January 2019

Biochemical, Structural, And Drug Design Studies Of Aspartate Transcarbamoylase From Pseudomonas Aeruginosa And Staphylococcus Aureus

Chandni Patel
Wayne State University, chpatel@med.wayne.edu

BIOCHEMICAL, STRUCTURAL, AND DRUG DESIGN STUDIES OF ASPARTATE TRANSCARBAMOYLASE FROM *PSEUDOMONAS AERUGINOSA* AND *STAPHYLOCOCCUS AUREUS*

by

CHANDNI PATEL

DISSERTATION

Submitted to the Graduate School

of Wayne State University,

Detroit, Michigan

in partial fulfillment of the requirements

for the degree of

DOCTOR OF PHILOSOPHY

2019

MAJOR: BIOCHEMISTRY AND MOLECULAR BIOLOGY

Approved By:

_____

Advisor Date

_____

_____

_____

DEDICATION

This dissertation is dedicated to my late grandmother, Smt. Manharbala Desai.

Ba, you will always be in my heart.

ACKNOWLEDGEMENTS

Last five years at Wayne State University has changed my life immensely in terms of personal and professional development. I would like to acknowledge those who made this dissertation possible and helped me reach this point.

I would like to thank my advisor, Dr. David Evans, for giving me the opportunity to work in his lab. I am thankful for his guidance and support as well as for the freedom he gave me to control my project. Dr. Evans has helped me become an independent scientist.

I would like to thank my committee members: Dr. Brian Edwards, Dr. Ladislau Kovari, and Dr. Steven Firestine for their feedback, guidance, and constructive criticism of my project.

I would like to thank Dr. Brian Edwards for generously providing me with lab resources, including reagents, instruments, and software licenses essential for my project. I thank Asmita Vaishnav for teaching me basic biochemistry techniques and for assisting me with my project. I will always be grateful for the love and care Asmita gave me as a mother figure in the lab.

I would like to thank my colleagues in the Evans lab specifically, Fatme Hachem for helping me in various ways when I first joined the lab and for teaching me basic experimental techniques, and Lauren Iacobelli for her friendship.

I would like to thank my friends outside my lab, Kendall Muzzarelli, Joshua Holcomb, Nicholas Spellmon, Tyler Peters, Hasini Kalpage, and Stephanie Gladyck for their friendship and their help with finding reagents and instruments for my experiments.

I would like to acknowledge Dr. Philp Pellett, BMI chair, and Dr. Bharati Mitra, former BMB interim chair as well as the BMI staff, April Wolak, Joseph Fiore, Mary Dismuke, and Kayla Gilmore for their support.

I thank my mother, Kinnari Desai for always believing in me and for supporting my life decisions. I thank my mama and mami, Nilay Desai and Mina Desai, for their insurmountable amount of help in my life. I thank my in-laws, Jasu Patel and Yogini Patel for their blessings. Lastly, I thank my husband, Krunal Patel, for being my backbone through this journey. I thank Krunal for always believing in me, supporting me, challenging me to be better, and for all the sacrifices he has made to help me achieve this goal.

Lastly, I thank Sai Baba. Baba blessed me with perseverance to achieve this goal.

TABLE OF CONTENTS

List of Figures

List of Tables

CHAPTER 1: GENERAL INTRODUCTION

1.1 Pyrimidine Biosynthesis

Pyrimidines play a significant role in a variety of life processes. They are the building blocks of DNA (cytosine and thymine) and RNA (uracil and cytosine) and are essential for replication and transcription as well as repair. Pyrimidine activated sugars are key intermediates in glycogen synthesis, glucuronidation reactions, protein and lipid glycosylation as well as phospholipid synthesis.

There are two pathways leading to the synthesis of pyrimidines, the salvage pathway and *de novo* biosynthesis pathway. In the salvage pathway, pyrimidine bases from cellular degradation of RNA and DNA are reattached to ribose sugars, activated 5-phosphoribosyl-1-pyrophosphate or PRPP, to yield UMP (uridine-5'-monophosphate) or CMP (cytidine-5'-monophosphate) in a single enzymatic step [1]. These nucleotides are further metabolized into all pyrimidine forms. The *de novo* biosynthesis pathway requires glutamine, bicarbonate, ATP (adenosine-5'-triphosphate), aspartate, and PRPP for the synthesis of UMP.

The *de novo* pyrimidine biosynthesis consists of six enzymatic reactions [2, 3]. The first reaction in the pathway is catalyzed by glutamine-dependent carbamoyl phosphate synthetase (CPSase, E.C. 6.3.5.5). CPSase catalyzes the formation of carbamoyl phosphate from glutamine, two molecules of ATP, and bicarbonate. Carbamoyl phosphate reacts with aspartate to form carbamoyl aspartate in a reaction catalyzed by aspartate transcarbamoylase (ATCase, E.C. 2.1.3.2). Dihydroorotase (DHOase, E.C. 3.5.2.3) catalyzes the reversible condensation of carbamoyl aspartate to dihydroorotate, which is then oxidized to orotate by dihydroorotate dehydrogenase. Orotate is coupled to

PRPP to form orotidine-5'-monophosphate (OMP) through a reaction catalyzed by orotate phosphoribosyl transferase (OPRTase). In the last step of the pathway, OMP is decarboxylated by OMP decarboxylase (ODCase) to form UMP, the product of pyrimidine biosynthetic pathway. UMP is further phosphorylated by UMP kinase to form UDP and UTP by nucleoside diphosphate kinase. CTP synthetase catalyzes the formation of CTP from UTP, ATP, and glutamine.

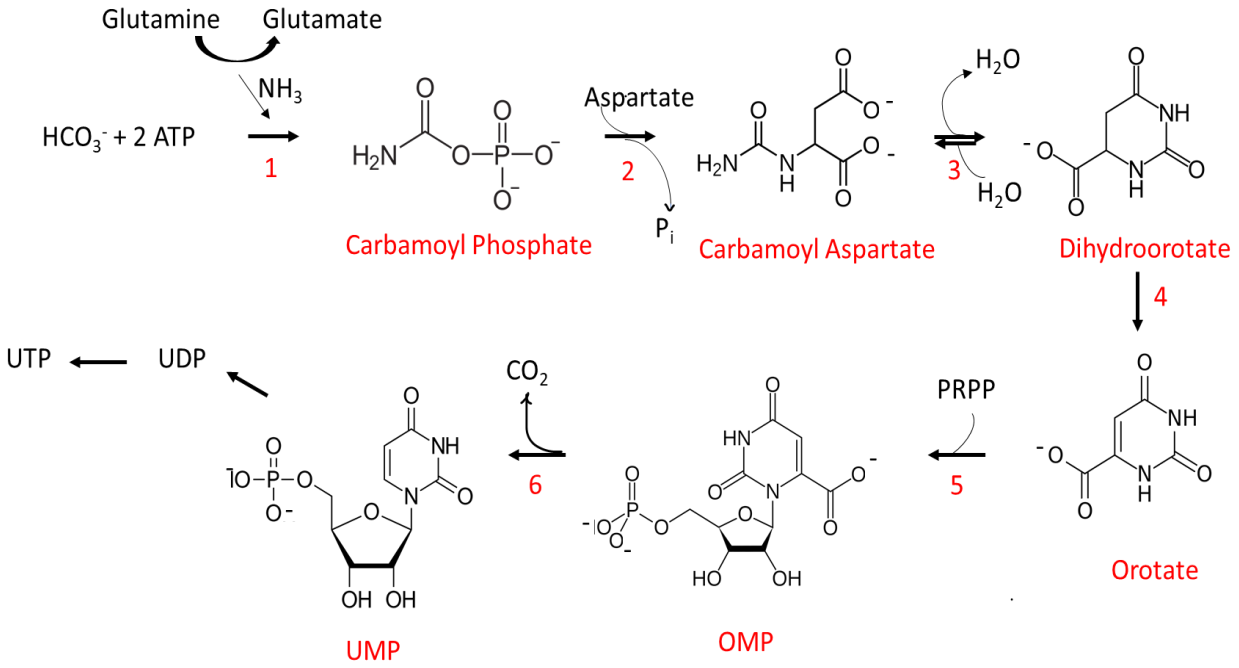

Figure 1: The *de novo* pyrimidine biosynthesis pathway
The *de novo* pyrimidine biosynthesis consists of six reactions leading to the formation of Uridine-5'-monophosphate (UMP) from bicarbonate, glutamine, 2 ATP, aspartate and PRPP. The reactions numbered in red are catalyzed by the following enzymes, (1) carbamoyl phosphate synthetase, (2) aspartate transcarbamoylase, (3) dihydroorotase, (4) dihydroorotate dehydrogenase, (5) orotate phosphoribosyl transferase, and (6) OMP decarboxylase.

In mammals, the first three enzymes of pyrimidine biosynthesis are consolidated on a single 243 kDa polypeptide, called CAD, combining CPSase, ATCase, and DHOase domains [2]. The fourth enzyme, DHODHase, is an integral membrane protein present on the outer leaf of mitochondrial inner membranes. OPRTase and ODCase activities,

the fifth and sixth steps of the pathway, are catalyzed by a 53 kDa bifunctional protein called UMP synthase [4]. In prokaryotes, these enzymes are expressed separately and function independently or associate non-covalently to form multi-functional oligomers.

Due to the essential role of pyrimidines in various cellular reactions, defects in pyrimidine biosynthesis can be devastating. For example, orotic aciduria, which is caused by a disabling point mutation in UMP synthase, is characterized by megaloblastic anemia and crystalluria [5], and is associated with defects in physical and intellectual development [6]. Treatment for this disorder is the administration of uridine triacetate which is then converted into UMP in the body.

1.1.1 Aspartate Transcarbamoylase

Aspartate transcarbamoylase (ATCase; EC 2.1.3.2) catalyzes the reaction of carbamoyl phosphate (CP) and aspartate to form N-carbamoyl-l-aspartate (CA) and inorganic phosphate [7] a key step in *de novo* pyrimidine biosynthesis. The catalytic subunits or domains of all known ATCases in eukaryotes, prokaryotes and archaea have a molecular mass of approximately 34 kDa and form stable homo-trimers under physiological conditions. Although ATCase is ubiquitous and catalyzes the same reaction, the enzyme from different organisms is remarkably polymorphic, differing in oligomeric structure, composition and regulatory properties.

ATCase is structurally organized as a part of 243 kDa CAD, combining CPSase, ATCase, and DHOase, in *Drosophila melanogaster* [8] and *Dictyostelium discoideum* [9]. The ATCases from the fungi, *Saccharomyces cerevisiae* [10] and *Neurospora crassa* [11] have a similar structural organization to CAD but lack DHOase activity. On the contrary, *Trypanosoma cruzi* ATCase is not part of CAD and exists independently, representing an

early progenitor in pyrimidine biosynthesis in the eukaryotic lineage before the gene fusion event [12].

In prokaryotes, these enzymes are expressed separately and function independently or associate non-covalently. The bacterial ATCase catalyzes the first committed reaction in pyrimidine biosynthesis, and it is therefore highly regulated. Bethel and Jones [13], have grouped the bacterial ATCases into three different families, A, B and C, based on their molecular size and feedback regulation characteristics. Class A are the largest with molecular size of 400-500 kDa dodecamers. Class A_1 consist of active ATCase and active dihydroorotase (DHOase), the third enzyme in the pathway, e.g. *Aquifex aeolicus* [14, 15] *Thermus aquaticus* [16], and *Streptomyces* [17]. X-ray studies of the *A. aeolicus* ATCase-DHOase complex have shown that two ATCase trimers are held together by three DHOase dimers, an dodecameric structure reminiscent of the 32 symmetry of *E. coli* ATCase, but with the regulatory dimers replaced by dimers of DHOase subunits [14, 15, 18]. In class A_2 the active dihydroorotase is replaced by its inactive homologue also known as pseudo-dihydroorotase as in *Pseudomonas fluorescens* [19], *Pseudomonas putida* [20], and *Pseudomonas aeruginosa* [21]. The inactive pseudo-dihydroorotase maintains ATCase activity by conserving the dodecameric assembly of the enzyme.

E. coli ATCase, the archetype ATCase, is designated as a class B enzyme. It is a 300 kDa heteromeric dodecamer consisting of six catalytic chains arranged into two trimers and six regulatory chains arranged into three dimers [22-24]. The catalytic subunit catalyzes the reaction and is not sensitive to nucleotides, whereas the regulatory subunit binds nucleotides but does not exhibit catalytic activity. The enzyme undergoes feedback

inhibition by CTP and UTP, the end products of the pathway, and activation by the purine nucleotide, ATP, providing a balance between the synthesis of pyrimidines and purines. X-ray studies (15-17) showed that two catalytic trimers are stacked above each other in nearly eclipsed configuration and are held together by three regulatory dimers, which are clustered around the periphery of the molecule.

Class C ATCases are the simplest and smallest in size with a molecular mass of 100 kDa. These ATCases are homotrimers of the catalytic subunit. They do not associate with regulatory subunit or any other enzymes in the pathway. Class C ATCases lack homotropic cooperativity and are insensitive to allosteric effectors, e.g. *Bacillus subtilis* [25, 26]. X-studies [27] of *B. subtilis* ATCase showed that its tertiary structure is very similar to the catalytic subunit of *E. coli* ATCase.

1.1.2 Dihydroorotase

Dihydroorotase (DHOase: E.C. 3.5.2.3) is a zinc metalloenzyme belonging to the amidohydrolase family of enzymes [28]. It catalyzes the pH-dependent, reversible cyclization of N-carbamoyl-L-aspartate into dihydroorotate, the third intermediate in *de novo* pyrimidine biosynthesis. Carbamoyl aspartate is favored above pH 6.2 and dihydroorotate below [29]. Although all DHOases catalyze the same reaction in all organisms, the enzyme adopts several different forms.

DHOases were initially classified into two distinct groups based on the phylogenetic analysis [30]. Long (type I) DHOases are more ancient and larger in size with a molecular mass of approximately 45 kDa. These DHOases function independently, associate non-covalently with ATCase, e.g., *Aquifex aeolicus* DHOase [14, 31], or are covalently linked with another enzyme in the pathway, e.g., CAD [2]. Short (type II)

DHOases, e.g., *E. coli* DHOase, are smaller in size with a molecular mass of 38 kDa. A more recent phylogenetic analysis reevaluated evolutionary relationships among DHOases [32]. Long DHOases now include bacterial type I (*Bacillus anthracis*, *A. aeolicus*, *Thermus thermophilus*, and *Staphylococcus aureus*) and III (*Porphyromonas gingivalis*), animal CAD and CAD-like inactive DHOases from fungi, whereas the short DHOases include active DHOases from fungi, bacterial type II (*E. coli*), and plant DHOases. The long DHOases have one or two layered β-stranded adjacent domain that clamps one lateral of the catalytic domain suggesting a stabilizing function. This adjacent domain is not present in the short DHOases which only consist of the catalytic domain. All DHOases have a TIM-barrel catalytic domain consisting of eight alpha helices and eight beta strands, with catalytic residues at the carboxyl end of the barrel [28, 33]. The archetypal metal center of DHOases is binuclear metal center with two zinc cations separated by approximately 3.6 Å, e.g., *E. coli* and *B. anthracis* DHOase [34]. On the contrary, *S. aureus* DHOase (PDB: 3GRI) [35] and *A. aeolicus* DHOase (PDB: 3D6N) [31] have only one Zn^{2+} center whereas the DHOase domain of human CAD has three Zn^{2+} ions bound in the active site (PDB: 4C6M) [32]. In bacterial type II, III, and CAD DHOases, the two Zn^{2+} are bridged by a carboxylated lysine, whereas in type I DHOase, the two Zn^{2+} ions are bridged by an aspartate residue [36]. Another distinct feature is the flexible loop that is present in all DHOases but bacterial type I DHOases [32]. This flexible loop functions to seal the active site when the substrate, carbamoyl aspartate, is bound and aids in catalysis by stabilizing the transition state, excluding solvent, and increasing the substrate electrophilicity [37, 38]. Bacterial type I DHOase (*A. aeolicus*) has a shorter loop that cannot seal the active site and interacts minimally with the substrate. The bacterial

type I DHOase associates with ATCase to complete the active site with an electropositive reaction chamber and attain full activity [15]. Additionally, loop 5 in bacterial type I DHOase interacts with ATCase from the top of the barrel [15, 39], whereas in all other DHOases, loop 5 is part of the dimerization interface [32] .

1.2 *Pseudomonas aeruginosa*

1.2.1 *Pseudomonas aeruginosa* and its Biology

Pseudomonas aeruginosa is a motile, Gram-negative bacillus, approximately 0.5 µm by 2 µ in size, with polar, monotrichous flagella. It is a highly versatile microorganism that can adapt in variable environments and nutritional availability [40]. It is typically found in soil and moist environments. *P. aeruginosa* is a non-fermentative, obligate aerobe that derives its energy from oxidation of carbohydrates. It can also be a facultative anaerobe and can use nitrate as a terminal electron acceptor in the absence of molecular oxygen [41, 42]. Using the arginine dihydrolase pathway, *P. aeruginosa* can convert arginine to ornithine and generate ATP [43]. *P aeruginosa* is mesophilic; it can grow at temperatures ranging from 25-42 °C with an optimal growth temperature of 37°C [44]. *P. aeruginosa* can be distinguished from other Pseudomonads by its production of pyocyanin, a blue phenazine secondary metabolite, that gives blue-green color to pus from *P. aeruginosa* infections and has been implicated in iron metabolism of *P. aeruginosa* [45].

1.2.2 Pathogenesis and Multi-Drug Resistance

P. aeruginosa is a highly opportunistic pathogen known to infect a wide range of hosts, including plants, insects, and humans [46]. In humans, it can cause mild illness in healthy individuals exposed to *P. aeruginosa* in poorly chlorinated hot tubs and pools or from using extended-wear contact lenses [47]. *P. aeruginosa* is a common cause of

nosocomial infections in immunocompromised patients with HIV [48] or cancer [49], patients undergoing a transplant [50], patients who are mechanically ventilated [51], and burn victims [52]. The common pseudomonal infections include infection of the soft tissue from burns, open wounds, or post-surgery, infection of the urinary tract due to use of urinary catheter, diabetic foot due to impaired microvascular circulation, otitis externa (swimmer's ear), keratitis, otitis media folliculitis (hot tub rash), bacteremia, pneumonia/respiratory infection due to cystic fibrosis, COPD or chronic obstructive pulmonary diseases, and mechanical ventilation [53]. *P. aeruginosa* is the main cause of morbidity and mortality in cystic fibrosis patients [54].

The stages of prototype *P. aeruginosa* infection include, adherence, colonization, invasion and dissemination, and systemic effects. *P. aeruginosa* has initial surface interactions with the host cells using flagella and cell surface pili, the main adhesins that enable binding to host cell membranes [55-57]. Once in contact with host cell membrane, *P. aeruginosa* activates its type III secretion system and secretes effector proteins into the host cell. These effector proteins interfere with signal transduction and cause irreversible damage to host cell membrane resulting in alterations in host immune responses and host cell necrosis [58, 59]. Once *P. aeruginosa* invades the host using its cell surface proteins and exotoxins, it can adapt to the host environment by means of quorum sensing and coordinating the expression of signaling molecules essential for survival, colonization, and virulence [60, 61]. Quorum sensing is a density-dependent signaling between cells through the production of autoinducer molecules. Quorum sensing has been shown to play a role in *P. aeruginosa* biofilm formation [62, 63] which causes persistent infections in cystic fibrosis patients. *P. aeruginosa* further invades the

host system by expressing a wide range of virulence factors, including exotoxin A, proteases, lipases, phospholipases, pyocyanin, and pyoverdine. Exotoxin A inhibits elongation factor 2 (EF2) in the host and inhibits protein synthesis; proteases degrade host complement factors and mucins, and disrupt intercellular junctions; lipases and phospholipases degrade lipids in the host cell membrane; pyocyanin causes oxidative stress in the host disrupting mitochondrial electron transport; pyoverdine is a siderophore that sequesters iron from host depots and allows for a competitive edge in the host environment where free iron is scarce [53, 64].

Multi-drug resistance of *P. aeruginosa* is increasing globally. *P. aeruginosa* has intrinsic resistance to a wide variety of antimicrobial agents due to low outer membrane permeability and efflux pumps pumping out macrolides, aminoglycosides, sulfonamides, tetracyclines, chloramphenicol, β-lactams, and fluoroquinolones [65, 66]. Overexpression of multiple efflux pumps has been found in several multi-resistant clinical isolates of *P. aeruginosa* [67]. Moreover, acquisition of resistance genes through horizontal transfer or mutational changes and decreased expression of outer membrane porin, OprD, have also been implicated in *P. aeruginosa* resistance to β-lactams, aminoglycosides, and carbapenem [68-70]. Adaptive resistance, including biofilm-mediated resistance and generation of persister cells, during environmental stress in *P. aeruginosa* has been attributed to tolerance of ciprofloxacin and tobramycin [71].

1.2.3 Current Therapeutics

The increase in antibiotic resistance among *P. aeruginosa* is associated with an increase in patient morbidity. Studies [72, 73] have shown that combination therapy in patients suspected of having pseudomonal infection leads to an increased likelihood of

choosing an effective agent. Combining an anti-pseudomonal β-lactam with a second anti-pseudomonal agent is suggested [74]. However, once susceptibility testing is available, treatment should be deescalated to monotherapy to reduce the risk of resistance selection.

Current empirical therapy for *P. aeruginosa* infections in patients with no assumed risk factors includes carbapenem, ceftazidime, and aminoglycoside [74]. Newly developed anti-Pseudomonal agents used clinically include, cefiderocol (cephalosporin), ceftolozane-tazobactam or ceftazidime-avibactam (cephalosporin + β-lactamase inhibitors), meropenem-vaborbactam (carbapenem + β-lactamase inhibitors) [74]. These new drugs for *P. aeruginosa* infections have a good safety profile and tolerability, rapid tissue distribution, and high activity against *P. aeruginosa* MDR strains, however, these drugs have increased cost, no oral formulation, and carry a risk of more resistant bacterial or fungal infection.

1.3 *Staphylococcus aureus*

1.3.1 *Staphylococcus aureus* and its Biology

Staphylococcus aureus is a member of the Micrococcaceae family. *S. aureus* is Gram-positive cocci, measuring 0.5 µM to 1.5 µM in diameter, which occur singly, in pairs, as short chains or in grape-like clusters [75]. *S. aureus* can grow in temperatures ranging from 7-48 °C with an optimum temperature of 37 °C. *S. aureus* naturally colonizes the skin, nasal passage, and axillae [76]. *S. aureus* is a facultative anaerobe; it can upregulate glycolysis and fermentation [77] and can readily use nitrate as the final electron acceptor under hypoxic conditions [78]. It can be distinguished from other Gram-positive cocci by anaerobic fermentation of glucose, and positive catalase and coagulase tests. *S. aureus*

is catalase positive and produces bubbles upon addition of a few drops of 3% hydrogen peroxide [76]. It is also coagulase positive and coverts soluble fibrinogen in plasma into insoluble fibrin. It is non-motile and non-spore forming [79] and produces microcapsules [80].

1.3.2 Pathogenesis and Multi-Drug Resistance

S. aureus is a commensal microorganism but also a serious pathogen. It is the most common cause of community-acquired and nosocomial infections. Everyone is susceptible to *S. aureus* infections; however, certain groups of people are at a greater risk, including patients with weakened immune system, diabetes, cancer, lung disease, or eczema and patients hospitalized in the intensive care units and with medical devices inserted in their bodies [81]. *S. aureus* causes a multitude of infections, including superficial mild cutaneous abscesses and impetigo to more invasive and life-threating pneumonia, osteomyelitis, bacteremia, endocarditis, sepsis, and toxic shock syndrome [82].

S. aureus infection usually results from a breach of the skin, the first line of defense, enabling the entry of bacteria into the underlying tissue. Once inside the host tissue, *S. aureus* overcomes the challenge of adhering to host tissue by expressing many surface protein adhesins called “microbial surface components recognizing adhesive matrix molecules” (MSCARMMs) [83]. These MSCARMMs bind to components of the extracellular matrix namely fibronectin, collagen, and fibrinogen, and facilitate tissue attachment. *S. aureus* can evade the host immune system in numerous ways. *S. aureus* shields its surface and impedes phagocytosis by polymorphonuclear leukocytes (PMNs) by expressing a polysaccharide microcapsule surrounding its cell wall [84]. It further

inhibits oposonization and phagocytosis by expressing protein A on the cell wall. Protein A binds to the Fc region of host IgG resulting in incorrectly oriented IgG that cannot be recognized by neutrophils [85]. *S. aureus* has been shown to inhibit neutrophil chemotaxis and recruitment toward complement activation by secreting chemotaxis inhibitory protein (CHIP) [86]. It secretes membrane-damaging polypeptides, notably α-hemolysin, a pore-forming exotoxin that targets multiple cell types and primarily causes cell lysis by allowing flow of ions and low molecular weight molecules through the amphipathic pore in the plasma membrane [87]. α-hemolysin has also been shown to delay corneal wound healing in keratitis and promote intracellular invasion of *S. aureus* [88]. *S. aureus* further invades the host tissue through a variety of extracellular enzymes that cause tissue destruction facilitating bacterial penetration into the tissue. A few of these enzymes include, proteases, lipases, nucleases, hyaluronate lyase, phospholipase C, metalloproteases [89]. *S. aureus* infections can be highly persistent and recurrent. S. *aureus* can form multilayered biofilm allowing a protected mode of growth, antibiotic resistance, and seeding dispersal to other sites [90]. *S. aureus* also has the ability to switch phenotype from normal colony phenotype (NCP) to a dormant small-colony variants (SCVs) phenotype. These SCVs can persist intracellularly in a protective niche from host immune system and antibiotics [91, 92]. SCVs are a result of selective pressure in the host environment, and they can revert to the parental phenotype after the discontinuation of antibiotic treatment.

S. aureus is notorious for developing multi-drug resistance. The first wave of resistance was seen during *S. aureus* resistance to penicillin that was mediated by β-lactamase. β-lactamase, encoded by *blaZ* gene, inactivates β-lactam antibiotics by

hydrolyzing the β-lactam ring [93]. The discovery of penicillase-resistant methicillin marks the onset of second wave of resistance. Methicillin resistance in *S. aureus* was first discovered by Jevons in 1961 [94] only two years after methicillin was introduced. The rise of methicillin resistant *S. aureus* (MRSA) is thought to have originated due to the horizontal transfer of *mecA* gene between *S. aureus* and another staphylococcal species [95]. *mecA* encodes for penicillin-binding protein, PBP2a, which has a lower affinity for β-lactam antibiotics compared to native PBP [96, 97]. Consequently, peptidoglycan cross-linking is not affected in MRSA. Methicillin resistance is a broad beta-lactam antibiotic class that is resistant to penicillin, cephalosporin, and carbapenem. Since 1970s, new MRSA strains have emerged including, MRSA II, III, and IV, community acquired (CA) MRSA, and hospital acquired (HA) MRSA, causing worldwide pandemic. The dramatic increase in vancomycin used to treat MRSA infections has inevitably triggered vancomycin resistance in *S. aureus.* Vancomycin intermediate-resistant *S. aureus* (VISA) carries several spontaneous mutations [98] that increase peptidoglycan synthesis and abnormally thick cell wall hindering vancomycin penetration into the cell [99]. Vancomycin resistant *S. aureus* (VRSA) is suggested to have resulted from conjugal transfer of *vanA* operon from a vancomycin-resistant *Enterococcus faecalis* [100]. In these isolates, with the presence of *vanA*, there is an alteration in the terminal peptide from D-Ala-D-Ala to D-Ala-D-Lac in the peptidoglycan resulting in reduced affinity to vancomycin and continuous peptidoglycan assembly [93].

1.3.3 Current Therapeutics

The therapeutic approach for *S. aureus* infections is based on the site and source of infection as well as on the detection of metastatic spread [101, 102]. Generally, the

infections caused by methicillin-sensitive *S. aureus* infection are treated by β-lactams, carbapenams, and cephalosporins. Methicillin-resistant *S. aureus* infection is commonly treated with vancomycin, a glycopeptide antibiotic. However, vancomycin must be given through IV, it is not absorbed if given orally. Other alternatives in case of treatment failure include linezolid and daptomycin. Linezolid is a new FDA-approved drug, an oxazolidinone antibiotic that has activity against methicillin-resistant as well as vancomycin-resistant *S. aureus* infections and is available in oral form with 100% bioavaibility [103, 104]. Another oxazolidinone that has been licensed for short-term treatment is tedizolid. Tedizolid binds to the 50S subunit of the bacterial ribosome and inhibits protein synthesis [105]. Daptomycin is a cyclic lipopeptide antibiotic for methicillin-susceptible, methicillin-resistant, and vancomycin-resistant *S. aureus*. Daptomycin kills by causing rapid depolarization of the bacterial cell membrane [106]. Three new lipoglycopeptides including, dalbavancin, oritavancin, and telavancin, have been approved by the FDA for skin and soft tissue infections.

CHAPTER 2: MATERIALS AND METHODS

2.1 PCR and Cloning

The genes encoding *S. aureus* ATCase and DHOase were cloned into pMCSG19C vector. These plasmids were a generous gift from Dr. Joseph Brunzelle at Northwestern University, IL.

The *pyr*B gene encoding *Pseudomonas aeruginosa* (PAO1 strain) ATCase was amplified by polymerase chain reaction (PCR) using forward primer: 5' CAT CAT CAC CAC CAT CAC CCG ACA GAC GCC AAG CGC CCG 3' and reverse primer: 5' GTG GCG GCC GCT CTA TTA TTC GGC GTC CTC CTG TTC CAG 3'. The *pyr*X gene encoding *P. aeruginosa* pDHO was amplified using forward primer: 5' CAT CAT CAC CAC CAT CAC ACC ATC AGT ATC CGA GGC GCC 3' and reverse primer: GTG GCG GCC GCT CTA TTA GCC CTC GTG GGT CAG GTG TCC 3'. The resulting PCR products were cloned separately into T7 pETite (Lucigen, catalog: 49001-1), an expression vector that incorporates a 6xHis tag on the amino end of the recombinant protein. The pETite vector and PCR product were co-transformed into HI-Control 10G chemically competent cells. pETite vector is provided in a linear form allowing recombination between the vector and PCR product within the host strain fusing the gene of interest to the vector.

2.2 Expression and Isolation of the Recombinant Proteins

The constructs were transformed separately into *E. coli* Hi-Control BL21(DE3) cells for protein expression. The transformants were grown at 37°C in LB medium until OD600 (optical density at 600 nm) of 0.6 and protein expression was induced by addition of 0.1 mM isopropylthio-β-D-galactoside (IPTG) followed by overnight (16-18 hours) incubation at 20°C. The cells were harvested by centrifugation and resuspended in binding buffer

consisting of 50 mM sodium phosphate, pH 7.5, 500 mM NaCl, and 5% glycerol. The cells were lysed by sonication and then passed through a French press. The cell lysate was centrifuged at 12,000 x g for 30 minutes at 4°C. The soluble fraction was applied to 5.0-ml Ni^{2+} Probond affinity column (Invitrogen) after equilibrating the column with ten column volumes of the binding buffer. The column was then washed three times with 10 column volumes of buffer containing increasing concentrations of imidazole, 0 mM imidazole, 25 mM imidazole, and 50 mM imidazole, and the proteins were eluted in 5-mL aliquots with 250 mM imidazole in the same buffer. The fractions were analyzed by electrophoresis on 12% SDS-PAGE gels [107]. Pure protein fractions were pooled and concentrated in the Amicon Ultra-15 centrifugal filter units (EMD Millipore, catalog: UFC901008). Protein concentrations were then determined by the Lowry method [108] using bovine serum albumin as a standard.

2.3 Size-Exclusion Chromatography

The molecular mass of the recombinant proteins was determined by size-exclusion on an ÄKTA Prime Plus chromatography system. The Ni^{2+} column purified pDHO/DHO, ATCase, and the ATCase-pDHO/DHO complex, reconstituted by mixing equimolar amounts of individual proteins, were applied to an ÄKTA Superdex S200 column equilibrated with 50 mM Tris-HCl, pH 7.5, 200 mM NaCl, and 5% glycerol. A 0.5-2.0 mL sample of purified protein, 5-10 mg/mL, was applied and eluted with the same buffer at a flow rate of 0.5 mL/min. The protein fractions were analyzed by electrophoresis on 12% polyacrylamide gel. The column was calibrated with a mixture of standard proteins (Bio-Rad, catalog: 1511901) with molecular weights from 1.3 –670 kDa and the mass of the eluted species was determined from plots of log (MW) versus elution volume.

2.4 Protein Quantification

The colorimetric Lowry protein assay [108] was used for the quantification of the proteins. A standard curve of 0 to 100 µg of bovine serum albumin (BSA) was prepared in 200 µL from 1 mg/mL BSA stock solution. The protein samples (3, 5, and 7 µL) were diluted in 200 µL water. Alkaline copper reagent consisting of 0.02 Na/K tartrate, 0.01% $CuSO_4.5H_2O$, and 1.96 % Na_2CO_3 in 0.1 N NaOH was prepared from stock solutions of 2% Na/K tartrate, 1% $CuSO_4.5H_2O$ and 2% Na_2CO_3 in 0.1 N NaOH. 800 µL of alkaline copper reagent was added to all standard and sample tubes. The tubes were vortexed and incubated for 15 minutes at room temperature. Folin and Ciocalteu's phenol reagent (Sigma, Catalog: F9252) was diluted 1:1 with water and 100 µL of diluted reagent was added to all tubes. The tubes were vortexed and incubated for 30 minutes at room temperature. The absorbance was measured at 750 nm and plotted as a function of BSA concentration. The protein concentrations of the three samples were determined using the standard curve

2.5 Enzyme Assay

ATCase activity was measured by the colorimetric method as previously described by Prescott and Jones [109, 110]. The reaction mixture to measure carbamoyl aspartate saturation curve of ATCase consisted of 8 mM aspartate, 50 mM Tris/acetate buffer, pH 8.3, and 1-4 µg of purified ATCase and variable (0-10 mM) carbamoyl phosphate in a total volume of 1 mL. The reaction mixture for aspartate saturation consisted of 10 mM carbamoyl phosphate, 50 mM Tris/acetate buffer, pH 8.3, 1-4 µg of purified ATCase and variable (0-15 mM) aspartate in a total volume of 1 mL. In *P. aeruginosa* ATCase activity assay samples, an equimolar amount of pDHO was present. Samples were pre-incubated

at 37°C for 1 min. The reaction was then initiated by the addition of carbamoyl phosphate or aspartate, 0-15 mM, and allowed to proceed for 2 min. The reaction was quenched by the addition of 1 mL of 5% acetic acid. Then 2 mL of color mix containing antipyrine/diacetyl monooxime in a 2:1 ratio was added, and the assay mixture was heated at 60°C for 60 min for color development. The carbamoyl aspartate generated by ATCase is converted into a yellow chromophore and the absorbance was measured at 466 nm.

DHOase activity for *S. aureus* DHOase was determined by measuring the reverse reaction, the formation of carbamoyl aspartate from dihydroorotate at pH 8.3. The reaction mixture to measure dihydroorotate saturation of DHOase consisted of 50 mM Tris/acetate buffer, pH 8.3, and 1-4 µg of purified DHOase and variable (0-8 mM) dihydroorotate in a total volume of 1 mL. Samples were pre-incubated at 37°C for 1 min. The reaction was then initiated by the addition of dihydroorotate and allowed to proceed for 2 min. The reaction was quenched with 1 mL of 5% acetic acid, and the samples were processed hereafter as mentioned for the ATCase assay above.

2.6 Chemical Cross-linking

Bis(sulfosuccinimidyl)suberate (BS3) (Thermo Scientific, catalog: 21580), non-cleavable amine-to-amine cross-linker, was freshly prepared by adding 2 mg of cross-linker to 70 µL water giving a 50 mM stock. Purified recombinant ATCase (45 µM) or pDHO (37 µM) in 50 mM sodium phosphate, pH 7.5, 500 mM NaCl, and 5% glycerol was cross-liked for up to 2 hours at room temperature with 5 mM bis(sulfosuccinimidyl)suberate as a final concentration. For cross-linking of ATCase-pDHO complex, ATCase (36µM) and pDHO (37 µM) in 50 mM sodium phosphate, pH

7.5, 500 mM NaCl, and 5% glycerol were crosslinked for the indicated times with 5 mM bis(sulfosuccinimidyl)suberate. The reaction was quenched by adding 10 µL of 1 M Tris-HCl, pH 8 and sample buffer consisting of 12 mM Tris-HCl, pH 6.8, 5% glycerol, 0.4% SDS, 2.88 mM β-mercaptoethanol, and 0.02% bromophenol blue. The samples were boiled at 100°C for 7 minutes and the cross-linked species were analyzed by SDS electrophoresis on 7.5% or 4-20% gradient polyacrylamide gel.

2.7 Thermal Shift Assay

Thermal shift assay using Applied Biosystems 7500 Real-time PCR system was performed to determine the thermal stability of the proteins. The final concentrations of individual subunits. ATCase and pDHO, ATCase-pDHO complex, and the SYPRO Orange (1000X stock, Invitrogen, Catalog: S6651) were optimized to 0.1 mg/mL, 0.05 mg/mL, and 20X, respectively [111]. The total reaction volume was 25 µL that was made up the addition of buffer consisting of 50 mM Tris, pH 7.5, and 200 mM NaCl. 200 µM PALA, 10 mM ATP, or 0-1 mM top-ranking FDA-approved compounds were present in the well where indicated. The microplate was sealed with an adhesive optical clear seal and centrifuged for 60 seconds at 1000 x g before placing in the instrument. The thermal shift assay was run from 25 to 95 °C with a ramp speed of 0.5°C/min. The melting temperature was determined using the 7500-software.

2.8 Polyacrylamide Gel Electrophoresis

Polyacrylamide gel electrophoresis were carried out using the Laemmli system [107], which uses a discontinuous buffer system. The acrylamide/bis-acrylamide percentage in all the separating gels varied from 4-20% gradient, 7.5% or 12% non-gradient depending on the size of the proteins separated. 7.5% acrylamide/bis-acrylamide

gels were typically used when analyzing ATCase-DHO complex formation. 0.1% SDS was present in all SDS gels and the electrophoresis buffer contained 0.192 M glycine, 0.025 M Tris-HCl, pH 8.3, and 0.1% SDS. The samples were boiled for 7 minutes at 100°C in sample buffer consisting of 12 mM Tris-HCl, pH 6.8, 5% glycerol, 0.4% SDS, 2.88 mM β-mercaptoethanol, and 0.02% bromophenol blue. The electrophoresis was carried out at a constant voltage of 150 V on ice until the dye front reached the bottom of the gel.

All native gels [112] consisted of 7.5% acrylamide/bis-acrylamide with or without 10 mM ATP or 10 mM sodium pyrophosphate and no SDS. The electrophoresis buffer contained 0.192 M glycine and 0.025 M Tris-HCl, pH 8.3. ATP (10 mM) or sodium pyrophosphate (10 mM) was present in the electrophoresis buffer when running gel with ATP or sodium pyrophosphate present in the gel matrix. The samples for native gel electrophoresis were prepared in the sample buffer containing 12 mM Tris-HCl, pH 6.8, 5% glycerol, and 0.02% bromophenol blue. The native gel electrophoresis was carried out at a constant voltage of 150 V for 55 minutes on ice.

2.9 Crystallization, Data Collection, and Structure Refinement

All proteins were gel-filtered in buffer containing 50 mM Tris-HCl, pH 7.5, 200 mM NaCl, and 1 mM dithiothreitol prior to crystallization. The crystals were grown at room temperature using the sitting-drop, vapor diffusion method by mixing the protein with an equal volume of reservoir solution. The crystals were harvested by soaking in a cryoprotectant solution consisting of mother liquor and 20% ethylene glycol prior to freezing in liquid nitrogen. X-ray diffraction data were collected at the Advanced Photon Source, Argonne National Laboratory in Illinois, and processed and scaled using the

program XDS [113]. The crystal structures were solved by the molecular replacement method with the program PHASER within the Phenix suite [114]. Structure modeling was carried out in COOT [115] and refinement was performed using Phenix and PDB-Redo [116]. The final structure was validated with Molprobity [114].

2.10 Programs used for Various Applications

Table 1: List of Programs

Program	**Application**
Phenix [114]	Xtriage: used to analyze diffraction data to assess quality and detect possible problems Phaser: Used for molecular replacement Autobuild: Used for automated model building Refine: Used to refine the structure by improving the fit of the model to the data MolProbity: To produce geometric validation statistics
PDB-Redo [116]	PDB-Redo Server: Optimizes refinement settings, refines, and partially rebuilds structure, and validates the results
Coot [115]	Used for model building, model manipulations, and validation
Yasara [117]	Used for molecular visualization
MOE [118]	Used for molecular visualization and virtual screening
PISA [119]	Used to calculate protein interfaces and assembly

CHAPTER 3: CHARACTERIZATION AND ASSEMBLY OF THE *PSEUDOMONAS AERUGINOSA* ASPARTATE-TRANSCARBAMOYLASE-PSEUDO DIHYROOROTASE COMPLEX

3.1 Abstract

Pseudomonas aeruginosa is a virulent pathogen that has become more threatening with the emergence of multidrug resistant strains. The aspartate transcarbamoylase (ATCase) of this organism is a dodecamer comprised of six 37 kDa catalytic chains and six 45 kDa chains homologous to dihydroorotase (pDHO) but inactive. The pDHO chain itself has no catalytic activity but is necessary for ATCase activity. Here we have cloned and expressed both *P. aeruginosa* subunits. A stoichiometric mixture of the two proteins associates into a dodecamer with full ATCase activity. Unlike the catalytic subunit of other known ATCases, the *P. aeruginosa* catalytic chain does not spontaneously assemble into a trimer. Chemical crosslinking and size-exclusion chromatography clearly showed that protein remains monomeric which accounts for its lack of catalytic activity since the active site is a composite comprised of residues contributed by adjacent monomers in the trimer. Circular dichroism spectroscopy indicated that the ATCase chain folds into a well-defined structure although neither the ATCase nor the pDHO subunits are very stable as determined by a thermal shift assay. However, formation of the complex increases the melting temperature by about 30°C. Another unusual characteristic is that the ATCase is strongly inhibited by all nucleotide di- and triphosphates and exhibits extreme cooperativity. Previous studies suggested that the regulatory site is in an 11-residue extension of the amino end of the ATCase chain. However, deletion of the extensions of both the amino and carboxyl ends of the polypeptide did not affect catalytic activity, nucleotide inhibition or the assembly of the

dodecamer. Nucleotides destabilized the dodecamer which can probably account for the inhibition and extreme cooperativity of the substrate saturation curves. In contrast to previous interpretations, these results suggest that *P. aeruginosa* ATCase is not allosterically regulated by nucleotides.

3.2 Introduction

Pseudomonas aeruginosa is a ubiquitous, saprophytic microorganism that normally inhabits the soil and aquatic environments. It is an opportunistic pathogen that can infect a wide variety of hosts including plants, nematodes, insects, and animals [120]. *P. aeruginosa* is the leading cause of nosocomial infections in immunocompromised patients and is most commonly associated with ventilator-associated pneumonia and burn wound infections with a high mortality rate [121]. *P. aeruginosa* is the most common cause of respiratory failure and death in patients with cystic fibrosis [122]. Treating *P. aeruginosa* infections is challenging due to increasing resistance of *P. aeruginosa* to existing therapeutics.

Aspartate transcarbamoylase (ATCase; EC 2.1.3.2) catalyzes the reaction of carbamoyl phosphate (CP) and aspartate to form N-carbamoyl-l-aspartate (CA) and inorganic phosphate, a key step in *de novo* pyrimidine biosynthesis [7]. *P. aeruginosa* ATCase belongs to class A2 ATCases. The first class A2 ATCase was purified by Adair and Jones [123] from *Pseudomonas fluorescens*, who found that the protein was a dimer composed 180 kDa subunits and that it was inhibited by ATP, CTP and UTP. In view of the unusual subunit structure that suggested that the catalytic unit is not trimeric, we re-examined the size, composition and regulation of *P. fluorescens* ATCase [19]. In this study, isolated *P. fluorescens* ATCase was found to be a 460 kDa dodecamer composed

of six copies of a 34 kDa catalytic trimer and six copies of a 45 kDa subunit of unknown function. The function of the isolated subunits could not be ascertained because they could not be separated without denaturation and loss of ATCase activity. However, the 34 kDa polypeptide was shown to be an ATCase catalytic chain by affinity labelling of the active site with the competitive inhibitor, [^{14}C]-pyridoxal phosphate followed by sodium borohydride reduction. Schurr et al. [124] subsequently sequenced the 45 kDa subunit and showed that it was pDHO.

We then investigated the ATCase from *P. aeruginosa* [21] and found that it had the same subunit structure and putative regulatory properties. All oxy- and deoxynucleotide triphosphates strongly inhibited the enzyme. Free GTP and ATP, but not the Mg^{2+}ATP, inhibited the enzyme. It is difficult to reconcile these results with the proposed function of allosteric regulation of ATCases, namely, to balance the levels of pyrimidines and purines.

We report here the overexpression and purification of *P. aeruginosa* ATCase and pDHO, and determination of oligomeric states of individual proteins to better understand the assembly of the dodecamer. Unlike the ATCase from other organisms, the catalytic unit is monomeric and only becomes a catalytically active trimer when it associates with pDHO. Successful purification and crystallization of the *P. aeruginosa* ATCase-pDHO complex enhances our knowledge of class A_2 ATCases and represents a new target to develop antipseudomonal therapies.

3.3 Materials and Methods

3.3.1 CD Spectrometry

The CD spectra of pDHO (1.8 µM), ATCase (2.67 µM), and the ATCase-pDHO complex (1.8 µM) prepared by mixing stoichiometric amounts of pDHO and ATCase, were obtained in the wavelength range of 185-300 nm using a Jasco CD spectrophotometer. The proteins were prepared in 5 mM sodium phosphate, pH 8.

3.3.2 Controlled Proteolysis by Elastase

Purified recombinant ATCase was subjected to controlled proteolysis at 37°C at a protein-to-elastase ratio (wt/wt) of 250. The reaction mixture consisted of 160 µg of ATCase or 160 µg of ATCase-pDHO complex and 0.64 µg of elastase per 160 µL in 50 mM Tris-HCl, pH 8, and 200 mM NaCl with or without 100 µM PALA. Samples were taken periodically over 60 minutes and quenched by adding 5 µL of sample buffer consisting of 12 mM Tris-HCl, pH 6.8, 5% glycerol, 0.4% SDS, 2.88 mM β-mercaptoethanol, and 0.02% bromophenol blue, and by heating for 7 min at 100°C. The samples were analyzed by electrophoresis on SDS 12% polyacrylamide gel.

3.3.2 Crystallization, Data Collection, and Refinement

Prior to crystallization, 200 µM N-phosphonacetyl-L-aspartate (PALA) was added to gel-filtered delN ATCase-pDHO complex in 50 mM Tris-HCl, pH 7.5, 200 mM NaCl, and 1 mM dithiothreitol. All crystals were grown at room temperature using the sitting-drop, vapor diffusion method. 1 µL of Ndel ATCase-pDHO - PALA solution was mixed with 1 µL of reservoir solution containing 20% polyethylene glycol 10,000, 0.1 M hydroxyethyl-piperazineethane-sulfonic acid or HEPES buffer, pH 7.5, and 1 mM Anderson−Evans polyoxotungstate [TeW6O24]6− (TEW). Crystals that grew within two weeks were then used for preparing seed stock for performing subsequent seeding experiments as follows: 2 µL of the drop solution - including the crystals - was added to

50 µL of reservoir solution in a microcentrifuge tube with Seed Bead (Hampton) and vortexed for 3 minutes to generate seed stock. One µL of 1:4 diluted seed stock was mixed with one µL of 1 mg/mL delN ATCase-pDHO-PALA solution to allow crystal growth at room temperature using the sitting-drop, vapor diffusion method. The best diffracting cubic crystals grew to 0.1 mm x 0.1 mm within 2-4 days. The crystals were soaked in a cryoprotectant solution consisting of 25% polyethylene glycol 10,000, 0.1 M hydroxyethyl-piperazineethane-sulfonic acid or HEPES buffer, pH 7.5, and 1 mM Anderson−Evans polyoxotungstate [TeW6O24]6− (TEW), 200 µM PALA, and 20% ethylene glycol prior to freezing in liquid nitrogen. X-ray diffraction data were collected at the Advanced Photon Source, Argonne National Laboratory in Illinois. The crystals belong to the space group H32 (No. 155) and diffracted to 2.47 Å resolution, with one delN ATCase, one pDHO, and two molecules of TEW in the asymmetric unit. The structure was solved by the molecular replacement method using the PHASER application within the Phenix suite from uncomplexed homology models of ATCase and pDHO. Structure modeling was carried out in COOT and refinement was performed using Phenix.

3.4 Results

3.4.1 Cloning, Expression, and Purification of *P. aeruginosa* ATCase and pDHO

The *pyrB* gene encoding *P. aeruginosa* ATCase and the *pyrX* gene encoding pDHO from strain PAO1 were separately amplified by PCR and inserted into the pETite vector, which incorporates a 6x His tag on the amino terminus of the proteins. The resulting constructs were then transformed into *E. coli* Hi-Control BL21(DE3) cells. The proteins were expressed and purified as described in chapter 2. Although significant

amounts of both proteins formed inclusion bodies, the soluble proteins were both expressed at 40 mg/liter (Fig. 2A and B).

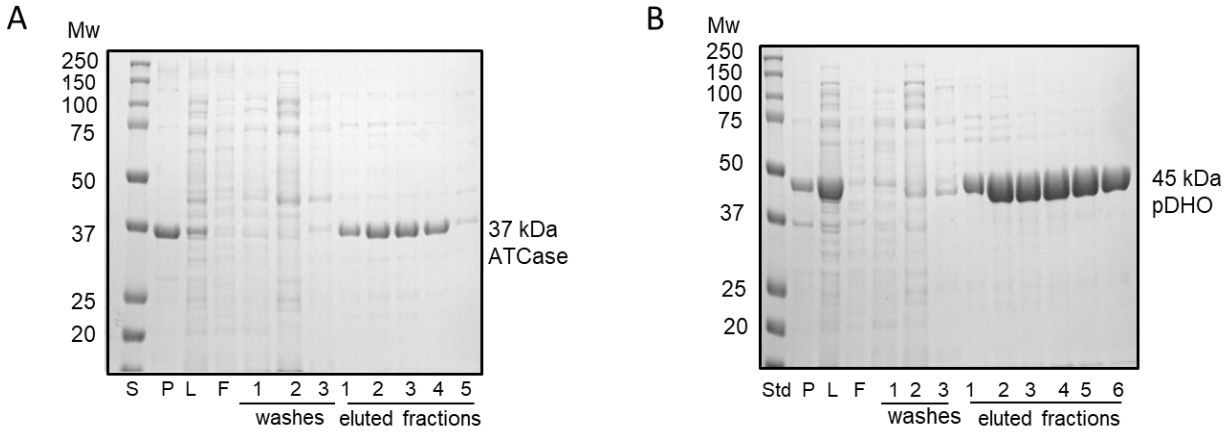

Figure 2: Expression and Purification of *P. aeruginosa* ATCase and pDHO.
The genes encoding *P. aeruginosa* ATCase (*pyr*B) and pDHO (*pyr*X) were separately cloned into pETite (Lucigen), an expression vector that incorporates a 6xHis tag on the amino end of the recombinant proteins. The resulting constructs were transformed separately into *E. coli* Hi-Control BL21(DE3) cells (Lucigen). The transformants were grown at 37°C in LB medium until OD600 of 0.6 and induced with 0.1 mM IPTG overnight (16-20 hours) at 20°C. The cells were harvested and resuspended in 50 mM sodium phosphate and 0.5 M NaCl, pH 7.5, and passed twice through a French press. The cell lysate was centrifuged at 12,000 x g for 45 minutes at 4°C. The supernatant was applied to 5.0 ml Ni^{2+} affinity column. The column was washed with 10 column volumes with increasing concentration of imidazole up to 100 mM. the proteins were eluted in 5 mL aliquots with 250 mM imidazole in the same buffer. A) ATCase and B) pDHO fractions were analyzed by electrophoresis on 12% SDS-PAGE Laemmli gels; S: protein standard, P: pellet, L: lysate, F: flow-through.

3.4.2 Oligomeric Structure of *P. aeruginosa* ATCase and pDHO

On SDS-PAGE, under denaturing conditions, ATCase had an estimated molecular mass of 36 kDa, in agreement with the mass calculated from the amino acid sequence. ATCase purified by nickel affinity chromatography was then subjected to gel filtration chromatography on a calibrated Superdex S200 column. ATCase eluted as a single species with a molecular mass of 37 kDa indicating that it is monomeric (Fig. 3A & B). The isolated pDHO monomer had a molecular mass of 45 kDa on denaturing SDS gels

but eluted as a 90 kDa species on the S200 size exclusion column indicating that it forms stable dimer (Fig. 3C & D).

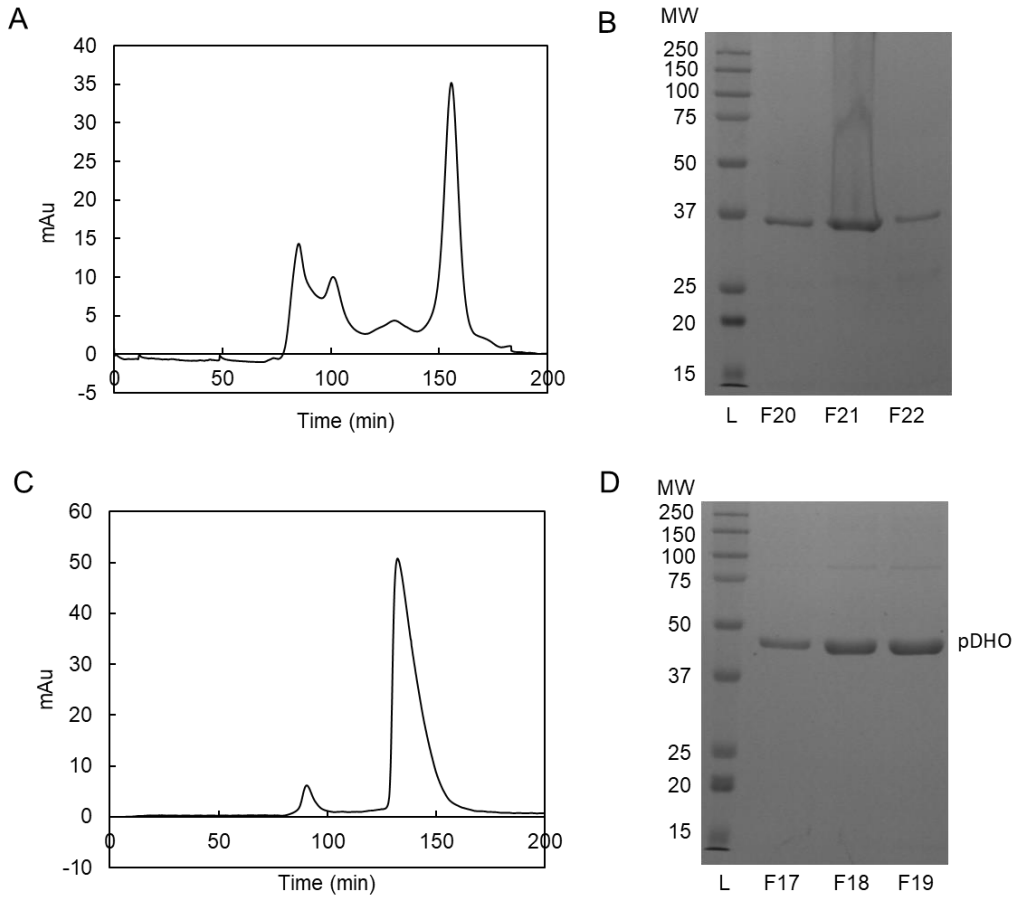

Figure 3: Oligomeric Structure of P. aeruginosa ATCase and pDHO
A) Purified *P. aeruginosa* ATCase was subjected to size-exclusion chromatography on a Superdex S200 Akta column and B) the fractions, F20, F21, and F22, corresponding to the ATCase peak were analyzed by 12% SDS-PAGE. C) Purified *P. aeruginosa* pDHO was subjected to size-exclusion chromatography. D) Fractions F17, F18, and F19 corresponding to pDHO peak were analyzed by 12% SDS-PAGE.

3.4.3 Chemical Cross-linking

The oligomeric structure of the proteins was also examined by chemical crosslinking. In agreement with the size exclusion chromatography, crosslinking of the ATCase subunit with BS3 (bis(sulfosuccinimidyl)suberate) for up to two hours, showed that the protein remained monomeric (37 kDa) although trace amounts of a higher

molecular species were visible (Fig. 4A). Although size exclusion chromatography showed that the pDHO is dimeric, no crosslinked species were observed (Fig. 4B). This result suggested that the pDHO dimer cannot undergo crosslinking because the lysines are not located near the dimer interface of pDHO.

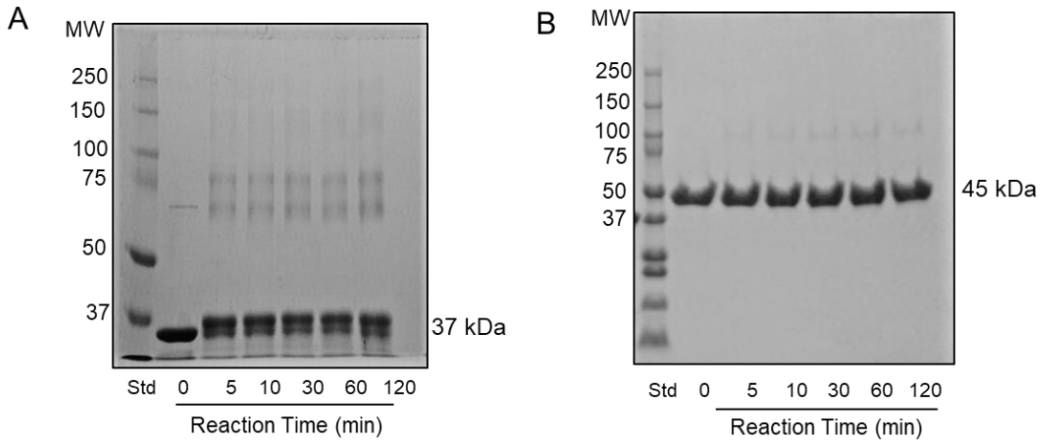

Figure 4: Chemical Crosslinking of *P. aeruginosa* ATCase and pDHO
A) Purified recombinant ATCase (45 µM) in 50 mM sodium phosphate, pH 7.5, and 500 mM NaCl, was cross-linked for the indicated times with 5 mM bis(sulfosuccinimidyl)suberate. The reaction was quenched by adding 10 µL of 1 M Tris-HCl, pH 8. Cross-linked species were analyzed by electrophoresis on a 7.5% polyacrylamide gel. B) chemical crosslinking of pDHO as described for ATCase.

3.4.4 Isolation and Composition of the ATCase-pDHO Complex

The isolated ATCase subunit lacked catalytic activity. However, titration of the purified ATCase subunit with pDHO subunit restored the latent catalytic activity (Fig. 5A). ATCase activity increased linearly with increasing amounts of pDHO until a molar ratio of ATCase to pDHO was 1:0.97, and the activity then leveled off as pDHO binding site on ATCase became saturated.

The *P. aeruginosa* complex was reconstituted by mixing an equimolar ratio of the ATCase and pDHO subunits. The reconstituted complex was then subjected to gel filtration chromatography on a calibrated Superdex S200 column. The ATCase-pDHO

complex eluted in single peak with a molecular mass of 457 kDa (Fig. 5B & C). SDS gel electrophoresis confirmed that the complex consisted of equimolar amounts of the two subunits. Furthermore, individual ATCase, pDHO, and ATCase-pDHO complex were subjected to native gel electrophoresis. The isoelectric points of ATCase and pDHO are 6.36 and 5.46, respectively. Laemmli's gel system without SDS at pH 8.3 was used to analyze these acidic proteins for native PAGE. The ATCase-pDHO complex had a band very distinct from individual subunits at a molecular weight of 480 kDa approximately (Fig. 5D), confirming oligomerization of ATCase and pDHO as shown by size exclusion chromatography.

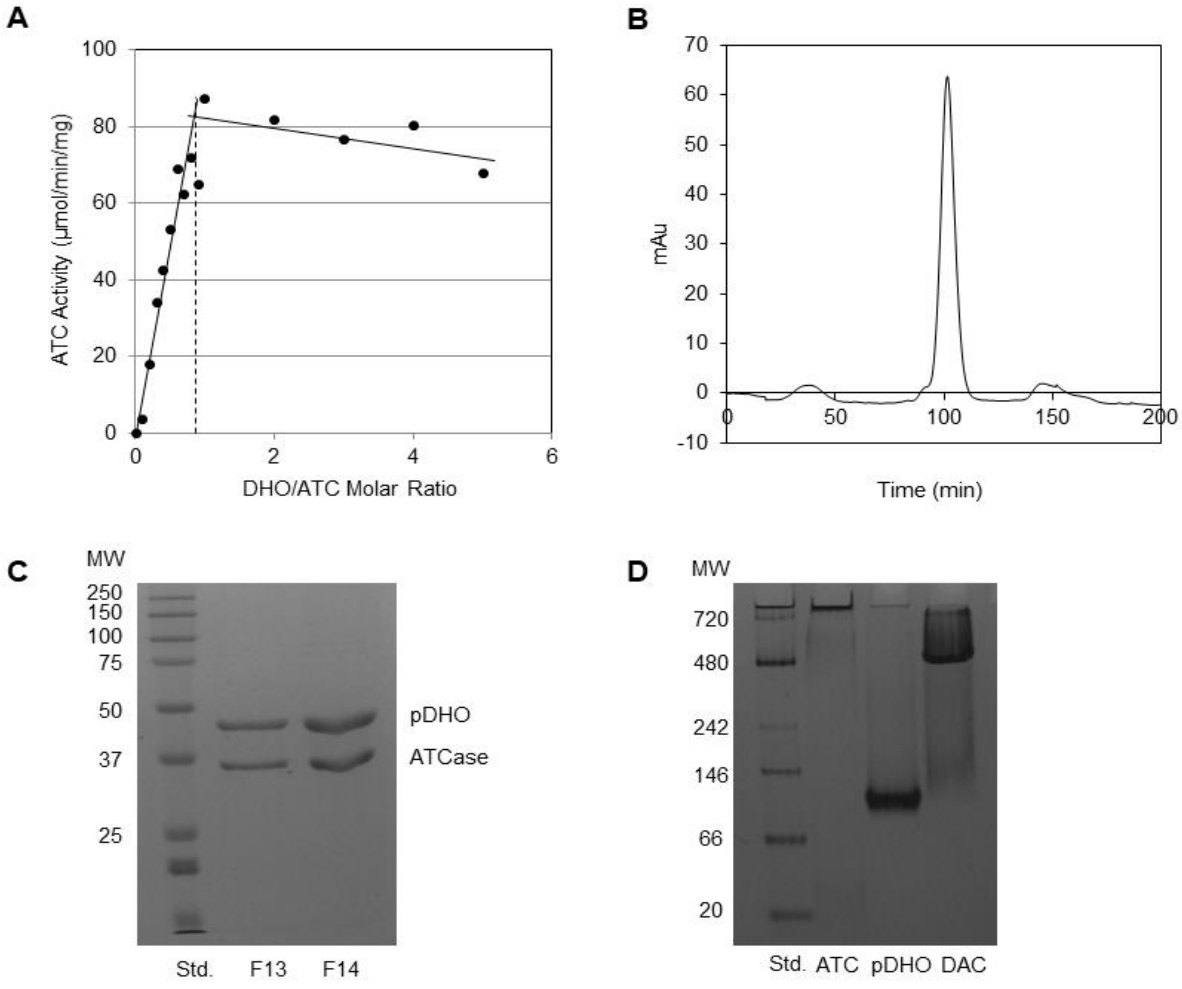

Figure 5: Formation of the ATCase-pDHO Complex.
A) A fixed constant amount of ATC (4 µg) was titrated with increasing amounts of pDHO (0-24.3 µg). The ATCase activity was measured at 37°C as described in chapter 2. B) Purified recombinant ATCase and pDHO were mixed in an equimolar ratio and the complex was analyzed by size-exclusion chromatography on a Superdex S200 column. C) Fractions F13 and F14 corresponding to the complex peak were analyzed on 12% SDS-PAGE. D) 7.5% native gel with ATCase, pDHO, and ATCase-pDHO complex (DAC). Chemical cross-linking of the *A. aeolicus* ATCase-and DHOase with DMS dimethyl suberimidate gave a limited number of crosslinked species (Fig. 6A) [14]. Crosslinking of the *P. aeruginosa* ATCase-pDHO with BS3 (bis(sulfosuccinimidyl)suberate) showed additional species suggesting a more complex assembly/disassembly pathway (Fig. 6B). In the absence of the crosslinking reagent, the *P. aeruginosa* complex was fully dissociated on the SDS gel into the constituent subunits (Fig 6B, lane 3). After the addition of the crosslinker, many more partial species were trapped, suggesting more complex association/dissociation pathway. An identical profile of crosslinked species was reproducibly obtained in eight crosslinking experiments.

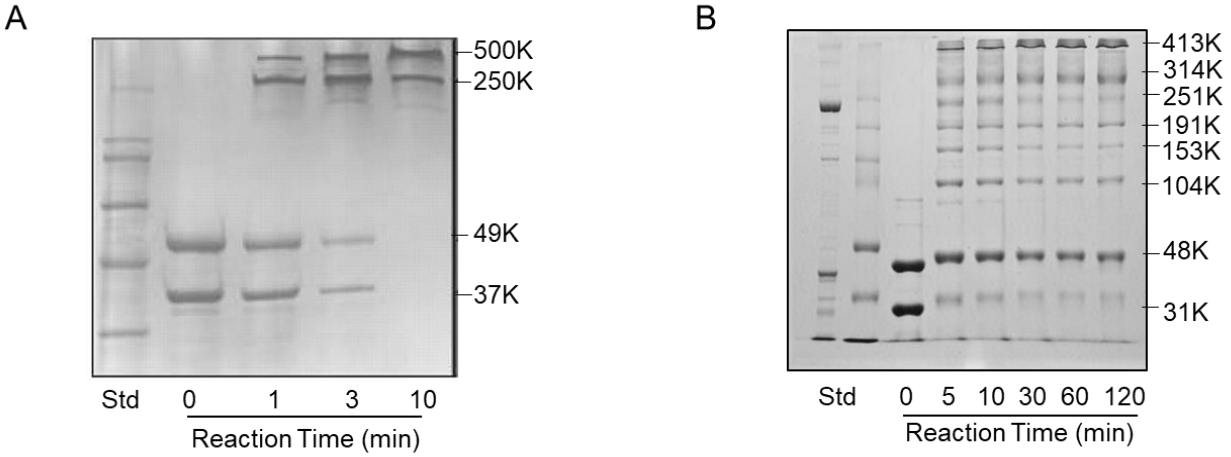

Figure 6: Assembly of the ATCase-pDHO complex
A) Chemical cross-linking of *A. aeolicus* ATCase and DHOase with DMS dimethyl suberimidate, Ahuja et al. [14]. B) Purified recombinant *P. aeruginosa* ATCase (36 µM) and pDHO (37 µM) in 50 mM sodium phosphate, pH 7.5, and 500 mM NaCl, were cross-linked for the indicated times with 5 mM bis(sulfosuccinimidyl)suberate. The reaction was quenched by adding 10 µl of 1 M Tris-HCl, pH 8. Cross-linked species were analyzed by electrophoresis on a 7.5% polyacrylamide SDS gel.

3.4.5 Steady State Kinetics

The ATCase steady state kinetics parameters were obtained from carbamoyl phosphate (Fig. 7A) and aspartate (Fig. 7B) saturation curves. As previously reported, *P. aeruginosa* ATCase was found to be inactive in the absence of pDHO. Activity was restored by the addition of an equimolar amount of pDHO to the assay mixture. The

carbamoyl phosphate saturation curve of *P. aeruginosa* ATCase-pDHO complex was sigmoidal. A least square fit of the data to the Hill equation gave a K_m for carbamoyl phosphate ($[S]_{0.5}$) of 2.5 mM and a V_{max} of 142 µmoL/min/mg (Table 2). The aspartate saturation curve of ATCase-pDHO had a K_m for aspartate of 3.6 mM and a V_{max} of 183 µmoL/min/mg. Both aspartate and carbamoyl phosphate saturation curves exhibit modest sigmoidicity. The bi-substrate inhibitor N-phosphonacetyl-L-aspartate (PALA) is also a potent inhibitor of the of the *P. aeruginosa* enzyme. Although PALA is a competitive inhibitor of the ATCase, *P. aeruginosa* ATCase is not inhibited competitively by PALA (Fig. 7C, Table 3).

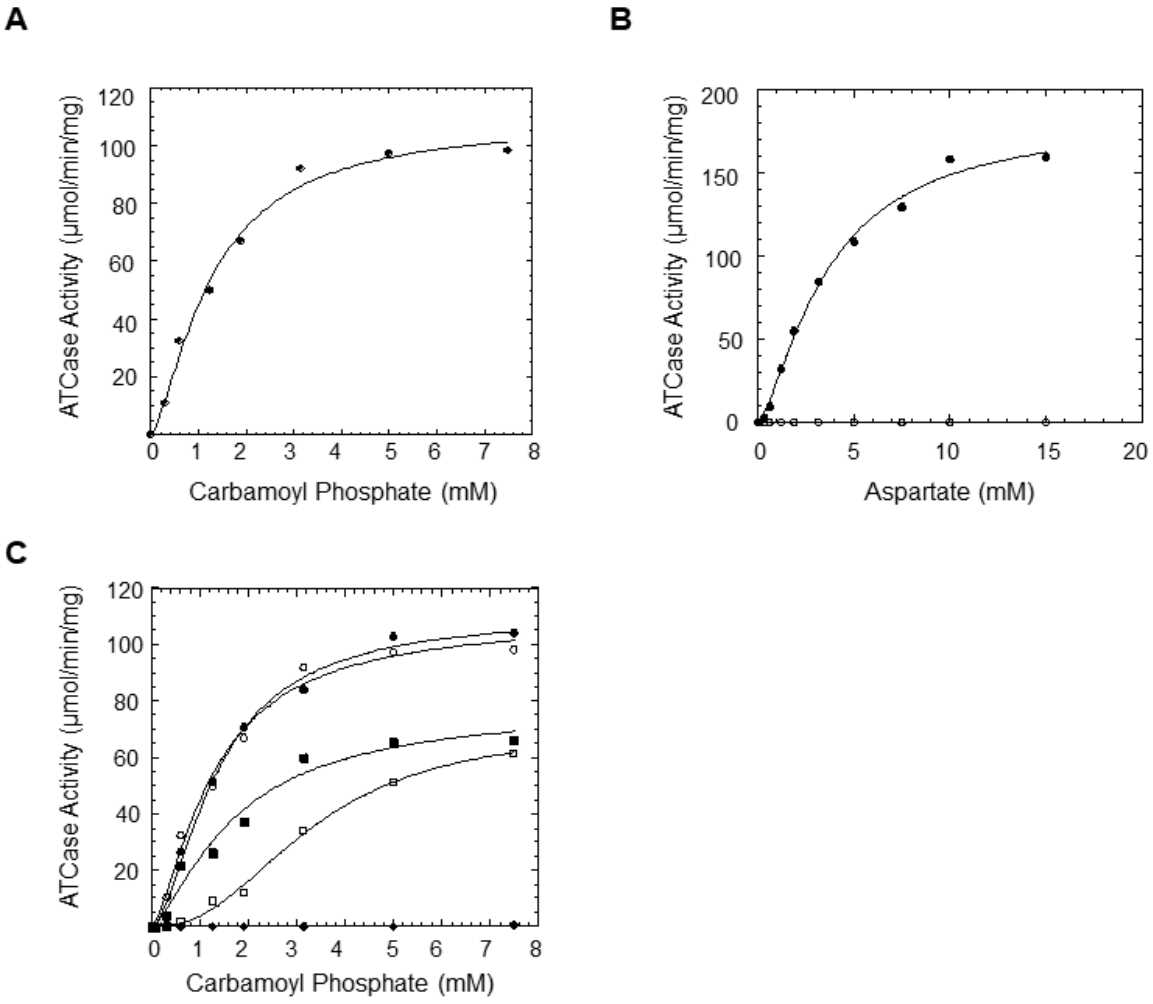

Figure 7. Carbamoyl Phosphate and Aspartate Saturation Curves for *P. aeruginosa* ATCase Kinetics.
ATCase activity was measured described in Chapter 2. A) Carbamoyl phosphate saturation: aspartate was fixed at 8 mM and carbamoyl phosphate was the variable substrate. B) Aspartate saturation: carbamoyl phosphate fixed at 10 mM and aspartate as the variable substrate. C) Carbamoyl phosphate saturation curves with aspartate fixed at 8 mM, in the absence of PALA (○), and presence of 1 nM (●), 25 nM (■), 100 nM (□), and 500 nM (♦) PALA. The saturation curves were fit to the Hill equation: $v=V_{max}[S]^n/(K_m^n + S^n)$.

Table 2: Steady State Kinetics of *P. aeruginosa* ATCase

Variable Substrate	Carbamoyl Phosphate (CP)	Aspartate (Asp)
K_m (mM)	2.8 ± 0.18	3.63 ± 0.41
V_{max} (µmol/min/mg)	142 ± 7.5	183.2 ± 4.3
k_{cat} (s^{-1})	87.6	113.0
k_{cat}/K_m ($s^{-1}M^{-1}$)	3.1×10^4	3.1×10^4
Hill coefficient	2.82 ± 0.35	1.44 ± 0.14

Table 3: PALA Inhibition

PALA (nM)	K_m (mM)	V_{max} (µmol/min/mg)	Hill Coefficient
0	1.27 ± 0.16	108.78 ± 6.60	1.46 ± .020
1	1.36 ± 0.12	110.73 ± 5.40	1.65 ± 0.20
25	1.74 ± 0.47	78.00 ± 10.72	1.40 ± 0.34
100	3.34 ± 0.24	70.73 ± 4.32	2.37 ± 0.24

3.4.6 Circular Dichroism Spectroscopy of ATCase, pDHO, and the ATCase-pDHO Complex

In the absence of pDHO, it is possible that the ATCase trimer does not form because the protein is not folded properly. However, CD spectroscopy of isolated ATCase and pDHO showed that both *P. aeruginosa* proteins have at least a well-defined secondary structure (Fig. 8A, Table 4). The CD spectrum of ATCase-pDHO complex has a similar secondary structure. More subtle changes in the tertiary structure no doubt occur.

3.4.7 Thermal Stability of ATCase, pDHO, and ATCase-pDHO Complex

A thermal shift assay was employed to determine the relative stability of the isolated subunits and the complex (Fig. 8B). The melting temperature of the proteins were analyzed by calculating the first derivative of the fluorescence vs. temperature plot using the Applied Biosystems 7500 software. ATCase and pDHO subunits had melting temperatures of 38°C and 44°C, respectively. When the reconstituted ATCase-pDHO complex was subjected to thermal shift, there was a dramatic positive shift in the melting temperature of the complex to 77°C indicating that while the ATCase and pDHO subunits are relatively unstable, the ATCase-pDHO dodecamer is quite stable.

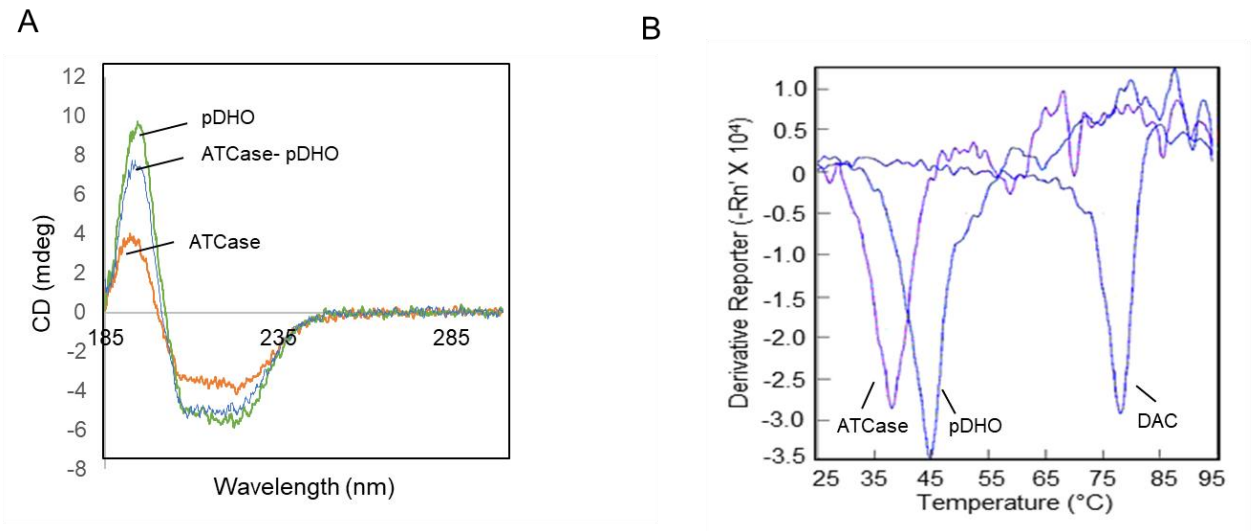

Figure 8: Folding and Thermal Stability of *P. aeruginosa* ATCase, pDHO and the complex

A) The CD spectrum of *P. aeruginosa* ATCase, pDHO, and the ATCase-pDHO complex formed by mixing stoichiometric amounts of the two subunits, in 5 mM sodium phosphate, pH 8.0. B) The thermal stability of each purified recombinant protein, ATCase, pDHO, and the ATCase-pDHO complex, was measured by preparing the proteins in buffer containing 50 mM Tris pH 7.5 and 200 mM NaCl, and then subjecting the sample to a thermal shift assay using 500X SYPRO Orange dye. The fluorescence was measured over a temperature range of 25 °C to 95 °C.

Table 4: CD Spectroscopy[a]

Secondary Structure	ATCase	pDHO	ATCase-pDHO
	%	%	%
Helices	15.9	23.7	15.2
Sheets	32.3	26.4	33.4
Turns	22.0	21.7	22.3
Undetermined	29.8	28.2	26.6

[a]The average of two scans

3.4.8 Trimerization of *P. aeruginosa* ATCase

ATCase was subjected to size-exclusion chromatography on an S200 Superdex column in the presence of 200 µM PALA in the sample as well as in the buffer, 50 mM

Tris pH 7.5 and 200 mM NaCl. PALA is a bisubstrate analog that has a very high affinity for the active site of ATCase. The active site of ATCase is composed of residues from adjacent monomer. Therefore, the rationale for subjecting ATCase to size-exclusion in the presence of PALA was that PALA would bind in the active site of the enzyme and facilitate trimer formation. However, ATCase eluted as a monomer even in the presence of PALA (Fig. 9A & B), indicating that PALA does not facilitate ATCase trimer formation. Furthermore, ATCase was subjected to cross-linking with BS3 in the presence of 200 μM PALA for up to two hours, however, most of the protein remained monomeric with some trace of dimer formation (Fig. 9C & D).

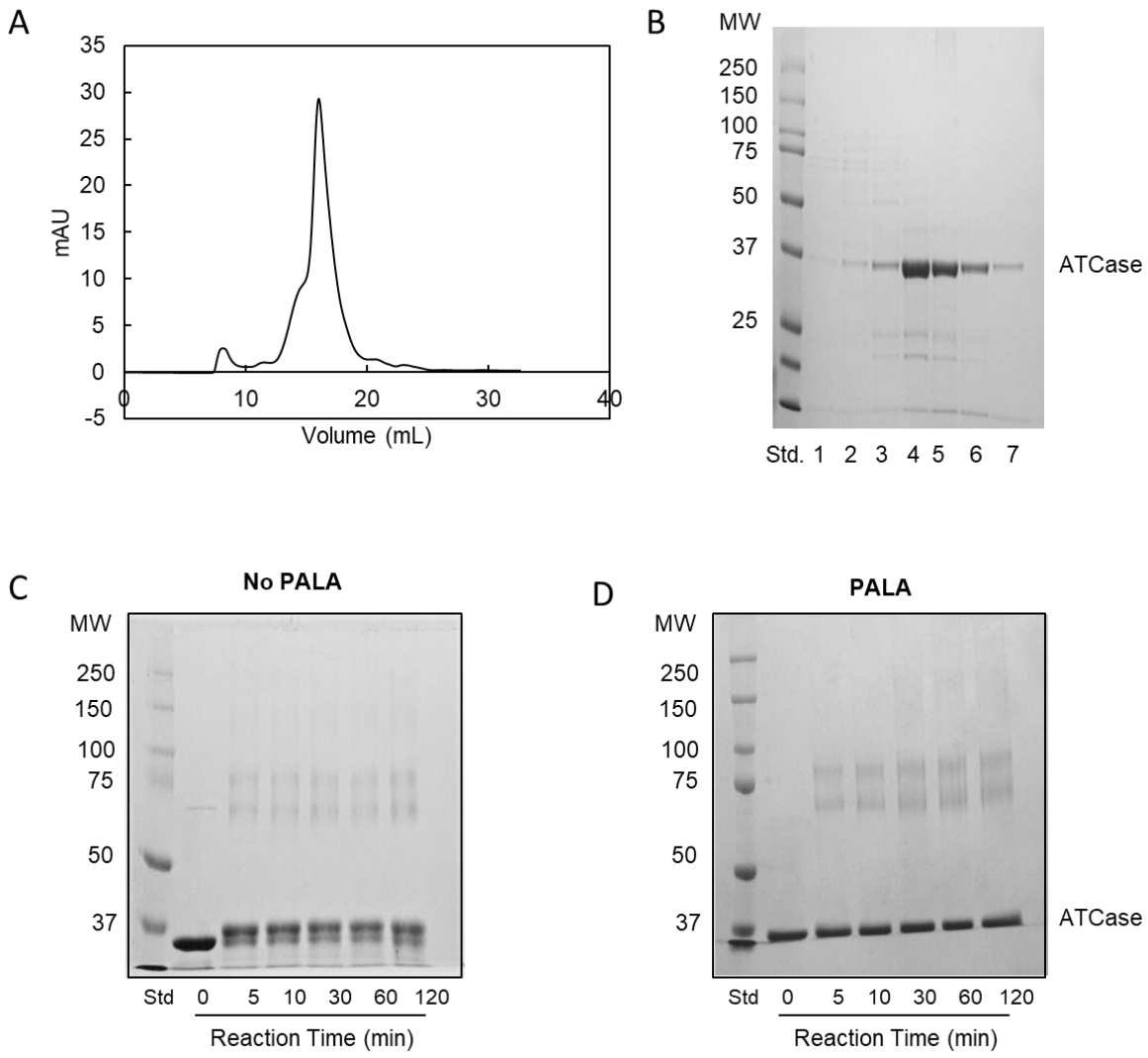

Figure 9: Trimerization of *P. aeruginosa* ATCase
A) The ATCase-pDHO preincubated with 200 μM PALA was analyzed by size-exclusion chromatography on a Superdex S200 column. B) Size-exclusion eluted fractions were analyzed on 12% SDS-PAGE; 1 and 2: fractions from the shoulder of the main peak, 3-7: fractions of the main peak. Purified ATCase was subjected to cross-linking with BS3 in the C) absence and D) presence of 200 μM PALA.

Additionally, a thermal shift assay was performed with ATCase and the ATCase-pDHO complex in the presence and absence of PALA to determine the binding of PALA to ATCase. No shift in melting temperature of ATCase was detected in the presence of PALA. However, there was a 10 °C increase in the melting temperature of the ATCase-pDHO complex in the presence of PALA suggesting that PALA only binds to ATCase when ATCase is complexed with pDHO (Fig. 10).

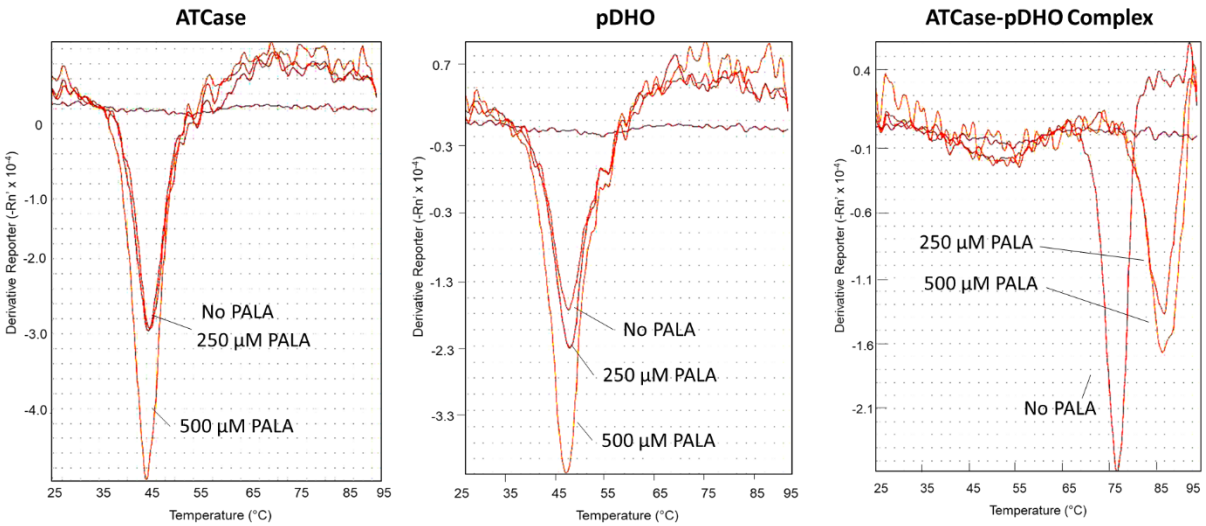

Figure 10: Thermal Stability of *P. aeruginosa* ATCase in the presence of PALA
The thermal stability of A) ATCase B) pDHO, and C) ATCase-pDHO complex, measured in the presence and absence of PALA, using 500X SYPRO Orange dye. The fluorescence was measured over a temperature range of 25 °C to 95 °C.

3.4.9 Activation of ATCase and Controlled Proteolysis by Elastase

The possibility was considered that there may be critical regions of the protein that are intrinsically disordered. The Protein Disorder Prediction System (PrDOS) was employed to identify possible disordered regions. This analysis predicted that the first 11 residues on the amino end and the last 13 residues on the carboxyl end are disordered. These disordered regions are not present in the shorter *E. coli* ATCase polypeptide. The inactivity of ATCase could be explained if the disordered extensions interfere with ATCase trimer formation in the absence of the pDHO, a pre-requisite for the enzyme's activity. The *pyr*B gene of *P. aeruginosa* ATCase without the first 11 residues (delN ATCase) and *pyr*B without the first 11 and last 13 residues (delNC ATCase) were cloned into T7 pETite vector and purified as described for the native subunit. The overexpression of mutant ATCases resulted in formation of insoluble inclusion bodies, therefore, mutant ATCases could not be tested for activity in the absence of pDHO. However, when the ATCase constructs were co- transformed and co-purified with *pyr*X gene encoding pDHO,

the mutant ATCase-pDHO complex formed and was found to be active suggesting that the truncation of the first 11 or last 13 residues did not affect the formation of ATCase-pDHO complex or ATCase activity.

Furthermore, ATCase was subjected to controlled proteolysis by elastase. The rationale for this experiment was that the elastase would cleave accessible and disordered regions of the protein. If these regions exert any inhibitory constraints, the ATCase may be activated. However, the time course of controlled proteolysis did not induce recovery of the latent ATCase activity. The elastase proteolysis of ATCase was also performed in the absence and presence of 200 µM PALA and pDHO to see if PALA protects ATCase from proteolysis. PALA did not protect ATCase from elastase proteolysis (Fig. 11A & B), whereas most of the ATCase was intact even after 120 minutes when it was subjected to elastase proteolysis in the presence of pDHO (Fig. 11C).

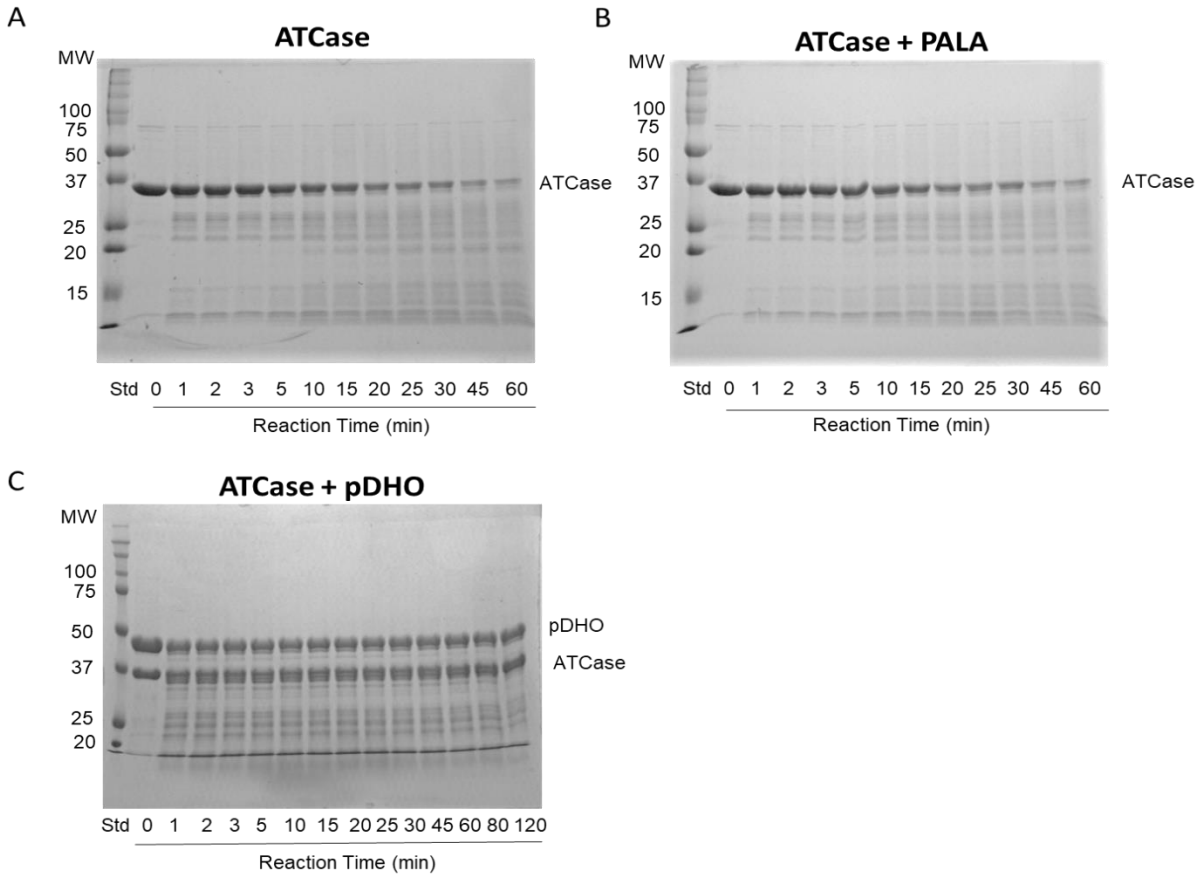

Figure 11: Controlled proteolysis of *P. aeruginosa* ATCase
Purified ATCase was subjected to proteolysis by elastase, A) in the absence of PALA or pDHO B) in the presence of 200 μM PALA and C) in the presence of 200 μM PALA and equimolar amount of pDHO. Samples were taken periodically over 60 minutes and quenched by adding 5 μL of sample buffer consisting of 12 mM Tris-HCl, pH 6.8, 5% glycerol, 0.4% SDS, 2.88 mM β-mercaptoethanol, and 0.02% bromophenol blue, and by heating for 7 min at 100°C. The samples were analyzed by electrophoresis on SDS 12% polyacrylamide gel.

3.4.9 Nucleotide Inhibition

The ATCase-pDHO complex is strongly inhibited by nucleotide tri-phosphates (Fig. 12A). Carbamoyl phosphate saturation curves showed mixed inhibition, decreasing k_{cat}, and to a lesser extent increasing K_m (Table 5). The most striking effect is a large increase in the Hill coefficient as the ATP concentration increases. When the ATCase-pDHO complex was cross-linked with BS3 in the presence of 10 mM ATP, (Fig. 12C) the complex appeared to be less stable as indicated by the appearance of fewer and smaller

intermediate species. Additionally, thermal shift data showed a negative 13°C shift of the melting temperature of the ATCase-pDHO complex in the presence of ATP - a further indication that ATP destabilizes the ATCase-pDHO complex (Fig. 12B). Additionally, the ATCase-pDHO complex was subjected to size-exclusion chromatography on S200 in the presence of 10 mM sodium pyrophosphate to determine complex dissociation. The ATCase-pDHO complex eluted as a dodecamer in the presence of sodium pyrophosphate indicating no dissociation (Fig. 12 E & F). Furthermore, the ATCase-pDHO complex was preincubated with 10 mM ATP or sodium pyrophosphate and analyzed on 7.5% native gel with 10 mM ATP or sodium pyrophosphate in the gel matrix and gel running buffer. The ATCase-pDHO complex ran as a single band on native gel indicating that the complex, although destabilized, is not completely dissociated by ATP or sodium pyrophosphate (Fig. 12 D & G). Moreover, the mutations in ATCase, delN or delNC, did not affect ATP inhibition suggesting that the ATP binding site is not present within the first 11 residues of N terminal as previously suggested.

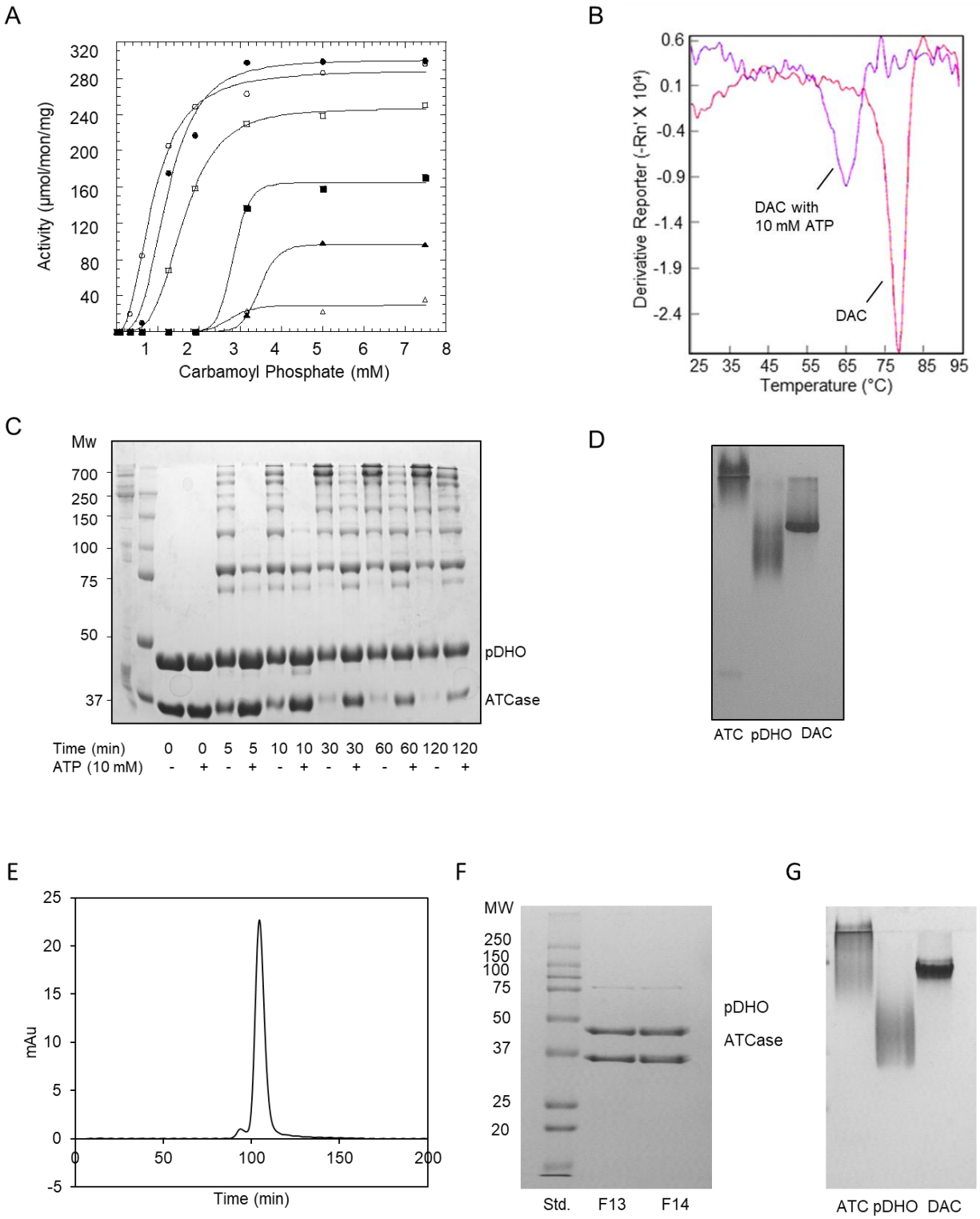

Figure 12: Nucleotide Inhibition

A) The ATCase activity of the ATCase-pDHO complex was measured with carbamoyl phosphate as the variable substrate, aspartate fixed at 8 mM in the absence of ATP (○) and in the presence of 0.5 mM (●), 1 mM (□), 2.5 mM (■), 5 mM (▲), and 10 mM (Δ) ATP. B) Preformed ATCase-pDHO complex prepared in buffer containing 50 mM Tris pH 7.5

and 200 mM NaCl was subjected to thermal shift assay using 500X SYPRO Orange dye, in the presence and absence of 10 mM ATP. The fluorescence was measured over a temperature range of 25 °C to 95 °C. C) Purified recombinant ATCase (36 µM) and pDHO (37 µM) in 50mM sodium phosphate, pH 7.5, and 500 mM NaCl, were cross-linked for the indicated times with 5 mM bis(sulfosuccinimidyl)suberate in the absence and presence of 10 mM ATP. D) Gel-filtered ATCase, pDHO, and the ATC-pDHO complex were preincubated with 10 mM ATP and subjected to native gel electrophoresis with 10 mM ATP in the gel matrix and running buffer. E) Purified recombinant equimolar ATCase and pDHO were subjected to size-exclusion chromatography on Superdex S200 column in the presence of 10 mM sodium pyrophosphate and F) the fractions corresponding to the peak were analyzed on 12% SDS-PAGE. G) Gel-filtered ATCase, pDHO, and the ATC-pDHO complex were preincubated with 10 mM sodium pyrophosphate and subjected to native gel electrophoresis with 10 mM sodium pyrophosphate in the gel matrix and running buffer.

Table 5: ATP Inhibition of *P. aeruginosa* ATCase

ATP mM	V_{max} µmol/min/mg	K_m mM	n_H
0	289 ± 5.0	0.88 ± 0.03	2.4
0.5	300 ± 10	1.22 ± 0.07	3.2
1.0	247 ± 2.7	1.62 ± 0.02	3.8
2.5	164 ± 2.6	2.83 ± 0.32	14.7
5	96.6 ± 1.1	3.53 ± 0.10	12.7
10	29.1 ± 2.7	2.76 ± 0.48	10.3

3.4.10 Structure of *P. aeruginosa* delN ATCase-pDHO Complex

The crystal structure of *P. aeruginosa* delN ATCase-pDHO complex at 2.47 Å has been refined to a final R_{work} value of 28% and a R_{free} value of 33%. The crystal structure belongs to space group H32 with unit cell parameters a = b = 171.65, c = 159.53 Å. The crystal structure contains a heterodimer of one delN ATCase, one pDHO, and two TEW molecules in its crystallographic asymmetric unit (Fig. 13A).

The *P. aeruginosa* delN ATCase chain has an overall fold like the other known ATCases with carbamoyl phosphate (residues 1-149) and aspartate (residues 166-298) domains connected by a hinge region (residues 150-165, 299-323). delN ATCase chain lacks continuity of electron density at 1.0 σ for the main chain of residues 45-49, 56-57, 92-99, 212, 242-251, and 272-273. Superimposition of *A. aeolicus* ATCase and *P. aeruginosa* ATCase gave an RMSD (root mean square deviation) of 1.75 Å for 283 Cα atoms. Saturating concentration of 200 μM PALA was added to the delN ATCase-pDHO solution prior to crystallization yet density for PALA was not found in the active site. Instead unambiguous density for TEW ([TeW6O24]6−) was present in the active site (Fig. 13C). TEW is a tellurium-centered Anderson-Evans polyoxotungstate that was present as an additive in the crystallization solution. This highly charged molecule with a total net charge of -6 interacts with positively charged regions of the protein and is known to stabilize flexible regions while maintaining the integrity of the protein [125]. TEW interacts covalently and through hydrogen bond interactions with the residues in the ATCase active site (Fig. 13D). TEW interacts through hydrogen bonding with a number of residues in the active site of ATCase including Ser 68, Arg 70, Arg 120, Arg 239 and Glu 243, but most importantly, TEW also interacts with residues of the 90's loop from the adjacent monomer including Ser 95 and Ser 97, thus stabilizing the active site and delN ATCase trimer. PALA has a very high affinity for the active site of ATCases – e.g. a K_i of 27 nM for *E. coli* ATCase [126]. The displacement of PALA by TEW in the active site of *P. aeruginosa* delN ATCase implies that TEW has a higher affinity for delN ATCase than PALA and that TEW may have an inhibitory role on *P. aeruginosa* delN ATCase.

P. aeruginosa pDHO chain folds into a TIM barrel domain (residues 56-365) connected to β-stranded adjacent domain (residues 1-55, 366-423) like other known DHOases. The pDHO chain lacks continuity of electron density for the main chain of residues 34-42. Superimposition of *A. aeolicus* DHOase and *P. aeruginosa* pDHO gave an RMSD of 1.38 Å for 420 Cα atoms. The second TEW molecule in the asymmetric unit was found to interact with pDHO through hydrogen bonding with Arg 71 and Arg 97.

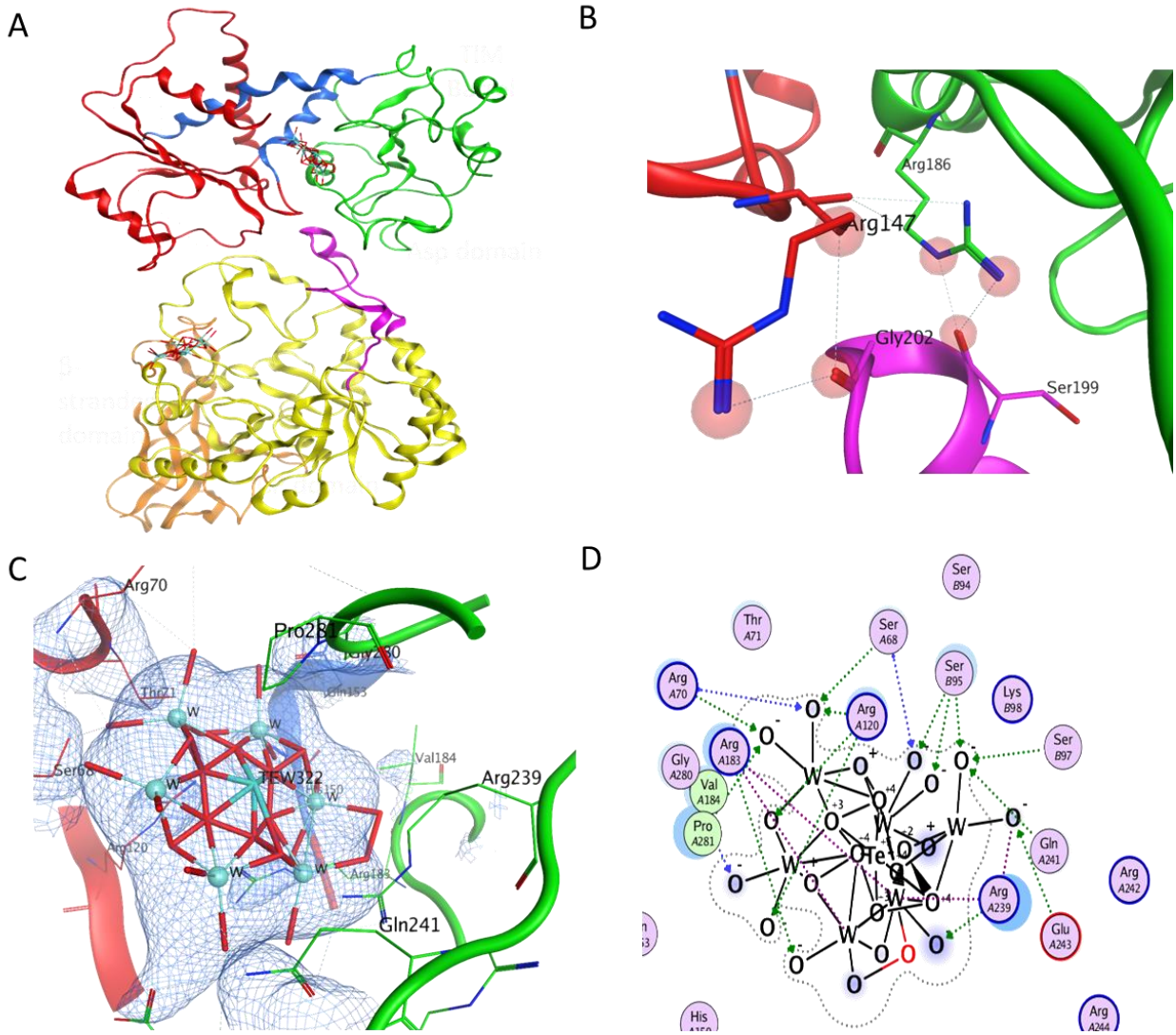

Figure 13: Crystal Structure of *P. aeruginosa* delN ATCase and pDHO
A) The single molecule of *P. aeruginosa* delN ATCase and pDHO with two molecules of TEW in the asymmetric unit. CP and Asp domains and hinge region of ATCase are

colored in red, green, and blue, respectively. TIM-barrel and β-stranded domains of pDHO are colored in yellow and orange respectively, whereas pDHO loop A is colored in purple, loop B in cyan, and loop C in white. B) Hydrogen bond interactions between pDHO loop A (magenta) and the interdomain cleft of delN ATCase. C) Electron density map of TEW in the active site of delN ATCase. D) MOE ligand interaction map of TEW with the delN ATCase active site residues of chain A and chain B.

The unit cell of this crystal space group contains 18 copies of the heterodimer delN ATCase and pDHO. The Protein Interfaces, Surfaces, and Assemblies service (PISA) [119] at the European Bioinformatics Institute identified a dodecameric assembly of delN ATCase and pDHO based on the largest buried surface area and the largest numbers of stabilizing interactions. Each delN ATCase subunit interacts with five other chains including two delN ATCases in the same trimer (A2 and A3) and three pDHO (D1, D4, and D2) in the central torus. In *A. aeolicus,* loop A at the top of the TIM barrel of DHOase plays an important role as 12 residues from this loop contribute to the interface with ATCase [15, 39]. *A. aeolicus* ATCase interacts with DHOase through 9 hydrogen bond interactions and 7 salt bridges. In *P. aeruginosa,* pDHO loop A also interacts with residues in the delN ATCase interdomain cleft. However, in *P. aeruginosa*, only three hydrogen bond interactions were found between pDHO loop A (D1) and ATCase (A1). Loop A Ser 199 interacts with ATCase Arg 186 and loop A Gly 202 interacts with ATCase Arg 147. ATCase also interacts with another chain of pDHO (D4) through ATCase Arg 206 – pDHO Thr 172 , ATCase Glu255 – pDHO Glu138, and ATCase Thr207 – pDHO Glu168. Lastly, ATCase interacts with pDHO D4 through hydrogen bond between ATCase Gly 285 – pDHO Arg 71. Each pDHO chain interacts with three other chains; its delN ATCase partner (A1) and two other pDHO chains (D4 and D5) in the opposite trimer. All chain interactions calculated by PISA [119] are depicted in Fig. 14 and listed in Table 6.

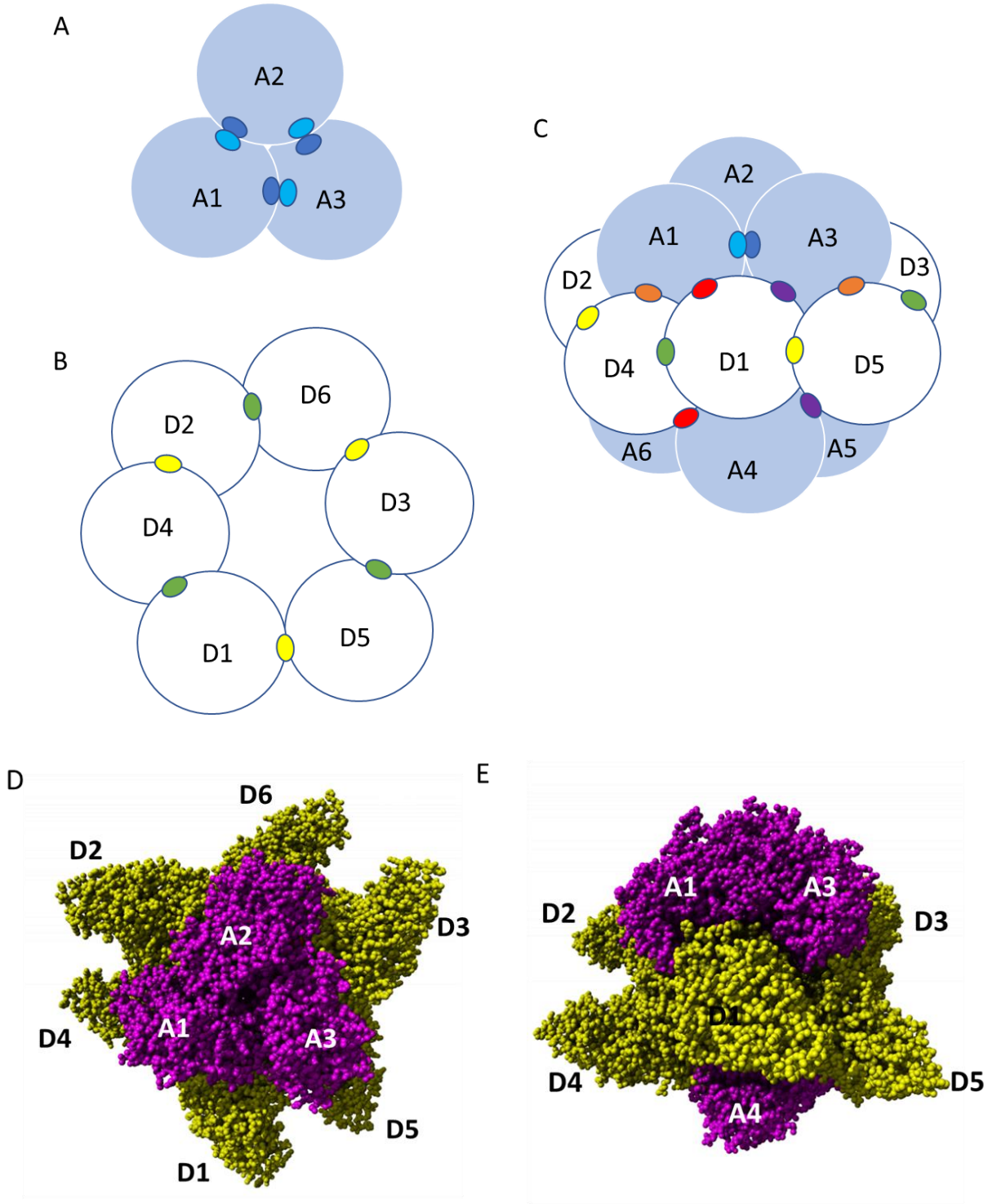

Figure 14: The dodecamer of *P. aeruginosa* ATCase and pDHO
A schematic diagram showing the interfaces listed in Table 6, A) the delN ATCase trimer, B) the pDHO hexamer, and C) the dodecamer. The delN ATCase (purple) and pDHO (yellow), D) top view with three ATCase chains labelled A1-A3 and three pDHO chains attached to the top trimer are labelled D1-D3, H) sideview of the dodecamer rotated 90 degrees horizontally.

Table 6: Chain Interfaces Calculated by PISA

Interface	Chain1:Chain 2	Residues	Buried Area	H-bonds	Salt bonds	CSS[a]	Color
1	pDHO1:pDHO4	27:26	1051	18	12	0.148	Green
2	ATC1:ATC2	24:26	889	9	1	0.307	Cyan
(2)	ATC1:ATC3	24:26	889	9	1	0.307	Blue
3	ATC1:pDHO1	28:24	790	3	0	0.287	Red
4	ATC1:pDHO4	14:18	543	2	0	0.176	Orange
5	pDHO1:pDHO5	12:12	365	2	4	0.037	Yellow
6	ATC3:pDHO1	6:3	124	1	0	0.011	Purple

[a]Complexation significance score

With successful crystallization of *P. aeruginosa* delN ATCase trimer as a part of the dodecamer, *P. aeruginosa* delN ATCase monomer-monomer ATCase interactions were analyzed using the protein interfaces service from PISA [119] and compared with *E.coli* (PDB: 1Q95), *Bacillus subtilis* (PDB: 3R7D), *S. aureus*, *A. aeolicus* (PDB: 3D6N), and human ATCase (PDB: 5G1N). Although $\Delta^{i}G$ or the free energy of solvation and the buried surface area upon interface formation were not very different, the number of salt bonds and hydrogen bonds was significantly lower for *P. aeruginosa* delN ATCase compared to all other ATCases as shown in Table 7. This suggests that although the hydrophobic interactions might be conserved, *P. aeruginosa* ATCase has very few electrostatic interactions at the monomer-monomer interface and most likely the reason why it is a monomer in solution in the absence of pDHO.

Table 7: Monomer-Monomer Interface Interactions

ATCase	# H-bonds	# Salt bonds	Buried Area ($Å^2$)	Δ^iG (kcal/mol)
E. coli	16	12	1058.8	-7.6
B. subtilis	14	9	941.0	-6.4
S. aureus	19	8	1089.3	-10.2
A. aeolicus	19	8	958.9	-5.5
H. sapiens	18	17	1075.6	-7.7
P. aeruginosa	9	1	889.4	-4.1

3.4.11 Inhibition of *P. aeruginosa* ATCase by TEW

Due to the displacement of PALA by TEW from the active site of *P. aeruginosa* ATCase during the crystallization process, ATCase assay was performed to assess the effect of TEW on *P. aeruginosa* ATCase activity. TEW inhibited *P. aeruginosa* ATCase with an IC_{50} in the range of 0.1 – 1 μM (Fig. 15). The assay will have to be repeated to determine a more accurate IC_{50} value, nonetheless, TEW is a potent inhibitor of *P. aeruginosa* ATCase.

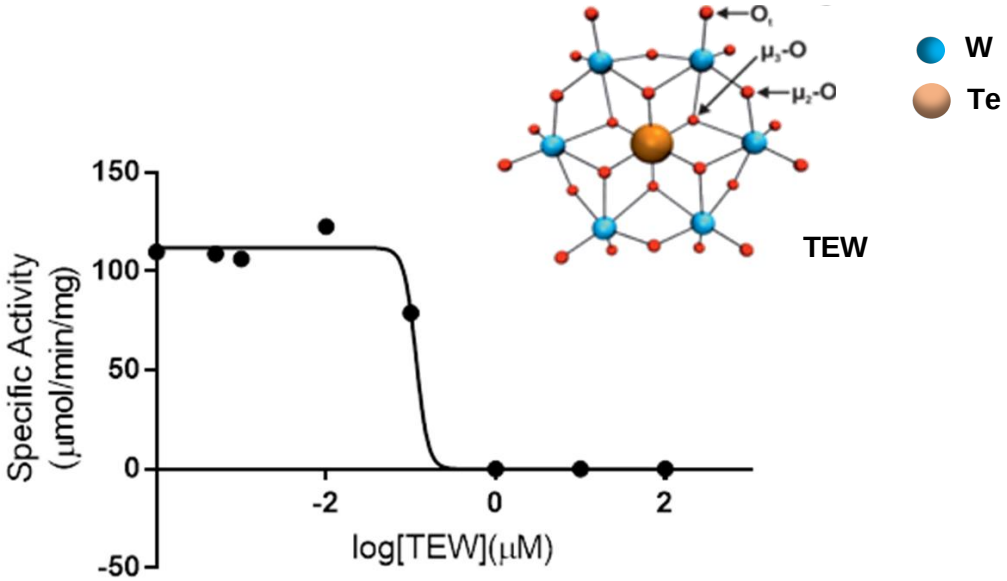

Figure 15. IC_{50} of TEW against *P. aeruginosa* ATCase
P. aeruginosa ATCase assay was performed with 2.5 mM carbamoyl phosphate, 2 mM aspartate, and increasing concentrations of TEW.

3.5 Discussion

Previous studies have shown that *Pseudomonas* ATCases have some unusual properties. All ATCase catalytic subunits from bacteria, fungi, and plants [127-129] have homologous sequences, have the same catalytic residues and mechanism and form stable catalytically active trimers. Although Schurr et al. [20] did not isolate the ATCase subunit they showed the ATCase activity in *Pseudomonas putida* was dependent on the presence of the pDHO domain and correctly concluded that it was necessary for the stability of the ATCase-pDHO complex. In this study we have cloned and expressed both the *P. aeruginosa* inactive ATCase and pDHO subunits and found that a relatively stable dodecameric complex with full ATCase activity could be reconstituted when the two subunits were mixed in a 1:1 stoichiometric molar ratio.

Unlike all other ATCase that have been previously studied, the ATCase chains from these *Pseudomonas* species are monomeric and do not assemble into a catalytically active trimer unless the pDHO subunit is present. No significant amount of the ATCase trimer could be detected by size-exclusion chromatography or by chemical crosslinking. In contrast, chromatography indicated that the pDHO subunit formed a stable dimer, although the dimer did not crosslink because there are no appropriately positioned lysine residues at the dimer interface as known from the crystal structure of *P. aeruginosa* delN ATCase-pDHO dodecamer. The failure to form a stable ATCase trimer accounts for its lack of catalytic activity since the active site of every known ATCase requires a conserved serine and lysine (Ser80 and Lys840 in *E. coli*) from the adjacent subunit that participates in catalysis.

The three very important interactions between *E. coli* ATCase monomers in the catalytic trimer have been identified to be Lys-41, Asp-100, and Asp-90 of one monomer that form salt links with Glu-37, Arg-65, and Arg-269 of the adjacent subunit [130, 131]. Multiple sequence alignment of *P. aeruginosa* ATCase with other trimeric ATCases (Fig. 16) showed that two of the three interactions are partially conserved in *P. aeruginosa*.

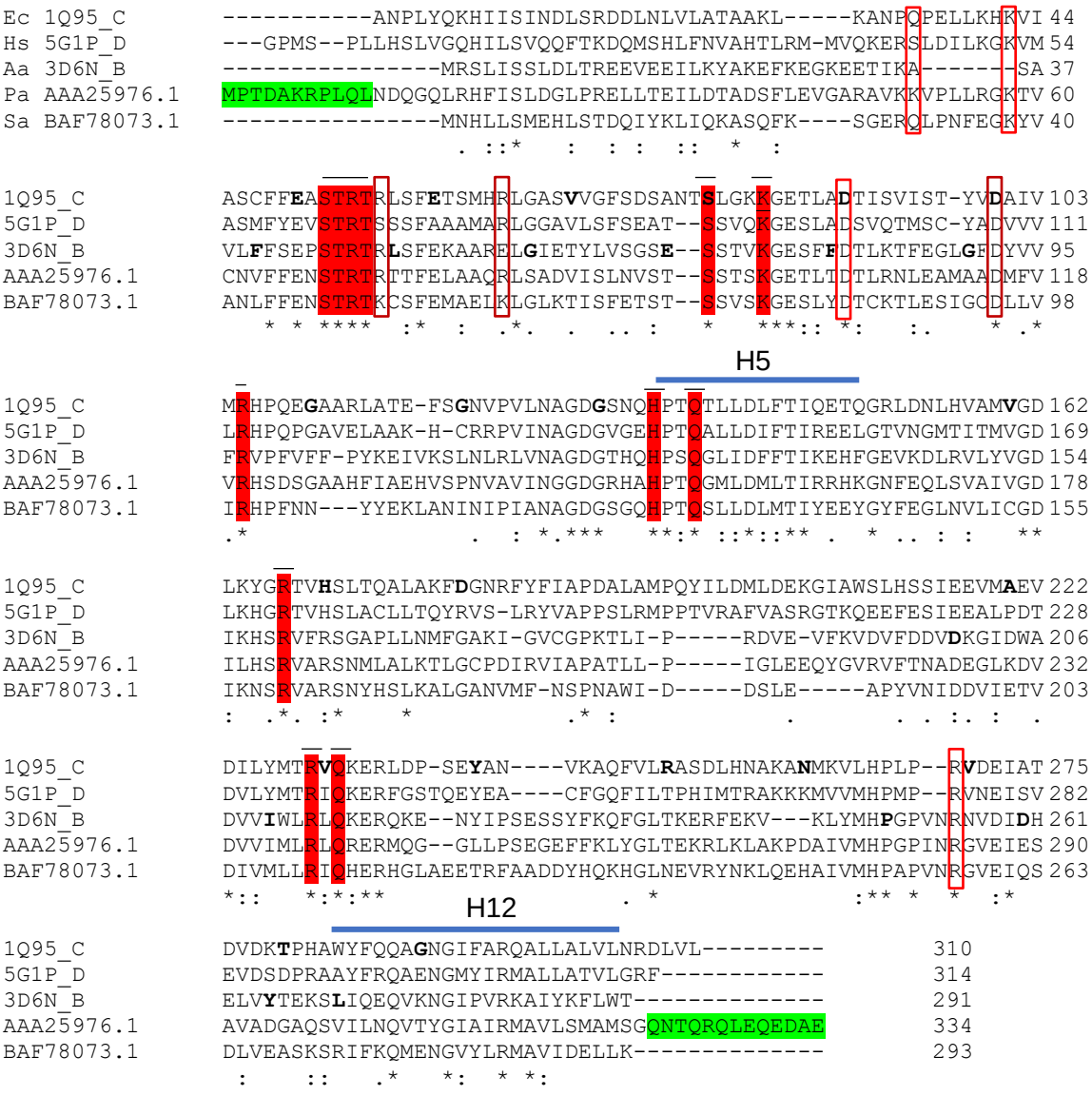

Figure 16: Sequence Similarity of ATCases
A CLUSTAL O (1.2.4) multiple sequence alignment of ATCase catalytic chain or domain of ATCase from *E. coli* (Ec), *Homo sapiens* (Hs), *Aquifex aeolicus* (Aa), *Pseudomonas aeruginosa* (Pa) and *Staphylococcus aureus* (Sa). Active site residues are highlighted in red; H5 and H12 represent the residues that connect the carbamoyl phosphate and aspartate domains of ATCase; residues involved in monomer-monomer interactions are boxed in red; amino and carboxyl end extensions of *P. aeruginosa* ATCase are highlighted in green.

CD analysis showed that both the isolated subunits can spontaneously assume a typical secondary structure, although neither ATCase nor pDHO is very stable with melting temperatures as determined by the thermal shift assay were 38°C and 44°C respectively. Formation of the complex appreciably stabilizes the protein, raising the

melting temperature to 77°C. Time-dependent chemical crosslinking of the reconstituted dodecamer of the *A. aeolicus* ATCase-DHOase complex showed a progressive disappearance of the monomers and the formation of the 240 kDa hexamer which gradually disappears with the formation of the 480 kDa dodecamer. In contrast, crosslinking of preformed *P. aeruginosa* ATCase-pDHO gave a complex but highly reproducible pattern of 8 bands, that gradually gave way to species of higher molecular mass. This pattern may have resulted from the intrinsic instability of the subunits and the lack of pDHO crosslinking.

As reported previously [123] micromolar levels of nucleotide tri- and di-phosphates competitively inhibit *P. fluorescens* when carbamoyl phosphate is limiting (7.5-30 µM). At higher carbamoyl phosphate concentrations (10 mM), nucleotides are non-competitive inhibitors [132]. The regulatory logic of these phenomena is elusive. *E. coli* ATCase is allosterically inhibited by UTP and CTP and activated by ATP. The rationale is that this regulatory mechanism provides a balance between the synthesis of pyrimidines and purines. However, *P. aeruginosa* ATCase is inhibited by both pyrimidines and purines. The inhibitors tend to shift the saturation curve to higher substrate concentrations and increase cooperative substrate binding and Hill coefficient. The Monod, Wyman and Changeux model stipulates that the upper limit of the Hill coefficient equals the number of substrate binding sites. The Hill coefficients for *P. aeruginosa* ATCase here and in a previous study [21] far exceed the number of effector binding sites suggesting that the observed sigmoidicity does not reflect true homotropic or cooperative substrate binding. The ATP binding site was previously shown to be located on the ATCase catalytic subunit by affinity labeling with the radiolabeled ATP analog, [^{3}H]-FSBA. Previous studies [124]

provided evidence that ATP binds to the 11 residue extension on the amino end of the catalytic polypeptide. However, subcloning of deletion mutants lacking the extension on the amino end and the carboxyl ends of the protein were inhibited by ATP. We conclude that the nucleotide inhibition is a consequence of the nucleotide induced destabilization of the ATCase-pDHO complex and does not represent an allosteric regulatory mechanism. How then is pyrimidine biosynthesis regulated in *P. aeruginosa?* A possible explanation is that carbamoyl phosphate synthetase (CPSase) which provides the ATCase substrate, carbamoyl phosphate, regulates ATCase. *P. aeruginosa* CPSase. Is controlled by metabolites in the arginine biosynthetic pathway but is also feedback inhibited by CTP [133].

The crystallization of *P. aeruginosa* delN ATCase-pDHO in space group H32 revealed one delN ATCase, one pDHO, and two TEW in the asymmetric unit. The biological assembly of *P. aeruginosa* subunits is a dodecamer consisting of six copies of both subunits as shown by size-exclusion and cross-linking experiments. Crystallization of delN ATCase-pDHO in the presence of TEW resulted in displacement of PALA and binding of TEW to the active site of delN ATCase. TEW interacts through hydrogen bonding with the active site residues of the main chain as well as 90's loop from the adjacent monomer suggesting that TEW stabilizes the delN ATCase trimer. TEW was found to be a potent inhibitor of *P. aeruginosa* ATCase with an IC_{50} value in the low micromolar range.

In summary, although the isolated ATCase from *P. aeruginosa* has a well-defined secondary structure, it is relatively unstable and does not self-associate to form a stable trimer. Association with the pDHO subunit is therefore necessary to stabilize the

catalytically active timer and to form the dodecamer. ATP induced destabilization of the ATCase-pDHO complex accounts for the inactivation of the ATCase catalytic subunit.

3.6 Future Directions

It is important to obtain the crystal structure of *P. aeruginosa* ATCase and pDHO in the absence of TEW to determine if TEW led to distortion of DAC in any way. The inhibitory effect of TEW on *P. aeruginosa* ATCase should be explored more thoroughly. Experiments to be performed:

- Crystallization of apo ATCase-pDHO complex
- Co-crystallization of ATCase-pDHO complex in the presence of ATP to determine ATP binding site
- *P. aeruginosa* and *A. aeolicus* ATCase activity assay in the presence of TEW
- Crystallization of *P. aeruginosa* and *A. aeolicus* ATCase in presence of TEW
- Crystallization of *A. aeolicus* ATCase-DHOase (DAC) in the presence of TEW

CHAPTER 4: ASPARTATE TRANACARBAMOYLASE IN *STAPHYLOCOCCUS AUREUS*

4.1 Abstract

Staphylococcus aureus is a commensal pathogen that has become a serious threat due to its emerging multi-drug resistance, especially to methicillin and vancomycin. The aspartate transcarbamoylase (ATCase) of this organism is a trimer comprised of three 33 kDa catalytic chains. We have cloned the *pyr*B gene of *S. aureus* encoding ATCase, overexpressed the clone in *E. coli* and purified the protein using nickel affinity chromatography. Chemical cross-linking and size-exclusion chromatography showed that ATCase is a 99 kDa homotrimer. The carbamoyl phosphate saturation curve of ATCase is hyperbolic whereas the aspartate saturation curve is sigmoidal. Furthermore, the ATCase activity was inhibited by mM amounts of ATP with a decrease in V_{max} and slight change in the K_m indicating non-competitive inhibition of ATCase. Moreover, cross-linking, size-exclusion, and enzyme activity assays showed no evidence of interaction of ATCase with dihydroorotase (DHOase), the third enzyme in the pathway, which often forms a complex with ATCase. This study also presents the three-dimensional structure of *S. aureus* ATCase bound to PALA, N-phosphonacetyl-L-aspartate, a bi-substrate inhibitor of the enzyme. The X-ray structure of *S. aureus* ATCase closely resembles the *Bacillus subtilis* homotrimeric ATCase.

4.2 Introduction

Staphylococcus belongs to Micrococcaceae family of eubacteria that naturally colonizes the human skin. *Staphylococcus aureus* is a leading cause of health-care associated and community-associated infections in immunocompromised individuals. There is an increased morbidity and mortality associated with *S. aureus* infection when it

manifests into bacteremia, infective endocarditis, metastatic infection, and/or sepsis [134, 135]. Emerging resistance of *S. aureus* to methicillin and vancomycin poses an urgent need for the development of new antimicrobial drugs. In the design of therapeutic strategies, pyrimidine metabolism of this organism has not been thoroughly explored.

Aspartate transcarbamoylase (ATCase; EC 2.1.3.2) catalyzes the reaction of carbamoyl phosphate (CP) and aspartate to form N-carbamoyl-l-aspartate (CA) and inorganic phosphate [7] a key step in *de novo* pyrimidine biosynthesis. ATCase catalyzes the same reaction in all organisms but is highly polymorphic. In mammals, the first three enzymes of the pyrimidine biosynthesis are consolidated on a single polypeptide, called CAD, combining carbamoyl phosphate synthetase (CPSase), aspartate transcarbamoylase, and dihydroorotase (DHOase) [136]. The 243 kDa CAD then self-associates into a hexamers and higher oligomers [137] exceeding a molecular mass of 1.4 MDa [2].

We report here the overexpression, purification, and crystallization of *S. aureus* ATCase. We have also determined the oligomeric state of the protein, the kinetic properties, and whether it associates with DHOase. *S. aureus* is a 99 kDa trimer of catalytic chains and it does not associate with DHOase. The X-ray structure of *S. aureus* ATCase shares a high sequence similarity with *B. subtilis* ATCase and both ATCases have a very similar tertiary structure. *S. aureus* ATCase was found to be inhibited by nucleotides indicating allosteric regulation.

4.3 Materials and Methods

4.3.1 Crystallization, Data Collection, and Structure Refinement

Gel-filtered ATCase in 50 mM Tris-HCl, pH 7.5, 200 mM NaCl, and 1 mM dithiothreitol was concentrated in the Amicon Ultra-15 centrifugal filter units (EMD Millipore) to a final concentration of 8.85 mg/mL as determined by the Lowry method [29] using bovine albumin serum as a standard. Prior to crystallization, N-phosphonacetyl-L-aspartate or PALA was added to protein at a final concentration of 200 µM. All crystals were grown at room temperature using the sitting-drop, vapor diffusion method. PALA-bound ATCase crystals were grown by mixing 1 µL of ATCase-PALA and 1 µL of 2 M ammonium sulfate, 5% polyethylene glycol 400, and 0.1 M sodium 2-(N-Morpholino) ethanesulfonic acid or MES, pH 6.5. Crystals that grew within 10 days were then used for preparing seed stock for performing subsequent seeding experiment. A 2 µL drop solution, including the crystals, was added to 50 µL of reservoir solution into the microcentrifuge tube with the Seed Bead (Hampton), which was then vortexed for 3 minutes, and used as seed stock. One µL of 1:4 diluted seed stock was mixed with 1 µL of 8.85 mg/mL ATCase to allow crystal growth at room temperature. The best diffracting cubic crystals grew to 0.1 mm x 0.1 mm within 2-4 days. The crystals were soaked in a cryoprotectant solution consisting of mother liquor and 20% ethylene glycol prior to freezing in liquid nitrogen. X-ray diffraction data were collected at Advanced Photon Source, Argonne National Laboratory in Illinois. The crystals belong to the space group $P3_221$ and diffracted to 2.27 Å resolution, with three ATCase molecules in the asymmetric unit. The structure was solved by the molecular replacement method with the program PHASER within the Phenix suite [114] using crystal structure of unliganded ATCase from *Bacillus subtilis*, PDB: 3R7D, [26] as the search model. Structure modeling was carried out in COOT [115] and refinement was performed using Phenix and PDB-Redo [116].

4.4 Results

4.4.1 Expression and Purification of *S. aureus* ATCase and DHOase

The *pyr*B gene encoding *S. aureus* ATCase and *pyr*C gene encoding DHOase was cloned into pmcsg19c vector incorporating a 6x his-tag on the amino terminus of the protein. The resulting constructs was transformed into *E. coli* Hi-Control BL21(DE3) cells. The proteins were expressed and purified using Ni^{2+} affinity chromatography as described in chapter 2. ATCase and DHOase were soluble and expressed at 50 mg/liter of culture (Fig. 17A & B).

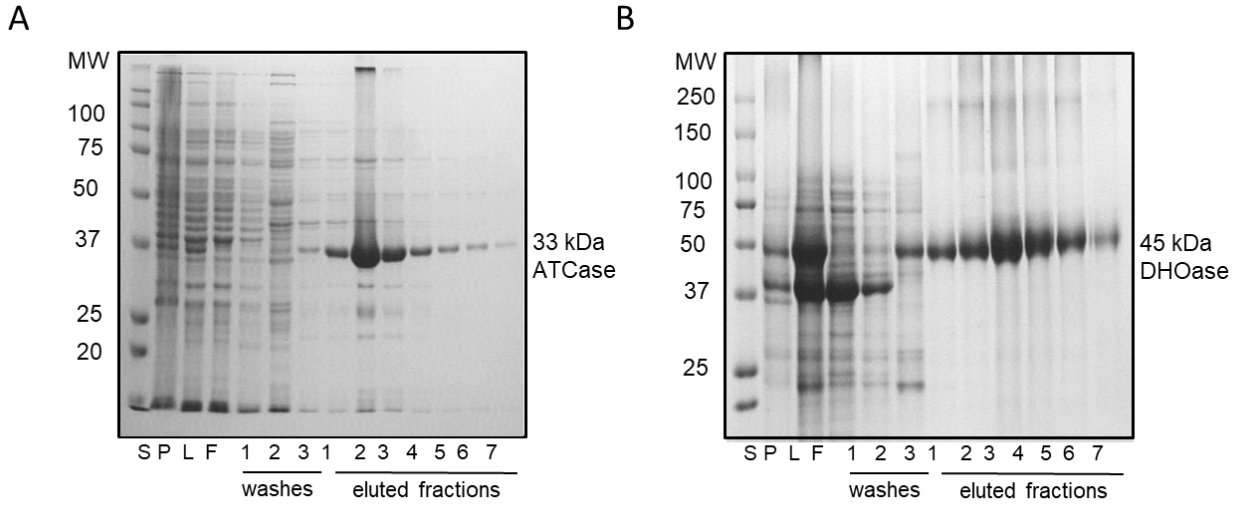

Figure 17: Expression and Purification of *S. aureus* ATCase and DHOase
The *pyr*B gene encoding *S. aureus* ATCase pmcsg19c was cloned into the expression vector that incorporates a 6xHis tag on the amino end of the recombinant proteins. The resulting constructs were transformed separately into *E. coli* Hi-Control BL21(DE3) cells (Lucigen). The transformants were grown at 37°C in LB medium until OD600 of 0.6 and induced with 0.1 mM IPTG overnight (16-18 hours) at 20°C. The cells were harvested and resuspended in 50 mM sodium phosphate and 0.5 M NaCl, pH 7.5, and lysed by sonicating and French pressing once. The cell lysate was centrifuged at 12,000 x g for 45 minutes at 4°C. The supernatant was applied to 5.0-ml Ni^{2+} affinity column. The column was washed with 10 column volumes with increasing concentration of imidazole up to 100 mM. the proteins were eluted in 5-ml aliquots with 250 mM imidazole in the same buffer. The fractions were analyzed by electrophoresis on 12% SDS-PAGE Laemmeli gels, A) ATCase and B) DHOase.

4.4.2 Oligomeric Structure of ATCase and DHOase

On SDS-PAGE, under denaturing conditions, ATCase had an estimated molecular mass of 33 kDa, in agreement with that calculated mass from the amino acid sequence. Nickel column purified ATCase was then subjected to gel filtration chromatography on a calibrated Superdex S200 column. ATCase eluted as a single species with a molecular mass of 99 kDa indicating that it is a trimer under non-denaturing conditions (Fig. 18A & B). This result was confirmed by chemical cross-linking with BS3 (bis(sulfosuccinimidyl)suberate). The time course of the cross-linking reaction of ATCase showed a gradual formation of ATCase dimer and then trimer with disappearance of the monomeric species (Fig. 18E).

DHOase had an estimated molecular weight of 45 kDa but eluted as a single species with a molecular weight of 90 kDa indicating that DHOase is a dimer in solution (Fig. 18C & D). Upon cross-linking DHOase with BS3, there is a gradual increase in dimeric species and a decrease in monomeric species when analyzed on 4-20% gradient SDS-PAGE (Fig. 18F).

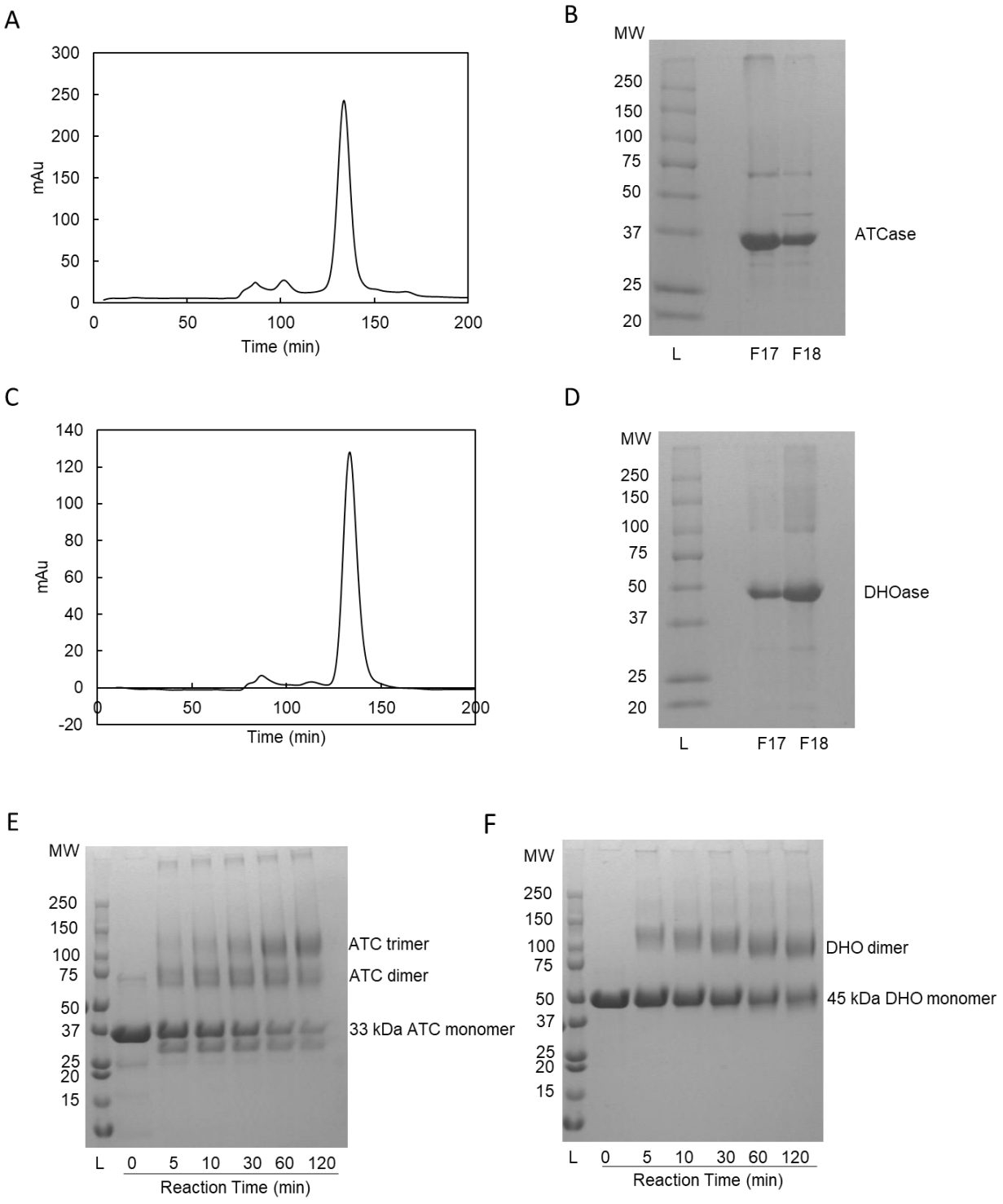

Figure 18: Oligomeric Structure of *S. aureus* ATCase and DHOase

A) Purified *S. aureus* ATCase was subjected to size-exclusion chromatography on a Superdex S200 Akta column and B) fractions 17 and 18 corresponding to the ATCase peak were analyzed by 12% SDS-PAGE. C) Purified *S. aureus* DHOase was subjected to size-exclusion chromatography on a Superdex S200 Akta column and D) fractions 17

and 18 corresponding to the DHOase peak were analyzed by 12% SDS-PAGE. E) Purified recombinant ATCase (45 µM) and F) DHOase (45 µM) in 50mM sodium phosphate, pH 7.5, and 500 mM NaCl, were cross-liked for the indicated times with 5 mM bis(sulfosuccinimidyl)suberate. The reaction was quenched by adding 10 ul of 1M Tris-HCl, pH 8. Cross-linked species were analyzed by electrophoresis on 4-15% gel.

4.4.3 ATCase Steady State Kinetics

The steady state kinetics parameters were obtained from carbamoyl phosphate and aspartate saturation curves of ATCase. The carbamoyl phosphate curve of ATCase was hyperbolic (Fig. 19A). A least square fit of the Michaelis-Menten equation gave a K_m for carbamoyl phosphate ($[S]_{0.5}$) of 2.4 mM and a V_{max} of 305 µmoL/min/mg (Table 8). The aspartate saturation curve of ATCase was sigmoidal and indicated cooperative substrate binding with a K_m for aspartate ($[S]_{0.5}$) of 4.5 mM and a V_{max} of 287 µmoL/min/mg with a Hill-coefficient of 2 (Fig.19B, Table 8). The bi-substrate inhibitor N-phosphonacetyl-L-aspartate designed to resemble the *E. coli* ATCase transition state is also a potent inhibitor of *S. aureus* ATCase (data not shown).

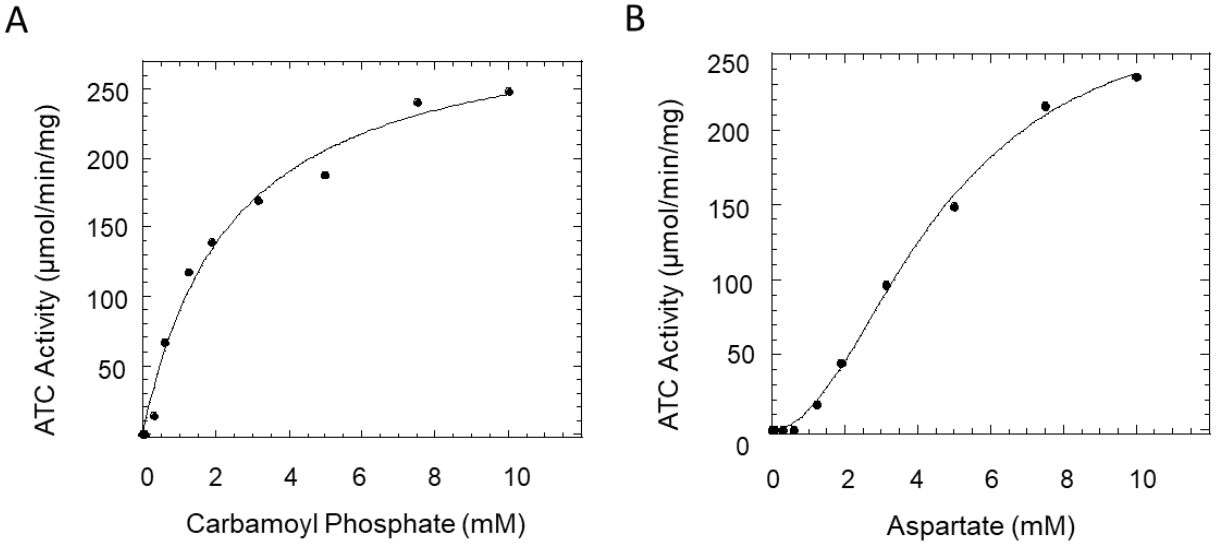

Figure 19: Steady State Kinetics of *S. aureus* ATCase
The ATCase activity was measured as described in chapter 2, A) aspartate fixed at 8 mM and carbamoyl phosphate as the variable substrate. The carbamoyl phosphate saturation curve was fit to the Michaelis-Menten equation, $v=V_{max}[S]/([S] + K_m)$. B) carbamoyl

phosphate fixed at 5 mM and aspartate as the variable substrate. The aspartate saturation curve was fit to the Hill equation: $v=V_{max}[S]^n/(K_m^n + S^n)$.

Table 8: Steady State Kinetics of *S. aureus* ATCase

Variable Substrate	Carbamoyl Phosphate (CP)	Aspartate (Asp)
K_m (mM)	2.42 ± 0.41	4.57 ± 0.35
V_{max} (µmol/min/mg)	305.73 ± 19.07	287.11 ± 16.81
k_{cat} (s^{-1})	168.15	157.91
k_{cat}/K_m ($s^{-1}M^{-1}$)	6.9×10^4	3.4×10^4
Hill coefficient	-	2.00 ± 0.16

4.4.4 Nucleotide Inhibition

S. aureus ATCase was found to be inhibited by ATP (Fig. 20). ATCase activity was measured by keeping aspartate constant, varying carbamoyl phosphate concentration, and increasing ATP concentration up to 10 mM. Carbamoyl phosphate saturation curves indicated non-competitive inhibition decreasing V_{max} with a little change in K_m up to 10 mM ATP (Table 9). At 10 mM ATP, the increase in K_m may indicate that the ATP might be starting to occupy the active site.

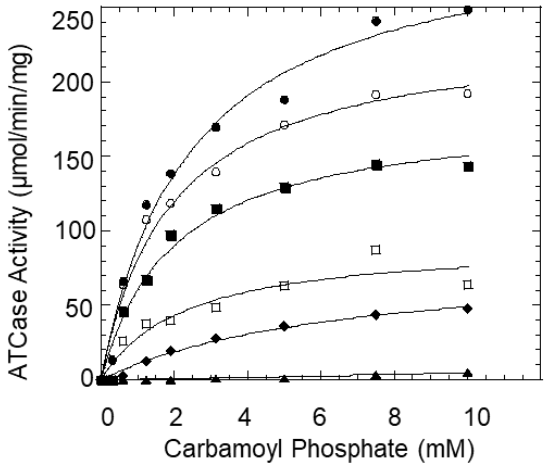

Figure 20: ATP Inhibition of *S. aureus* ATCase
The ATCase activity was measured with carbamoyl phosphate as the variable substrate, aspartate fixed at 8 mM in the absence of ATP (●) and in the presence of 1 mM (○), 2.5 mM (■), 5 mM (□), 5 mM (♦), and 10 mM (▲) ATP.

Table 9: ATP Inhibition

ATP mM	V_{max} µmol/min/mg	K_m mM
0	305.7 ± 19.0	2.42 ± 0.41
1.0	235.04 ± 18.3	1.93 ± 0.44
2.5	180.24 ± 13.6	1.99 ± 0.44
5	92.8 ± 13.3	2.29 ± 0.92
10	81.8 ± 9.3	6.72 ± 1.44

4.4.5 Association of Dihydroorotase

To examine whether *S. aureus* ATCase associates with dihydroorotase (DHOase), nickel column purified recombinant ATCase and DHOase proteins were mixed in a 1:1 ratio and rotated overnight in 4°C. This mixture was then subjected to size-exclusion chromatography on Superdex S200 column. ATCase and DHOase did not form a

complex as evidenced by elution of both proteins in a single peak comprised of both the ATCase trimer (99 kDa) and DHOase dimer (90 kDa) (Fig. 21A & B). Furthermore, an equimolar ratio of ATCase and DHOase mix was subjected to cross-linking with BS3. The monomeric ATCase and DHOase bands gradually decreased leading to a large band around 100 kDa possibly a mixture consisting of ATCase trimer and DHOase dimer (Fig. 21C). No complex formation was observed due to the absence of higher molecular weight species on the cross-linking gel. Under the assumption that ATCase and DHOase form a very transient complex unable to detect, we assessed the ATCase activity in the presence and absence of DHOase. However, there was no change in the activity of ATCase in the presence of DHOase suggesting that ATCase and DHOase do not interact (Fig. 21D & E).

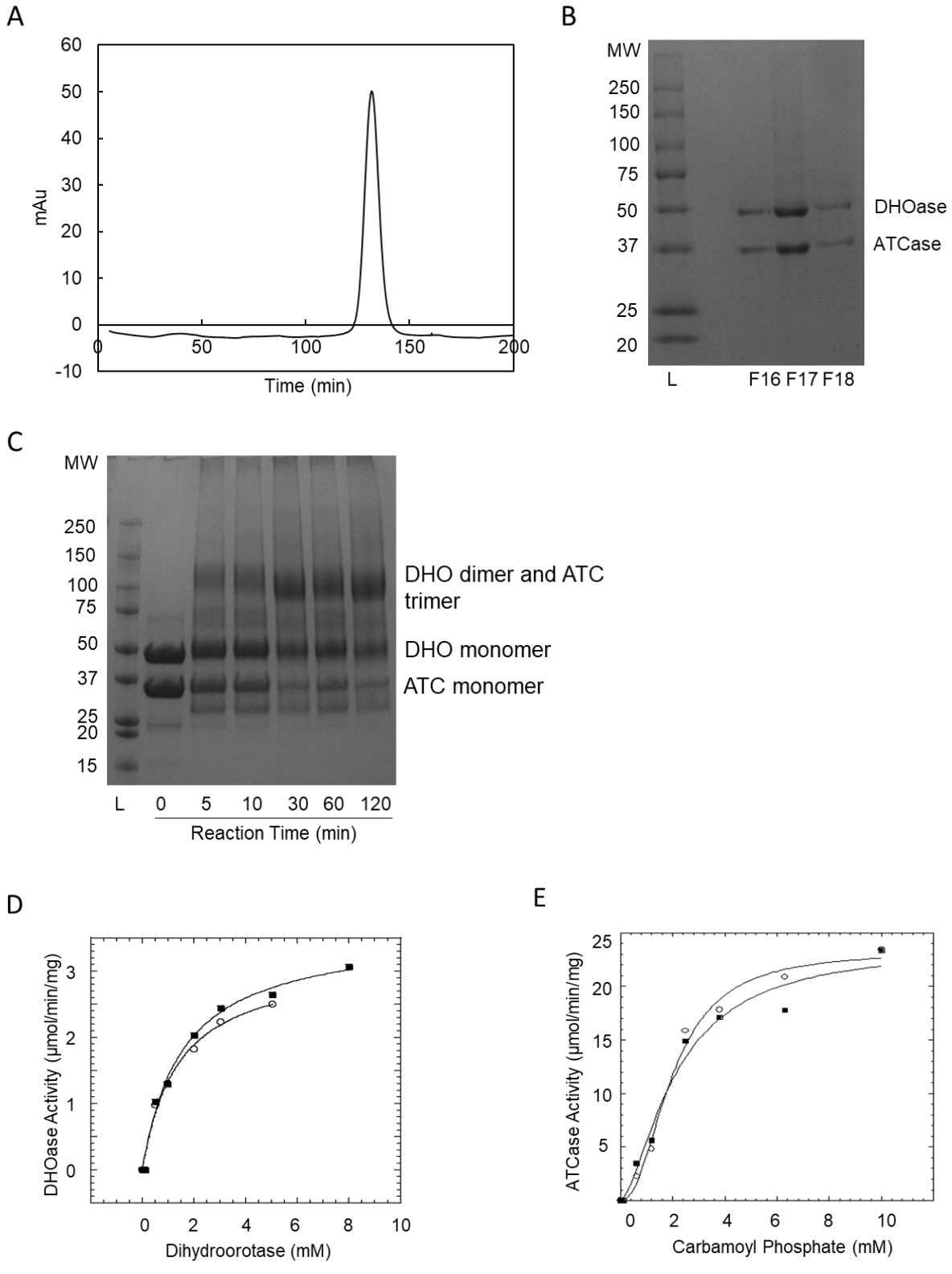

Figure 21: Association of *S. aureus* ATCase with DHOase

A) Purified *S. aureus* ATCase and DHOase were mixed in an equimolar ratio and subjected to size-exclusion chromatography on a Superdex S200 Akta column and B) fractions 16, 17, and 18 corresponding to the peak were analyzed by 12% SDS-PAGE. C) Recombinant ATCase (45 μM) and DHOase (45 μM) were cross-linked for the indicated times with 5 mM bis(sulfosuccinimidyl)suberate. The cross-linked species were analyzed on 12% SDS-PAGE. D) DHOase activity was measured in the (■) presence and (○) absence of ATCase, E) ATCase activity was measured in the (■) presence and (○) absence of DHOase.

Table 10: Kinetics of ATCase and DHOase Association

Variable Substrate	Dihydroorotate Without ATCase	Dihydroorotate With ATCase	Carbamoyl Aspartate Without DHOase	Carbamoyl Aspartate With DHOase
K_m (mM)	1.36	1.55	0.99	1
V_{max} (μmol/min/mg)	3.2	3.5	23.27	23.79
Hill coefficient	-	-	0.99	1

4.4.6 Structure Analysis

The overall topology of the *S. aureus* ATCase-PALA is like the c_3 units of *B. subtilis* and *E. coli*. ATCase has an equilateral triangular appearance with three-bladed propeller, mushroom-shaped cap facing the top face, a stalk-like central cavity, and active sites at the bottom face (Fig. 22A & B). PALA liganded ATCase crystal type belong to space group $P3_221$ with unit cell parameters a = b = 113.33, c = 151.33 Å.

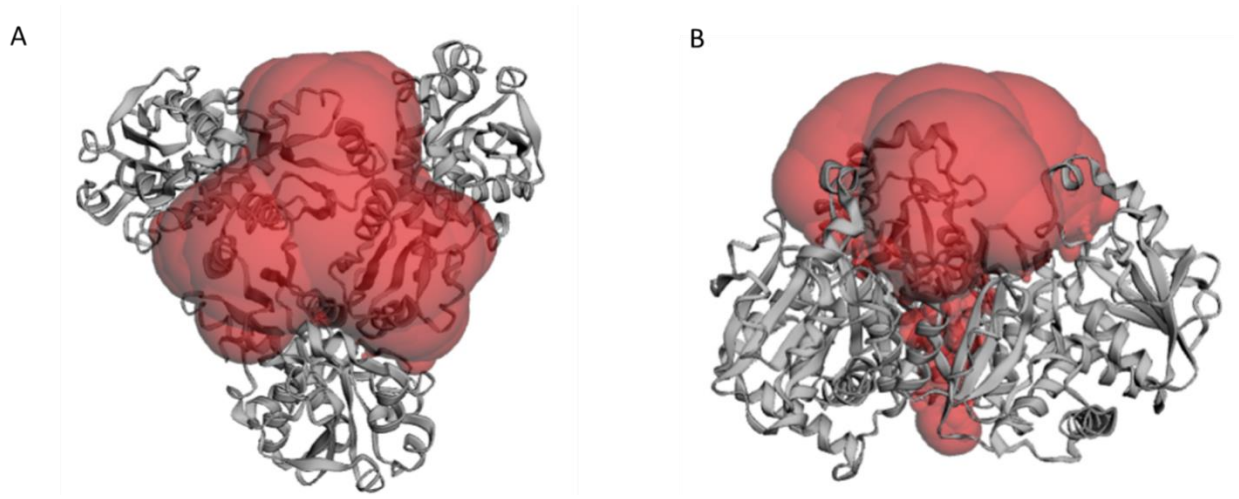

Figure 22: General Schematic of ATCase Structure
Perpendicular views of ATCase with A) top face of ATCase, B) stalk-like central cavity and active sites at the bottom face.

The structure of saATCase-PALA crystals at 2.27 Å resolution has been refined to a final R_{work} of 21% and R_{free} of 23%. The crystal structure contains one trimer in the asymmetric unit, where a molecule of PALA was observed in the active site of every subunit (Fig. 23A). The RMSD between Cα atoms for 293 residues between chains A:B is 0.10 Å, chains A:C is 0.12 Å, and chains B:C is 0.11 Å. The volume of the ATCase active site was calculated using CASTp [138]. Because *B. subtilis* ATCase shares 56% sequence identity with saATCase, the unliganded *B. subtilis* structure (PDB: 3R7D) [26] was used to study conformational changes in saATCase upon ligand binding. The volume of the unliganded *B. subtilis* active site pocket is 570 $Å^3$, which is reduced significantly upon PALA binding, to 64 $Å^3$ in saATCAse as well as in *B. subtilis* (PDB: 3R7L) [26] and Human ATCase (PDB: 5G1N) [139]. PALA has numerous interactions in the active site of ATCase (Fig. 23B-D), like those described in ecATCase [140], explaining the nanomolar affinity of this bisubstrate analog. The phosphonate group of PALA interacts with the CP domain, especially with the side chains of Ser 48 and Arg 100 as well as Ser 75 and Lys 78 from the adjacent subunit. The α- and β-carboxylates of PALA interact with

the side chains of Arg 160, Arg 210, and Gln 212 from the Asp domain. The amine group of PALA interacts with the backbone carbonyl of Ala 253 to possibly increase the nucleophilicity of the amino group of Asp when in close proximity to CP. Moreover, binding of PALA induces significant conformational changes around the active site of ATCase. When compared to *B. subtilis* unliganded ATCase, saATCase-PALA has considerable conformational changes rearranging the 40's loop (43-50), 70's loop (66-82), 100's loop (100-105), and 120's loop (122-126) in the CP domain and 160's loop (158-168), 180's loop (183-192), and 220's loop (211-225) in the Asp domain, essentially bringing them closer to the active site (Fig. 23E). The most crucial conformation changes involve the displacement of 70's loop by 1.4 Å and 220's loop by 12.6 Å resulting in substantial closure of the hinge between CP and Asp domains by 10.6° (Fig. 23F). Superimposition of *B. subtilis* unliganded ATCase and saATCase-PALA gave an RMSD of 1.82 Å for 288 Cα atoms (Fig. 23G).

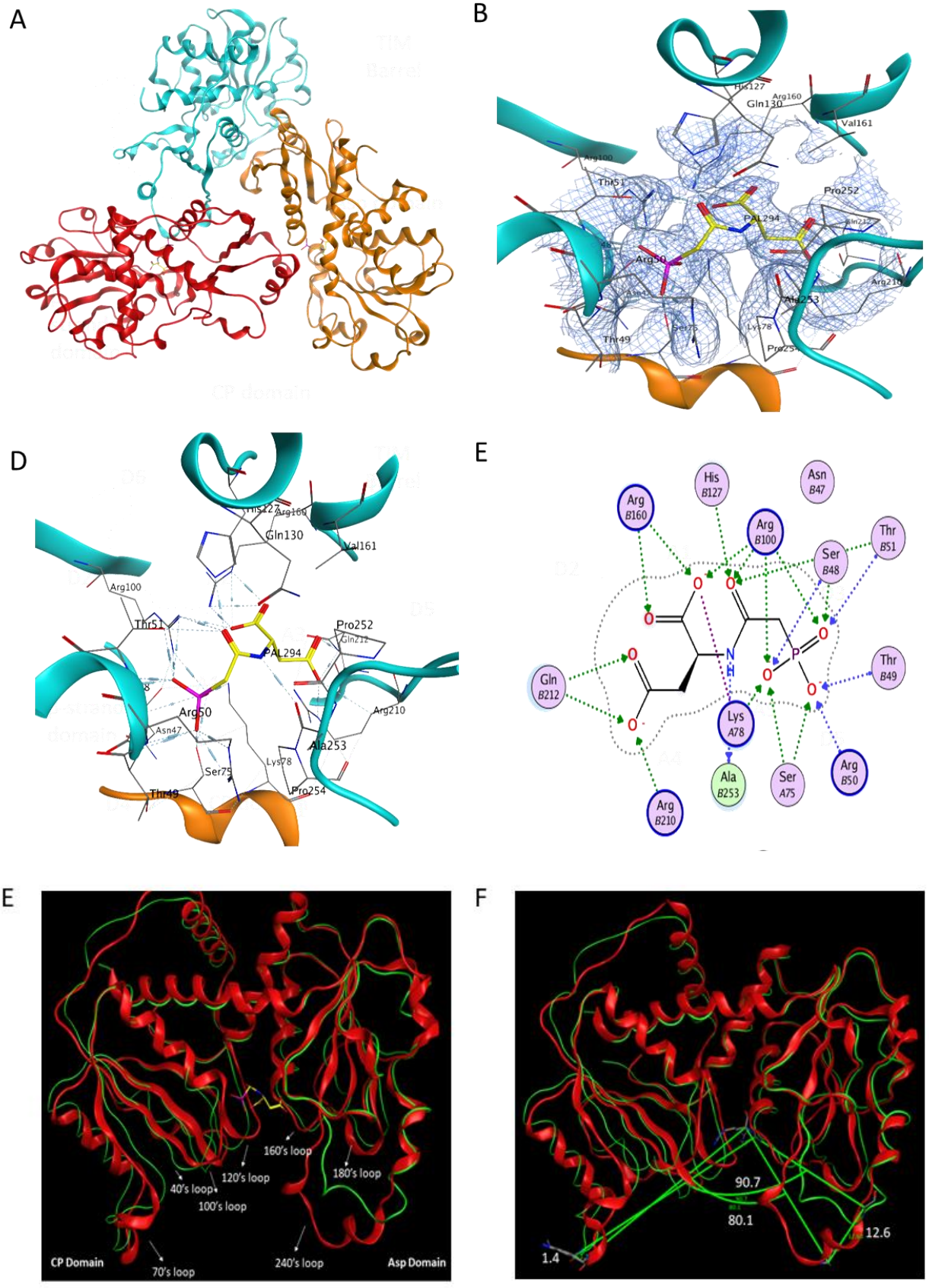
A
B
His127
Arg160
Gln130
Val161
Arg100
Thr51
Pro252
PAL294
Arg50
Arg210
Ala253
Lys78
Thr49
Ser75
D
His127
Arg160
Gln130
Val161
Arg100
Thr51
Pro252
PAL294
Arg50
Asn47
Arg210
Ala253
Lys78
Ser75
Thr49
Pro254
E
His B127
Asn B47
Arg B160
Arg B100
Ser B48
Thr B51
Gln B212
Thr B49
Lys A78
Ala B253
Ser A75
Arg B50
Arg B210
E
160's loop
120's loop
180's loop
40's loop
100's loop
CP Domain
70's loop
240's loop
Asp Domain
F
90.7
80.1
12.6
1.4

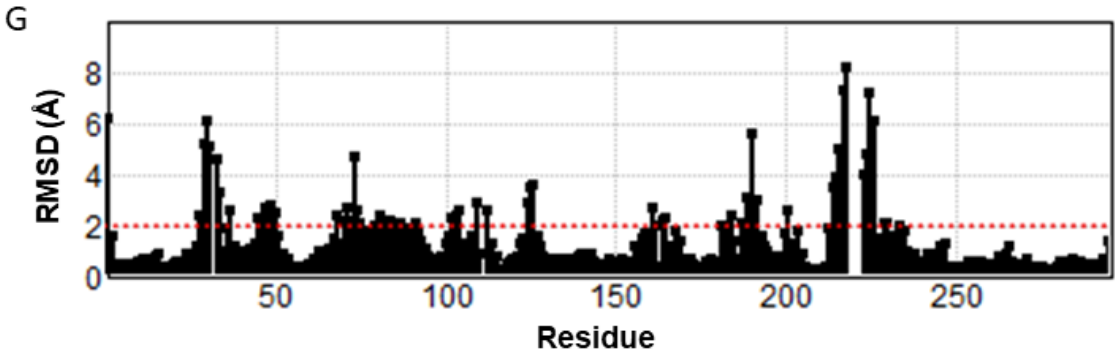

Figure 23: *S. aureus* ATCase Crystal Structure
A) Ribbon representation of the ATCase-PALA trimer in the asymmetric unit. Each chain is shown in a different color. PALA is shown in yellow. B) 2mFo-DFc electron density map (contour level 1σ) within 4.5 Å of PALA atoms. C) Interactions of PALA in the active site. 70's loop of adjacent chain is shown in orange. D) Ligand interaction map for PALA in the active site. E) Superimposition of unliganded *B. subtilis* (green) and saATCase-PALA (red). F) Loop displacement and domain closure of saATCase-PALA (red) compared to unliganded *B. subtilis* (green). G) RMSD plot depicting differences in Cα positions of 288 residues between *B. subtilis* unliganded ATCase and saATCase-PALA.

4.4.7 Effect of TEW on *S. aureus* ATCase Activity

Due to the inhibitory effect of TEW on *P. aeruginosa* ATCase, *S. aureus* ATCase assay was performed to assess the effect of TEW on *S. aureus* ATCase activity. TEW inhibited S. aureus ATCase to a lesser extent than *P. aeruginosa* ATCase with an IC_{50} value of 148 μM (Fig. 24).

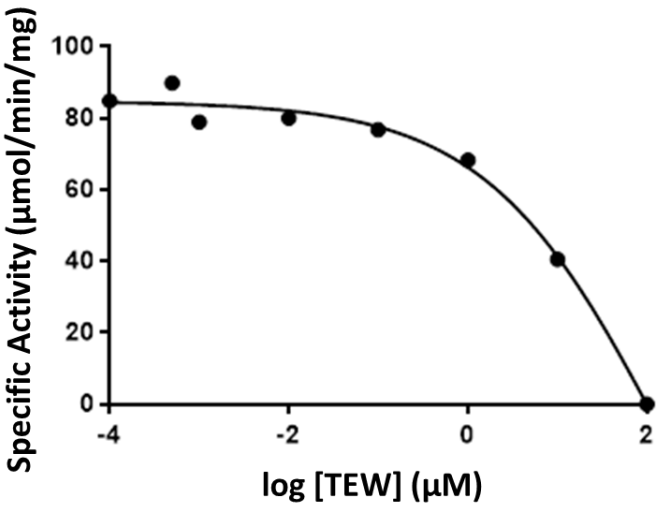

Figure 24: IC_{50} of TEW against *S. aureus* ATCase

S. aureus ATCase assay was performed with 2.5 mM carbamoyl phosphate, 2 mM aspartate, and increasing concentrations of TEW.

4.5 Conclusion

S. aureus ATCase is a 99 kDa trimer composed of three catalytic chains. *S. aureus* ATCase functions independently of DHOase and no evidence of association was observed by size-exclusion chromatography, chemical cross-linking, or enzymatic assay. Unlike *B. subtilis*, *S. aureus* ATCase has been shown to be inhibited by ATP and allosterically regulated. The X-ray structure of *S. aureus* ATCase shares 56% sequence identity with *B. subtilis* ATCase and both ATCases have a very similar tertiary structure. *S. aureus* ATCase undergoes a domain closure upon binding to PALA, a bisubstrate analog, to complete the catalytic cycle. TEW, the polyoxometalate, that displaced PALA from the active site of *P. aeruginosa* ATCase and inhibited its activity also has an inhibitory effect on *S. aureus* ATCase.

4.6 Future Directions

At present, the only high-resolution structure for *S. aureus* ATCase has PALA bound in the active site. To fully understand the conformational changes in *S. aureus* ATCase upon PALA binding, we need to obtain high-quality diffracting crystals of unliganded *S. aureus* ATCase. We are using the closed conformation structure of *S. aureus* ATCase for virtual screening of potential inhibitors. The structure of unliganded *S. aureus* ATCase will also aid in virtual screening of compounds.

Experiments to be performed:

- Kinetic study to determine whether ATP is a competitive or non-competitive inhibitor

- Determine which pyrimidine and purine tri-, di-, and mono-nucleotides inhibit the enzyme
- Crystallization of apo *S. aureus* ATCase
- Co-crystallization of *S. aureus* ATCase with CP to determine intermediate conformation changes prior to Asp binding
- Co-crystallization of *S. aureus* ATCase with ATP to determine ATP binding site
- Co-crystallization of S. aureus ATC with TEW

Chapter 5: *Staphylococcus aureus* Aspartate Transcarbamoylase Structure-Based Drug Design against Bacteremia and Sepsis

5.1 Bacteremia and Sepsis

Bacteremia is the presence of bacteria in the bloodstream and is associated with increased morbidity and mortality worldwide. Bacteremia can result from a breach of integrity of the skin, immune system, or from direct penetration in the bloodstream. It can result from existing local infection, dental procedure, surgical treatment of the infected wound, colonization of indwelling catheters or prosthetic joints, or from vigorous toothbrushing [141, 142]. *S. aureus* is a major cause of bacteremia and is one of the most frequently isolated pathogens in hospital-acquired and community-acquired bloodstream infections. *S. aureus* bacteremia poses a greater burden on the healthcare system compared with bacteremia caused by any other pathogen [143]. *S. aureus* bacteremia is associated with a longer duration of hospital stay, higher treatment cost, and a higher mortality rate [144]. Patients with advanced age, a compromised immune system, comorbidities, and intravenous drug use are at a higher risk of *S. aureus* bacteremia [145]. Bacteremia may be transient and cleared by the host immune system with no major adverse consequences, but it may also lead to sepsis and death. Sepsis is characterized by dysregulated host response and systemic inflammation to infection resulting in organ dysfunction [146]. Sepsis presents with fever, tachycardia, tachypnea with normal blood pressure. As sepsis develops into septic shock, it presents with decreased alertness and hypotension [147, 148]. Organ dysfunction is identified by the quick SOFA score (sequential organ failure assessment score): respiratory rate ≥ 22/min, altered mentation, and systolic blood pressure ≤ 100 mm Hg, where all three criteria must be present. The mortality rate increases with multiple organ failure.

5.2 Current Therapeutics for Sepsis and Septic Shock

Broad-spectrum gram-positive and gram-negative combinatorial antibiotics are administered intravenously as soon as possible and then therapy is narrowed after pathogen identification and sensitivities. The source of infection is controlled by removing potentially infected indwelling devices, drainage of an abscess, and debridement of infected necrotic tissue. Furthermore, perfusion is restored with IV fluids and vasopressors, and oxygen support is provided through mechanical ventilation [147, 149, 150].

5.3 Aspartate Transcarbamoylase as a Potential Therapeutic Target

Efficient utilization of available nutrients is a key for survival and pathogenesis of bacteria in a host environment. Although host environments are nutrient rich, many nutrients essential to bacterial growth are sequestered by the host, a term called nutritional immunity [151]. Studies by Simmonds and Harkness [152] determined the approximate level of uridine in human plasma to be 3 μmol/L. The bacteria can salvage low levels of pyrimidines but eventually the bacteria must overcome the pyrimidine-limited environment by upregulating the *de novo* pyrimidine biosynthesis pathway. A study by Samant et al. [153], showed that the *de novo* nucleotide biosynthesis is very critical for bacterial growth in human serum. This study demonstrated that inactivation of purine or pyrimidine biosynthetic genes in *E. coli*, *Salmonella enterica*, or *B. anthracis* led to severe growth defects of the mutants compared to the wildtype. Another study by Connolly et al. [154], demonstrated that a defect in tetrahydrofolate synthesis led to significant growth inhibition of *S. aureus* on human blood agar. This growth inhibition could only be rescued

by the addition of thymidine suggesting that thymidine content in blood is not enough for salvage and that pyrimidines are critical in bacterial survival.

ATCase catalyzes the committed step in the *de novo* pyrimidine biosynthesis pathway in bacteria, is allosterically regulated by nucleotide triphosphates, and therefore is an attractive drug target in pyrimidine biosynthesis. The active site of ATCase composed of residues from adjacent monomers in a trimer is highly conserved in all organisms. Therefore, our interest lies in the recognition and development of allosteric inhibitors that bind away from the active site and inhibit ATCase activity.

5.4 Virtual Screening of Compounds against *S. aureus* Aspartate Transcarbamoylase

5.4.1 Test: Docking of PALA into the Active Site of *S. aureus* ATCase

The *S. aureus* ATCase-PALA structure was loaded into MOE [118] without PALA bound in the active site. To fix structural issues, the protein was prepared using the QuickPrep function. QuickPrep is an automated process for the correction, protonation, and minimization of the structure. QuickPrep prepares structures by recognizing residues with atoms having fractional occupancies and using the highest occupancy alternate by default and by adding chemically appropriate hydrogen atoms. QuickPrep uses Protonate3D for protonation and optimization of the orientation of the hydrogen atoms, deletes water molecules farther than 4.5 Å from the protein, tethers atoms so the atoms do not deviate too far from their initial positions, and energy minimizes the structure to an RMS (Root Mean Square) gradient of 0.1 kcal/mol/A using Amber10:EHT forcefield unless specified otherwise. PALA, saved as .mol2, was loaded into MOE, and the molecule was washed. The Molecule Wash panel in MOE corrects for connected

components to molecule and protonation states and scales bond lengths to 1.5 Å for distorted structures. For PALA, the dominant protonation state at pH 7.0 was applied. PALA was successfully docked in the active site of *S. aureus* ATCase using the default settings in the General Dock panel. The placement was carried out using Triangle Matcher and scored using London dG. Triangle Matcher generates poses by aligning ligand triplets of atoms on triplets of alpha spheres [118]. The refinement was carried out using Rigid Receptor and scored using GBVI/WSA dG. Rigid receptor option keeps backbone and sidechain atoms of the receptor fixed.

5.4.2 Docking of FDA-Approved Compounds

Potential binding sites in *S. aureus* ATCase were identified using the Site Finder [118] application in MOE. Site Finder identifies regions of tight atomic packing and calculates alpha spheres on these regions. Alpha spheres are calculated by triangulation of three-dimensional points and assigning a sphere for each resulting simplex or a collection of four points. These alpha spheres are clustered to produce a collection of sites. It then ranks the sites according to propensity for ligand binding (PLB) score based on the amino acid composition in the site. When Site Finder was run on *S. aureus* ATCase, the two sites chosen for virtual screening were at the trimer interface and the interdomain cleft. The trimer interface was the highest-ranked site with a PLB score of 3.41, whereas the interdomain cleft had a PLB score of -0.18. The rationale for targeting the trimer interface was that the small molecule would disrupt trimer formation which would then lead to inhibition of ATCase activity, whereas targeting the cleft would interfere with the domain closure that is essential to the catalytic cycle of ATCase.

The FDA-approved compound library was obtained from the Zinc database [155]. The compounds were washed and the dominant protonation state at pH 7.0 was applied. The compounds were docked at the trimer interface or at the interdomain cleft using the default settings as described previously for PALA docking. The compounds with an S score of -8 kcal/mol or lower were considered for further analysis.

5.4.3 Assessment of Top-Ranking FDA-Approved Compounds

The top three compounds with the lowest S score from docking of FDA-approved compounds at the interdomain cleft compounds were pentoxifylline, ropinirole HCl, and nitazoxanide. The binding poses of all the three compounds are shown in Fig. 25.

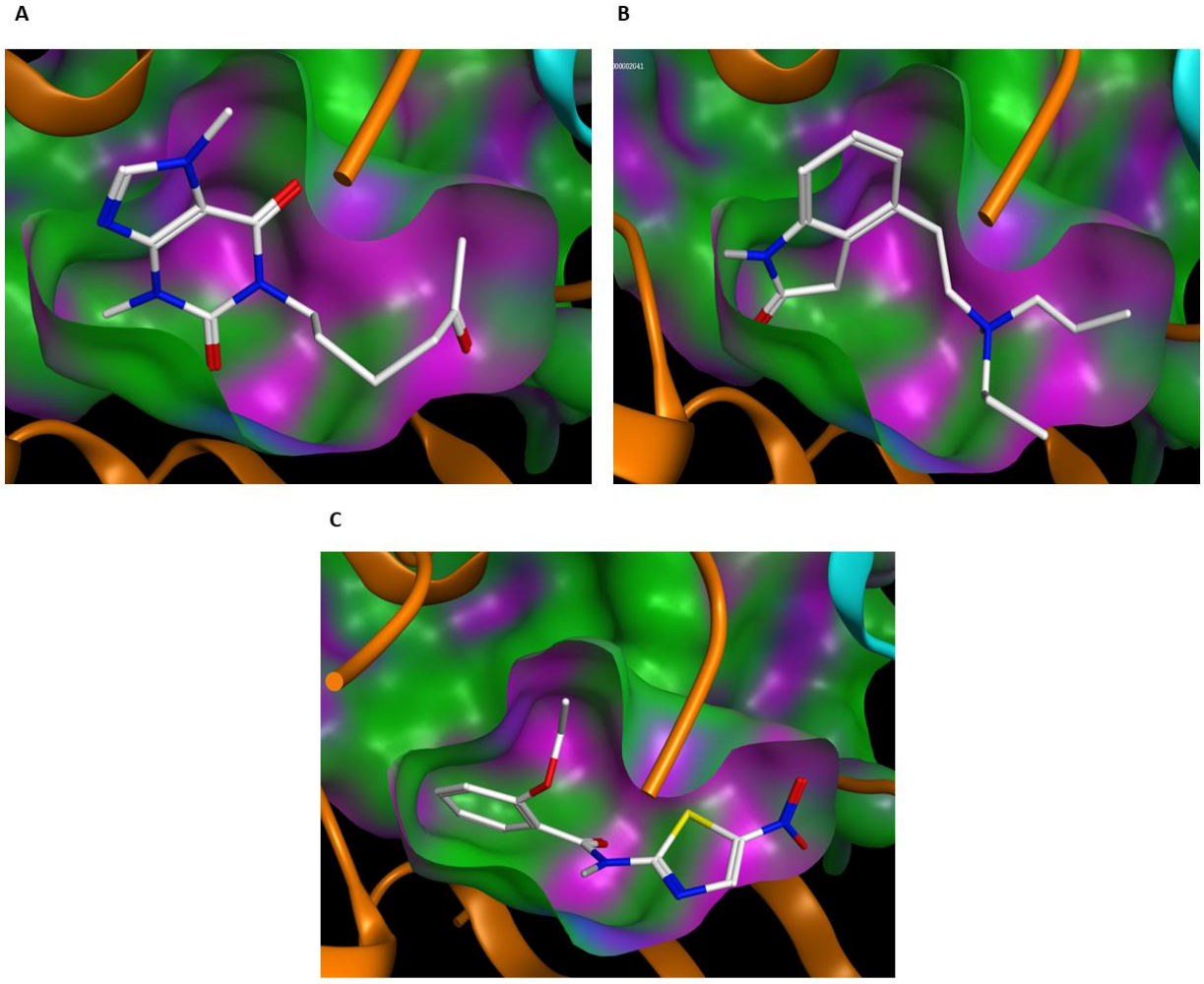

Figure 25: Binding Poses of Top-Ranking FDA-Approved Compounds in the Interdomain Cleft of *S. aureus* ATCase

The binding poses from docking of A) pentoxifylline, B) ropinirole HCl, and C) nitazoxanide. The color scheme for the molecular surface is as follows: purple for hydrogen bonding, green for hydrophobic, and blue for mildly polar.

The interdomain cleft is comprised of chain A Glu 46, Asn 47, Arg 160, Glu 214, Arg 215 and chain C Ser 77 and Lys 78. All the residues except for Glu 46 are also a part of the active site. Since the active site is conserved in all ATCases, the FDA-approved compounds were docked in the active site of human ATCase (PDB: 5G1N) [139] and were compared against *S. aureus* ATCase interdomain cleft.

Pentoxifylline is the top scoring compound with a docking score of -8.99 kcal/mol. Pentoxifylline interacts with the *S. aureus* cleft residues Arg 100, Lys 78, and Arg 160 through hydrogen bonding and Arg 210 and Lys 78 through pi-cation interaction (Fig. 26A). Arg 100 in *S. aureus* cleft is corresponding to Arg 2085 in the human active site of ATCase, and this Arg 2085 in human active site also interacts with pentoxifylline through hydrogen bonding as in *S. aureus* cleft (Fig. 26B).

Ropinirole HCl has a docking score of -8.56 kcal/mol in the S. aureus cleft and has a few interactions with the receptor. Ropinirole interacts with Ser 159, Val 161, and Ala 253 through hydrogen bonding and with Arg 210 though pi-cation interaction (Fig. 26C). In human active site, ropinirole binding is much weaker with a docking score of -5.6 kcal/ml and it has only one hydrogen bond with the receptor (Fig. 26D).

Nitazoxanide has a docking score of -8.54 kcal/mol in the *S. aureus* cleft as compared to -5.99 kcal/mol in the human active site of ATCase. It has several hydrogen bond interactions with Ser 75, Arg 210, Gln 212, Arg 160, Thr 51, Arg 100, and Thr 49 in the *S. aureus* cleft (Fig. 26E). None of these residues correspond to the residues in human active site interacting with nitazoxanide (Fig. 26F).

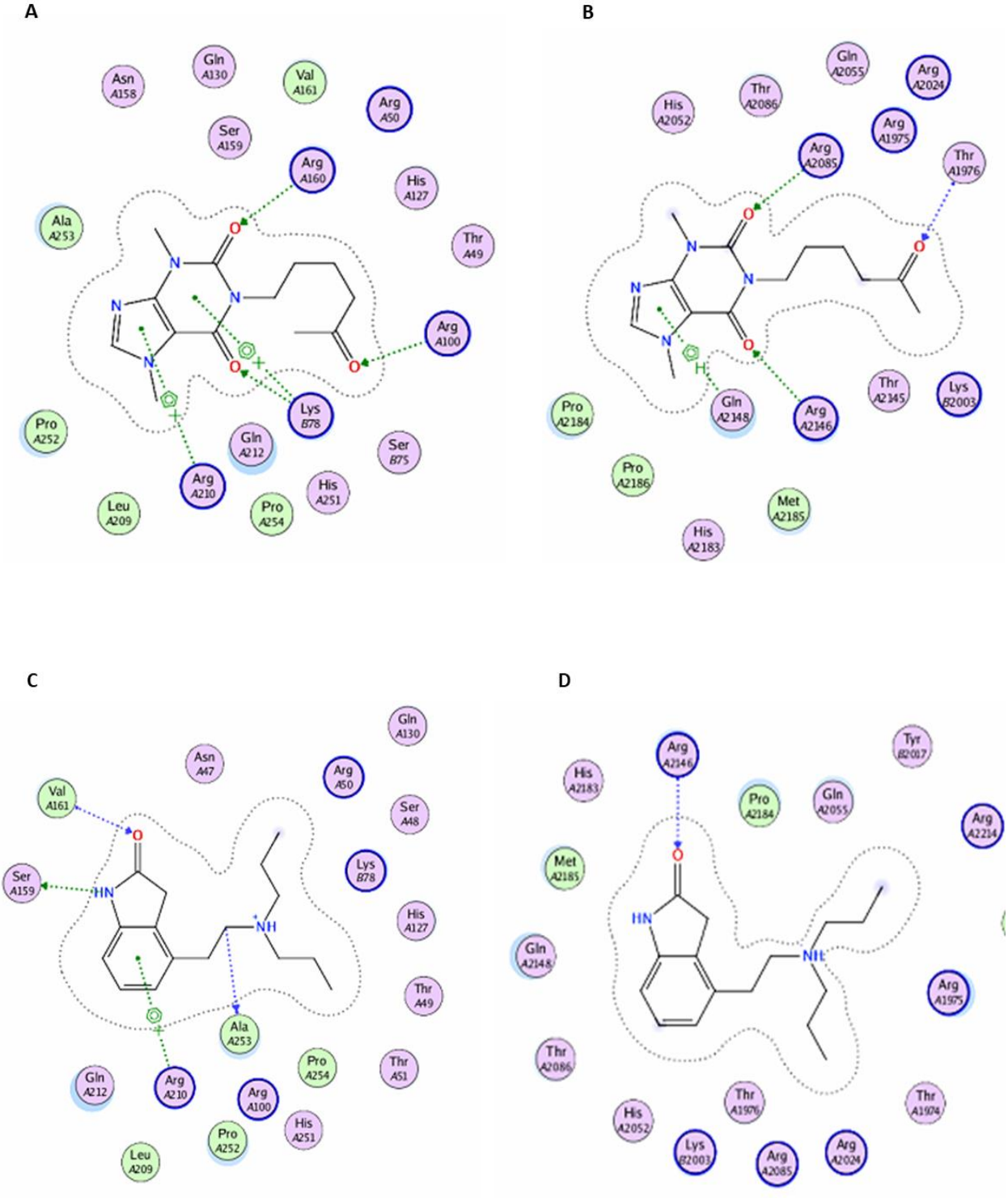
A
Gln A130
Asn A158
Val A161
Arg A50
Ser A159
Arg A160
His A127
Ala A253
Thr A49
Arg A100
Lys B78
Pro A252
Gln A212
Ser B75
Arg A210
His A251
Leu A209
Pro A254
B
Gln A2055
Arg A2024
Thr A2086
His A2052
Arg A1975
Arg A2085
Thr A1976
Thr A2345
Lys B2003
Pro A2184
Gln A2148
Arg A2146
Pro A2186
Met A2185
His A2183
C
Gln A130
Asn A47
Arg A50
Val A161
Ser A48
Ser A159
Lys B78
His A127
Thr A49
Ala A253
Pro A254
Thr A51
Gln A212
Arg A210
Arg A100
His A251
Pro A252
Leu A209
D
Tyr B2017
Arg A2146
His A2183
Pro A2184
Gln A2055
Arg A2214
Met A2185
Gln A2148
Arg A1975
Thr A2086
Thr A1976
Thr A1974
His A2052
Lys B2003
Arg A2085
Arg A2024

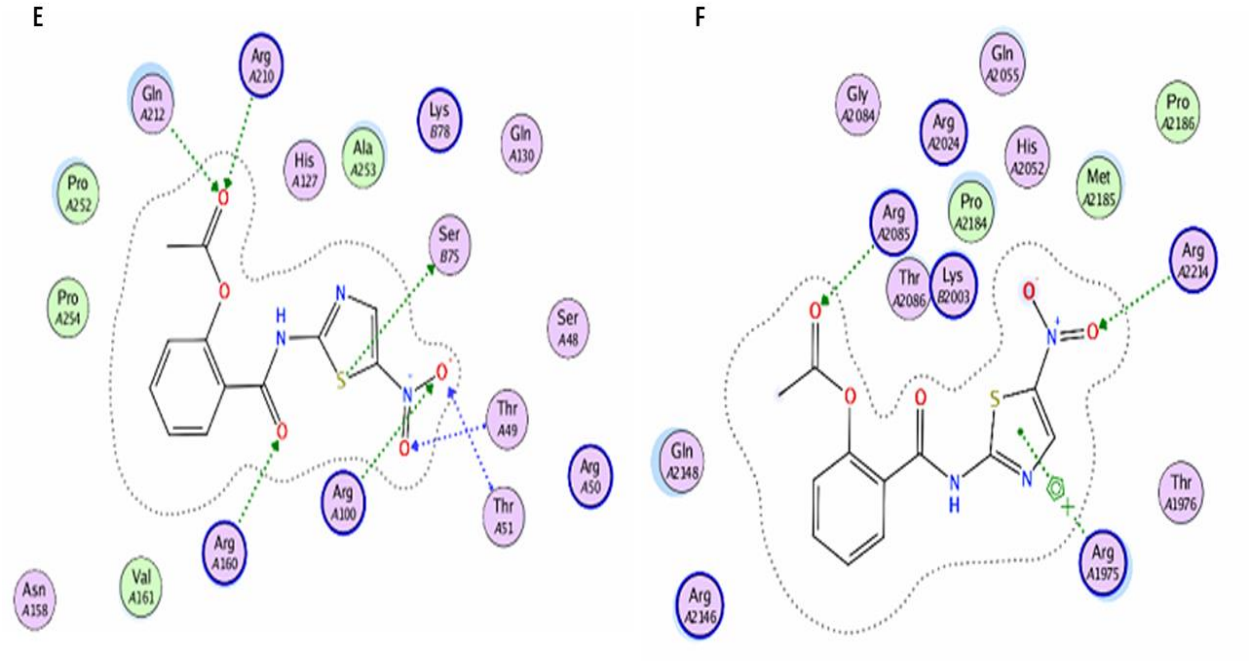

Figure 26: Ligand Interaction Maps
The top-ranking FDA-approved compounds were docked in the interdomain cleft of *S. aureus* and the active site of human ATCase and the ligand interactions were compared, pentoxifylline in A) *S. aureus* interdomain cleft, B) active site of human ATCase; Ropinirole HCl in C) *S. aureus* interdomain cleft, D) active site of human ATCase; nitazoxanide in E) *S. aureus* interdomain cleft, and F) active site of human ATCase

ATCase assays were performed to assess the effect of these compounds on *S. aureus* ATCase activity. Pentoxifylline gave a 14% decrease in ATCase activity but the inhibition was not dose-dependent. Nitazoxanide did not show any inhibition. Ropinirole HCl gave an IC_{50} of 3.12 mM, however, it is not accurate as 3.12 mM is the highest concentration used in the assay (Fig. 27).

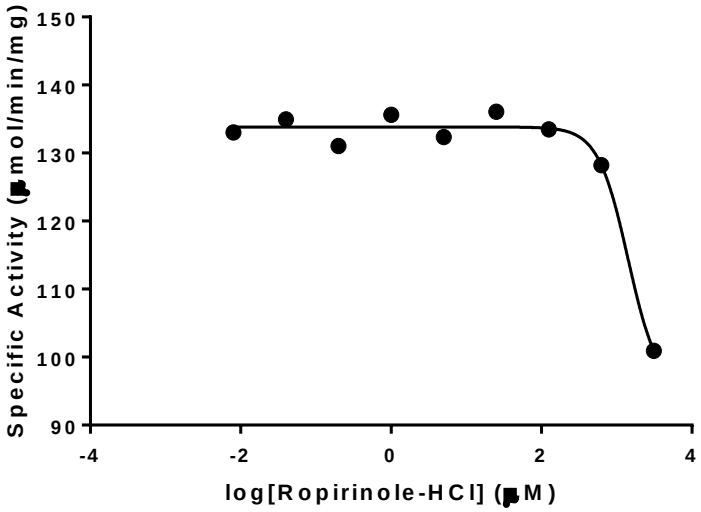

Figure 27: IC_{50} of Ropinirole HCl against *S. aureus* ATCase
S. aureus ATCase assay was performed with 2.5 mM carbamoyl phosphate, 2 mM aspartate, and increasing concentrations of ropinirole HCl.

Most compounds with an S score of -8 kcal/mol or less from the trimer interface were highly solvent exposed. Only one compound, indocyanine green, was considered to study its effect on *S. aureus* ATCase activity. When assessed for ATCase activity, the tubes containing indocyanine green turned deep yellow during the intermediate steps of the assay, and it could not be analyzed further due to intrinsic interference of the compound with the final step of the assay.

Furthermore, *S. aureus* ATCase was subjected to thermal shift assay in the absence and presence of the top-scoring compounds to determine if any of the compounds bind to the protein. The final concentrations of ATCase and the SYPRO Orange were optimized to 0.1 mg/mL and 20X, respectively. Three concentrations of pentoxifylline, ropinirole HCl, nitazoxanide, and indocyanine green, were tested: 1 mM, 0.1 mM, and 0.01 mM. Of all four compounds tested, only nitazoxanide showed a shift in the melting temperature of *S. aureus* ATCase. Nitazoxanide led to a dose-dependent

negative shift in the melting temperature of ATCase, with 1 °C shift at 0.01 mM, 2 °C shift at 0.1 mM, and 5 °C shift at 1 mM (Fig. 28).

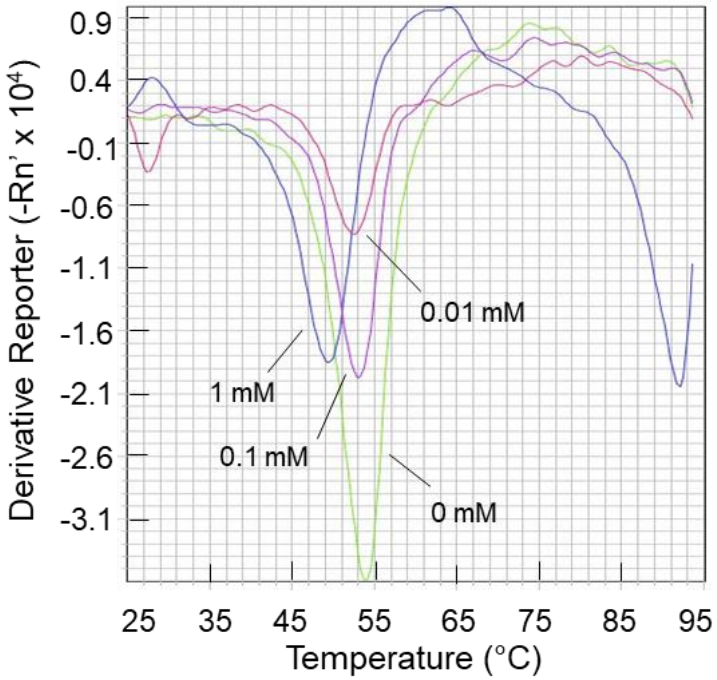

Figure 28: Effect of Nitazoxanide on the Thermal Stability of *S. aureus* ATCase
The thermal stability of S. aureus ATCase was measured nitazoxanide. The melting temperature of ATCase is 54 °C in the absence of nitazoxanide (green), 53 °C with 0.01 mM nitazoxanide (pink), 52 °C with 0.1 mM nitazoxanide (purple), and 49 °C with 1 mM nitazoxanide (blue).

5.5 Conclusion

Although the *S. aureus* interdomain cleft overlaps with the active site, the top-ranking FDA-approved compounds have differential docking in the *S. aureus* cleft compared to the active site of human ATCase. None of the top-scoring compounds had substantial inhibitory activity against *S. aureus* ATCase in vitro. Of all the compounds tested, only nitazoxanide had a dose-dependent effect on the melting temperature of *S. aureus* ATCase suggesting that although it binds *S. aureus* ATCase in vitro, the binding is probably too weak to see its inhibitory effect at the concentrations tested.

5.6 Future Directions

We have screened a very small subset from the extraordinarily large database of compounds available. To discover promising inhibitors, we will have to screen many more compounds. In terms of the few FDA-approved compounds explored in the lab, the MedChem Transformations [118] operation was applied to discover novel chemical structures from nitazoxanide because only nitazoxanide showed binding in thermal shift analysis. MedChem Transformations applies various transformation rules to exchange functional groups or alter the ring while preserving the rest of the ligand. The two chemical structures as a result of transformation on nitazoxanide are shown in Fig. 29. It would be worthwhile to determine how these newly transformed compounds dock in the cleft compared to the parent compound, nitazoxanide, and how these compounds behave in assay against ATCase activity. It would also be worthwhile to co-crystallize ropinirole HCl with *S. aureus* ATCase due to its negligible effect on ATCase activity. If ropinirole HCl binds in the cleft as predicted by the docking program, this compound can then also be used as a starting point in designing more potent inhibitors.

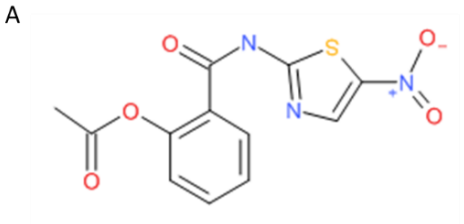

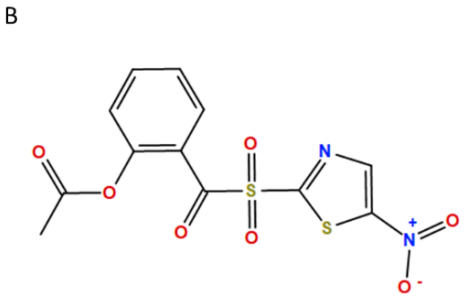

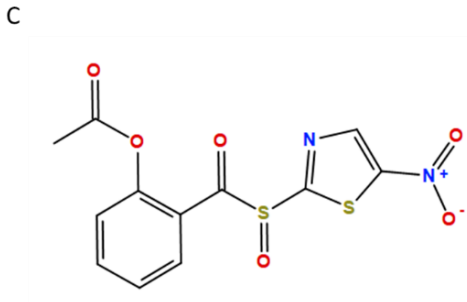

Figure 29: MedChem Transformations on Nitazoxanide
Compounds generated by MedChem transformation operation in MOE, A) nitazoxanide, B and C) Novel structures generated by MedChem transformations on nitazoxanide.

REFERENCES

1. Löffler, M., et al., *Pyrimidine pathways in health and disease.* Trends in Molecular Medicine, 2005. **11**(9): p. 430-437.
2. Evans, D.R. and H.I. Guy, *Mammalian Pyrimidine Biosynthesis: Fresh Insights into an Ancient Pathway.* Journal of Biological Chemistry, 2004. **279**(32): p. 33035-33038.
3. Moffatt, B.A. and H. Ashihara, *Purine and pyrimidine nucleotide synthesis and metabolism.* The arabidopsis book, 2002. **1**: p. e0018-e0018.
4. Walther, R., et al., *Evidence that a Single Polypeptide Catalyses the Two Step Conversion of Orotate to UMP in Cells from a Tomato Suspension Culture.* J Plant Physiol, 1984. **116**(4): p. 301-11.
5. HUGULEY, C.M., et al., *Refractory Megaloblastic Anemia Associated with Excretion of Orotic Acid.* Blood, 1959. **14**(6): p. 615-634.
6. Nyhan, W.L., *Disorders of purine and pyrimidine metabolism.* Molecular Genetics and Metabolism, 2005. **86**(1): p. 25-33.
7. Jones, M.E., *Pyrimidine nucleotide biosynthesis in animals: genes, enzymes, and regulation of UMP biosynthesis.* Annu Rev Biochem, 1980. **49**: p. 253-79.
8. Freund, J.N. and B.P. Jarry, *The rudimentary gene of Drosophila melanogaster encodes four enzymic functions.* J Mol Biol, 1987. **193**(1): p. 1-13.
9. Faure, M., J.H. Camonis, and M. Jacquet, *Molecular characterization of a Dictyostelium discoideum gene encoding a multifunctional enzyme of the pyrimidine pathway.* Eur J Biochem, 1989. **179**(2): p. 345-58.

10. Denis-Duphil, M., *Pyrimidine biosynthesis in Saccharomyces cerevisiae: the ura2 cluster gene, its multifunctional enzyme product, and other structural or regulatory genes involved in de novo UMP synthesis.* Biochem Cell Biol, 1989. **67**(9): p. 612-31.

11. Makoff, A.J., F.P. Buxton, and A. Radford, *A possible model for the structure of the Neurospora carbamoyl phosphate synthase-aspartate carbamoyl transferase complex enzyme.* Molecular and General Genetics 1978. **161**(3): p. 297-304.

12. Gao, G., et al., *Novel organization and sequences of five genes encoding all six enzymes for de novo pyrimidine biosynthesis in Trypanosoma cruzi.* J Mol Biol, 1999. **285**(1): p. 149-61.

13. Bethell, M.R. and M.E. Jones, *Molecular size and feedback-regulation characteristics of bacterial asartate transcarbamulases.* Arch Biochem Biophys, 1969. **134**(2): p. 352-65.

14. Ahuja, A., et al., *Aquifex aeolicus dihydroorotase: association with aspartate transcarbamoylase switches on catalytic activity.* J Biol Chem, 2004. **279**(51): p. 53136-44.

15. Zhang, P., et al., *Dihydroorotase from the hyperthermophile Aquifex aeolicus is activated by stoichiometric association with aspartate transcarbamoylase and forms a one-pot reactor for pyrimidine biosynthesis.* Biochemistry, 2009. **48**(4): p. 766-78.

16. Van de Casteele, M., et al., *Structure and expression of a pyrimidine gene cluster from the extreme thermophile Thermus strain ZO5.* J Bacteriol, 1997. **179**(11): p. 3470-81.

17. Hughes, L.E., M.Z. Hooshdaran, and G.A. O'Donovan, *Streptomyces Aspartate Transcarbamoylase Is a Dodecamer with Dihydroorotase Activity.* Current Microbiology, 1999. **39**(4): p. 175-179.

18. Purcarea, C., et al., *Aquifex aeolicus Aspartate Transcarbamoylase, an Enzyme Specialized for the Efficient Utilization of Unstable Carbamoyl Phosphate at Elevated Temperature.* Journal of Biological Chemistry, 2003. **278**(52): p. 52924-52934.

19. Bergh, S.T. and D.R. Evans, *Subunit structure of a class A aspartate transcarbamoylase from Pseudomonas fluorescens.* Proc Natl Acad Sci U S A, 1993. **90**(21): p. 9818-22.

20. Schurr, M.J., et al., *Aspartate transcarbamoylase genes of Pseudomonas putida: requirement for an inactive dihydroorotase for assembly into the dodecameric holoenzyme.* J Bacteriol, 1995. **177**(7): p. 1751-9.

21. Vickrey, J.F., G. Herve, and D.R. Evans, *Pseudomonas aeruginosa aspartate transcarbamoylase. Characterization of its catalytic and regulatory properties.* J Biol Chem, 2002. **277**(27): p. 24490-8.

22. Gerhart, J.C. and H.K. Schachman, *Distinct subunits for the regulation and catalytic activity of aspartate transcarbamylase.* Biochemistry, 1965. **4**(6): p. 1054-62.

23. Rosenbusch, J.P. and K. Weber, *Subunit structure of aspartate transcarbamylase from Escherichia coli.* J Biol Chem, 1971. **246**(6): p. 1644-57.

24. Kantrowitz, E.R., *Allostery and cooperativity in Escherichia coli aspartate transcarbamoylase.* Arch Biochem Biophys, 2012. **519**(2): p. 81-90.

25. Brabson, J.S. and R.L. Switzer, *Purification and properties of Bacillus subtilis aspartate transcarbamylase.* J Biol Chem, 1975. **250**(22): p. 8664-9.

26. Harris, K.M., et al., *Crystallographic snapshots of the complete catalytic cycle of the unregulated aspartate transcarbamoylase from Bacillus subtilis.* J Mol Biol, 2011. **411**(1): p. 190-200.

27. Stevens, R.C., K.M. Reinisch, and W.N. Lipscomb, *Molecular structure of Bacillus subtilis aspartate transcarbamoylase at 3.0 A resolution.* Proc Natl Acad Sci U S A, 1991. **88**(14): p. 6087-91.

28. Holm, L. and C. Sander, *An evolutionary treasure: unification of a broad set of amidohydrolases related to urease.* Proteins, 1997. **28**(1): p. 72-82.

29. Porter, T.N., Y. Li, and F.M. Raushel, *Mechanism of the Dihydroorotase Reaction.* Biochemistry, 2004. **43**(51): p. 16285-16292.

30. Fields, C., et al., *Phylogenetic analysis and classification of dihydroorotases: a complex history for a complex enzyme.* Paths Pyrimidines, 1999. **7**: p. 49-63.

31. Martin, P.D., et al., *The Crystal Structure of a Novel, Latent Dihydroorotase from Aquifex aeolicus at 1.7Å Resolution.* Journal of Molecular Biology, 2005. **348**(3): p. 535-547.

32. Grande-García, A., et al., *Structure, Functional Characterization, and Evolution of the Dihydroorotase Domain of Human CAD.* Structure, 2014. **22**(2): p. 185-198.

33. Seibert, C.M. and F.M. Raushel, *Structural and Catalytic Diversity within the Amidohydrolase Superfamily.* Biochemistry, 2005. **44**(17): p. 6383-6391.

34. Mehboob, S., et al., *Structure of dihydroorotase from Bacillus anthracis at 2.6 Å resolution.* Acta crystallographica. Section F, Structural biology and crystallization communications, 2010. **66**(Pt 11): p. 1432-1435.

35. *The Crystal Structure of a Dihydroorotase from Staphylococcus aureus.* To be published.

36. Vitali, J., A.K. Singh, and M.J. Colaneri, *Characterization of the Dihydroorotase from Methanococcus jannaschii.* Protein J, 2017. **36**(4): p. 361-373.

37. Lee, M., et al., *Dihydroorotase from Escherichia coli: Loop Movement and Cooperativity between Subunits.* Journal of Molecular Biology, 2005. **348**(3): p. 523-533.

38. Lee, M., et al., *Kinetic and structural analysis of mutant Escherichia coli dihydroorotases: a flexible loop stabilizes the transition state.* Biochemistry, 2007. **46**(37): p. 10538-50.

39. Evans, H.G., et al., *Intersubunit communication in the dihydroorotase-aspartate transcarbamoylase complex of Aquifex aeolicus.* Protein science : a publication of the Protein Society, 2014. **23**(1): p. 100-109.

40. Silby, M.W., et al., *Pseudomonas genomes: diverse and adaptable.* FEMS Microbiology Reviews, 2011. **35**(4): p. 652-680.

41. Vasil, M.L., *Pseudomonas aeruginosa: biology, mechanisms of virulence, epidemiology.* J Pediatr, 1986. **108**(5 Pt 2): p. 800-5.

42. Iglewski, B.H., *Pseudomonas*, in *Medical Microbiology*, B. S, Editor. 1996, University of Texas Medical Branch at Galveston: Galveston (TX).

43. Gilardi, G.L., *Characterization of Pseudomonas species isolated from clinical specimens.* Applied microbiology, 1971. **21**(3): p. 414-419.

44. Tsuji, A., et al., *The effects of temperature and pH on the growth of eight enteric and nine glucose non-fermenting species of gram-negative rods.* Microbiol Immunol, 1982. **26**(1): p. 15-24.

45. Cox, C.D., *Role of pyocyanin in the acquisition of iron from transferrin.* Infection and immunity, 1986. **52**(1): p. 263-270.

46. Pitt, T.L., *Biology of Pseudomonas aeruginosa in relation to pulmonary infection in cystic fibrosis.* Journal of the Royal Society of Medicine, 1986. **79 Suppl 12**(Suppl 12): p. 13-18.

47. Lutz, J.K. and J. Lee, *Prevalence and antimicrobial-resistance of Pseudomonas aeruginosa in swimming pools and hot tubs.* International journal of environmental research and public health, 2011. **8**(2): p. 554-564.

48. Shepp, D.H., et al., *Serious Pseudomonas aeruginosa infection in AIDS.* J Acquir Immune Defic Syndr, 1994. **7**(8): p. 823-31.

49. Chatzinikolaou, I., et al., *Recent experience with Pseudomonas aeruginosa bacteremia in patients with cancer: Retrospective analysis of 245 episodes.* Arch Intern Med, 2000. **160**(4): p. 501-9.

50. Zeglen, S., et al., *Frequency of Pseudomonas aeruginosa colonizations/infections in lung transplant recipients.* Transplant Proc, 2009. **41**(8): p. 3222-4.

51. Kollef, M.H., et al., *Global prospective epidemiologic and surveillance study of ventilator-associated pneumonia due to Pseudomonas aeruginosa.* Crit Care Med, 2014. **42**(10): p. 2178-87.

52. Santucci, S.G., et al., *Infections in a burn intensive care unit: experience of seven years.* Journal of Hospital Infection, 2003. **53**(1): p. 6-13.

53. Gellatly, S.L. and R.E.W. Hancock, *Pseudomonas aeruginosa : new insights into pathogenesis and host defenses.* Pathogens and Disease, 2013. **67**(3): p. 159-173.

54. Høiby, N. and C. Koch, *Cystic fibrosis. 1. Pseudomonas aeruginosa infection in cystic fibrosis and its management.* Thorax, 1990. **45**(11): p. 881-884.

55. Landsperger, W.J., et al., *Inhibition of bacterial motility with human antiflagellar monoclonal antibodies attenuates Pseudomonas aeruginosa-induced pneumonia in the immunocompetent rat.* Infection and immunity, 1994. **62**(11): p. 4825-4830.

56. Doig, P., et al., *Role of pili in adhesion of Pseudomonas aeruginosa to human respiratory epithelial cells.* Infection and immunity, 1988. **56**(6): p. 1641-1646.

57. Arora, S.K., et al., *Cloning and characterization of Pseudomonas aeruginosa fliF, necessary for flagellar assembly and bacterial adherence to mucin.* Infect Immun, 1996. **64**(6): p. 2130-6.

58. Sadikot, R.T., et al., *Pathogen-host interactions in Pseudomonas aeruginosa pneumonia.* American journal of respiratory and critical care medicine, 2005. **171**(11): p. 1209-1223.

59. Driscoll, J.A., S.L. Brody, and M.H. Kollef, *The epidemiology, pathogenesis and treatment of Pseudomonas aeruginosa infections.* Drugs, 2007. **67**(3): p. 351-68.

60. Moradali, M.F., S. Ghods, and B.H.A. Rehm, *Pseudomonas aeruginosa Lifestyle: A Paradigm for Adaptation, Survival, and Persistence.* Frontiers in cellular and infection microbiology, 2017. **7**: p. 39-39.

61. Passador, L., et al., *Expression of Pseudomonas aeruginosa virulence genes requires cell-to-cell communication.* Science, 1993. **260**(5111): p. 1127-30.

62. Davies, D.G., et al., *The involvement of cell-to-cell signals in the development of a bacterial biofilm.* Science, 1998. **280**(5361): p. 295-8.

63. de Kievit, T.R., *Quorum sensing in Pseudomonas aeruginosa biofilms.* Environ Microbiol, 2009. **11**(2): p. 279-88.

64. Lau, G.W., D.J. Hassett, and B.E. Britigan, *Modulation of lung epithelial functions by Pseudomonas aeruginosa.* Trends in Microbiology, 2005. **13**(8): p. 389-397.

65. Li, X.Z., D.M. Livermore, and H. Nikaido, *Role of efflux pump(s) in intrinsic resistance of Pseudomonas aeruginosa: resistance to tetracycline, chloramphenicol, and norfloxacin.* Antimicrobial agents and chemotherapy, 1994. **38**(8): p. 1732-1741.

66. Hirsch, E.B. and V.H. Tam, *Impact of multidrug-resistant Pseudomonas aeruginosa infection on patient outcomes.* Expert review of pharmacoeconomics & outcomes research, 2010. **10**(4): p. 441-451.

67. Llanes, C., et al., *Clinical Strains of Pseudomonas aeruginosa Overproducing MexAB-OprM and MexXY Efflux Pumps Simultaneously.* Antimicrobial Agents and Chemotherapy, 2004. **48**(5): p. 1797-1802.

68. Mesaros, N., et al., *Pseudomonas aeruginosa: resistance and therapeutic options at the turn of the new millennium.* Clinical Microbiology and Infection, 2007. **13**(6): p. 560-578.

69. Pang, Z., et al., *Antibiotic resistance in Pseudomonas aeruginosa: mechanisms and alternative therapeutic strategies.* Biotechnology Advances, 2019. **37**(1): p. 177-192.

70. Fernández, L. and R.E.W. Hancock, *Adaptive and mutational resistance: role of porins and efflux pumps in drug resistance.* Clinical microbiology reviews, 2012. **25**(4): p. 661-681.

71. Walters, M.C., 3rd, et al., *Contributions of antibiotic penetration, oxygen limitation, and low metabolic activity to tolerance of Pseudomonas aeruginosa biofilms to ciprofloxacin and tobramycin.* Antimicrob Agents Chemother, 2003. **47**(1): p. 317-23.

72. Garnacho-Montero, J., et al., *Optimal management therapy for Pseudomonas aeruginosa ventilator-associated pneumonia: an observational, multicenter study comparing monotherapy with combination antibiotic therapy.* Crit Care Med, 2007. **35**(8): p. 1888-95.

73. Traugott, K.A., et al., *Monotherapy or combination therapy? The Pseudomonas aeruginosa conundrum.* Pharmacotherapy, 2011. **31**(6): p. 598-608.

74. Bassetti, M., et al., *How to manage Pseudomonas aeruginosa infections.* Drugs in context, 2018. **7**: p. 212527-212527.

75. Cohen, M.L., *Staphylococcus aureus: Biology, mechanisms of virulence, epidemiology.* The Journal of Pediatrics, 1986. **108**(5, Part 2): p. 796-799.

76. Foster, T., *Staphylococcus* in *Medical Microbiology*, B. S, Editor. 1996, University of Texas Medical Branch at Galveston: Galveston (TX).

77. Fuchs, S., et al., *Anaerobic gene expression in Staphylococcus aureus.* J Bacteriol, 2007. **189**(11): p. 4275-89.

78. Burke, K.A. and J. Lascelles, *Nitrate reductase system in Staphylococcus aureus wild type and mutants.* J Bacteriol, 1975. **123**(1): p. 308-16.

79. Facklam, R.R. and P.B. Smith, *The gram positive cocci.* Human Pathology, 1976. **7**(2): p. 187-194.

80. Lowy, F.D., *Staphylococcus aureus infections.* N Engl J Med, 1998. **339**(8): p. 520-32.

81. *Staphylococcus aureus in Healthcare Settings*. Centers for Disease Control and Prevention

82. Tong, S.Y.C., et al., *Staphylococcus aureus Infections: Epidemiology, Pathophysiology, Clinical Manifestations, and Management.* Clinical Microbiology Reviews, 2015. **28**(3): p. 603-661.

83. Foster, T.J. and M. Höök, *Surface protein adhesins of Staphylococcus aureus.* Trends in Microbiology, 1998. **6**(12): p. 484-488.

84. O'Riordan, K. and J.C. Lee, *Staphylococcus aureus capsular polysaccharides.* Clin Microbiol Rev, 2004. **17**(1): p. 218-34.

85. Foster, T.J., et al., *Adhesion, invasion and evasion: the many functions of the surface proteins of Staphylococcus aureus.* Nat Rev Microbiol, 2014. **12**(1): p. 49-62.

86. de Haas, C.J., et al., *Chemotaxis inhibitory protein of Staphylococcus aureus, a bacterial antiinflammatory agent.* J Exp Med, 2004. **199**(5): p. 687-95.

87. Berube, B.J. and J. Bubeck Wardenburg, *Staphylococcus aureus α-toxin: nearly a century of intrigue.* Toxins, 2013. **5**(6): p. 1140-1166.

88. Putra, I., et al., *Staphylococcus aureus alpha-hemolysin impairs corneal epithelial wound healing and promotes intracellular bacterial invasion.* Experimental Eye Research, 2019. **181**: p. 263-270.

89. Gordon, R.J. and F.D. Lowy, *Pathogenesis of Methicillin-Resistant Staphylococcus aureus Infection.* Clinical Infectious Diseases, 2008. **46**(Supplement_5): p. S350-S359.

90. Archer, N.K., et al., *Staphylococcus aureus biofilms: properties, regulation, and roles in human disease.* Virulence, 2011. **2**(5): p. 445-459.

91. von Eiff, C., G. Peters, and K. Becker, *The small colony variant (SCV) concept -- the role of staphylococcal SCVs in persistent infections.* Injury, 2006. **37 Suppl 2**: p. S26-33.

92. Edwards, A.M., *Phenotype Switching Is a Natural Consequence of Staphylococcus aureus Replication.* Journal of Bacteriology, 2012. **194**(19): p. 5404-5412.

93. Lowy, F.D., *Antimicrobial resistance: the example of Staphylococcus aureus.* The Journal of clinical investigation, 2003. **111**(9): p. 1265-1273.

94. Jevons, M.P., *"Celbenin" - resistant Staphylococci.* British Medical Journal, 1961. **1**(5219): p. 124-125.

95. Wielders, C.L., *In-vivo transfer of mecA DNA to Staphylococcus aureus [corrected].* Lancet. **357**(9269): p. 1674-1675.

96. Hartman, B.J. and A. Tomasz, *Low-affinity penicillin-binding protein associated with beta-lactam resistance in Staphylococcus aureus.* Journal of bacteriology, 1984. **158**(2): p. 513-516.

97. Fuda, C., et al., *The Basis for Resistance to β-Lactam Antibiotics by Penicillin-binding Protein 2a of Methicillin-resistant Staphylococcus aureus.* Journal of Biological Chemistry, 2004. **279**(39): p. 40802-40806.

98. Matsuo, M., et al., *Comprehensive Identification of Mutations Responsible for Heterogeneous Vancomycin-Intermediate Staphylococcus aureus (hVISA)-to-VISA Conversion in Laboratory-Generated VISA Strains Derived from hVISA Clinical Strain Mu3.* Antimicrobial Agents and Chemotherapy, 2013. **57**(12): p. 5843-5853.

99. Sieradzki, K., et al., *The Development of Vancomycin Resistance in a Patient with Methicillin-Resistant Staphylococcus aureus Infection.* New England Journal of Medicine, 1999. **340**(7): p. 517-523.

100. Showsh, S.A., E.H. De Boever, and D.B. Clewell, *Vancomycin resistance plasmid in Enterococcus faecalis that encodes sensitivity to a sex pheromone also produced by Staphylococcus aureus.* Antimicrobial agents and chemotherapy, 2001. **45**(7): p. 2177-2178.

101. Auwaerter, P.M.D., *Staphylococcus aureus.* 2019.

102. Bal, A.M., et al., *Future trends in the treatment of methicillin-resistant Staphylococcus aureus (MRSA) infection: An in-depth review of newer antibiotics active against an enduring pathogen.* Journal of Global Antimicrobial Resistance, 2017. **10**: p. 295-303.

103. Ballow, C.H., R.N. Jones, and D.J. Biedenbach, *A multicenter evaluation of linezolid antimicrobial activity in North America.* Diagnostic Microbiology and Infectious Disease, 2002. **43**(1): p. 75-83.

104. Itani, K.M., et al., *Efficacy and safety of linezolid versus vancomycin for the treatment of complicated skin and soft-tissue infections proven to be caused by methicillin-resistant Staphylococcus aureus.* Am J Surg, 2010. **199**(6): p. 804-16.

105. Fala, L., *Sivextro (Tedizolid Phosphate) Approved for the Treatment of Adults with Acute Bacterial Skin and Skin-Structure Infections.* American health & drug benefits, 2015. **8**(Spec Feature): p. 111-115.

106. Taylor, S.D. and M. Palmer, *The action mechanism of daptomycin.* Bioorg Med Chem, 2016. **24**(24): p. 6253-6268.

107. Laemmli, U., *Cleavage of structural proteins during the assembly of the head of bacteriophage T4.* Nature, 1970. **227**: p. 680-685.

108. Lowry, O., et al., *Protein measurement with the Folin Phenol reagent.* J. Biol. Chem., 1951. **193**: p. 265-275.

109. Pastra-Landis, S.C., J. Foote, and E.R. Kantrowitz, *An improved colorimetric assay for aspartate and ornithine transcarbamylases.* Anal Biochem, 1981. **118**(2): p. 358-63.

110. Prescott, L.M. and M.E. Jones, *Modified methods for the determination of carbamyl aspartate.* Anal Biochem, 1969. **32**(3): p. 408-19.

111. Muzzarelli, K.M., et al., *Structural and Antiviral Studies of the Human Norovirus GII.4 Protease.* Biochemistry, 2019. **58**(7): p. 900-907.

112. Arakawa, T., et al., *Aggregation Analysis of Therapeutic Proteins, Part 1: General Aspects and Techniques for Assessment*. Vol. 4. 2006. 42-49.

113. Kabsch, W., *XDS.* Acta crystallographica. Section D, Biological crystallography, 2010. **66**(Pt 2): p. 125-132.

114. Adams, P.D., et al., *PHENIX: a comprehensive Python-based system for macromolecular structure solution.* Acta Crystallogr D Biol Crystallogr, 2010. **66**(Pt 2): p. 213-21.

115. Emsley, P., et al., *Features and development of Coot.* Acta Crystallogr D Biol Crystallogr, 2010. **66**(Pt 4): p. 486-501.

116. Joosten, R.P., et al., *The PDB_REDO server for macromolecular structure model optimization.* IUCrJ, 2014. **1**(Pt 4): p. 213-20.

117. Krieger, E. and G. Vriend, *YASARA View—molecular graphics for all devices—from smartphones to workstations.* Bioinformatics, 2014. **30**(20): p. 2981-2982.

118. *Molecular Operating Environment (MOE)*. 2019, Chemical Computing Group ULC: 1010 Sherbrooke St. West Suite#901 Montreal, Quebec, Canada H3A 2R7.

119. Krissinel, E. and K. Henrick, *Inference of macromolecular assemblies from crystalline state.* J Mol Biol, 2007. **372**(3): p. 774-97.

120. Mathee, K., et al., *Dynamics of Pseudomonas aeruginosa genome evolution.* Proceedings of the National Academy of Sciences, 2008. **105**(8): p. 3100.

121. Kang, C.-I., et al., *Pseudomonas aeruginosa Bacteremia: Risk Factors for Mortality and Influence of Delayed Receipt of Effective Antimicrobial Therapy on Clinical Outcome.* Clinical Infectious Diseases, 2003. **37**(6): p. 745-751.

122. Sordé, R., A. Pahissa, and J. Rello, *Management of refractory Pseudomonas aeruginosa infection in cystic fibrosis.* Infection and drug resistance, 2011. **4**: p. 31-41.

123. Adair, L.B. and M.E. Jones, *Purification and characteristics of aspartate transcarbamylase from Pseudomonas fluorescens.* J Biol Chem, 1972. **247**(8): p. 2308-15.

124. Schurr, M.J., et al., *Aspartate transcarbamoylase genes of Pseudomonas putida: requirement for an inactive dihydroorotase for assembly into the dodecameric holoenzyme.* J Bacteriol, 1995. **177**(7): p. 1751-1759.

125. Bijelic, A. and A. Rompel, *Ten Good Reasons for the Use of the Tellurium-Centered Anderson–Evans Polyoxotungstate in Protein Crystallography.* Accounts of Chemical Research, 2017. **50**(6): p. 1441-1448.

126. Porter, R.W., M.O. Modebe, and G.R. Stark, *Aspartate transcarbamylase. Kinetic studies of the catalytic subunit.* J Biol Chem, 1969. **244**(7): p. 1846-59.

127. Williamson, C.L. and R.D. Slocum, *Characterization of an aspartate transcarbamoylase cDNA from pea (Pisum sativum L.).* Plant Physiol, 1993. **102**(3): p. 1055-6.

128. Yon, R., Biochem. J., 1984. **128**: p. 311-320.

129. Williamson, C.L. and R.D. Slocum, *Molecular cloning and characterization of the pyrB1 and pyrB2 genes encoding aspartate transcarbamoylase in pea (Pisum sativum L.).* Plant Physiol, 1994. **105**(1): p. 377-84.

130. Baker, D.P. and E.R. Kantrowitz, *The conserved residues glutamate-37, aspartate-100, and arginine-269 are important for the structural stabilization of*

Escherichia coli aspartate transcarbamoylase. Biochemistry, 1993. **32**(38): p. 10150-8.

131. Baker, D.P., et al., *Weakening of the interface between adjacent catalytic chains promotes domain closure in Escherichia coli aspartate transcarbamoylase.* Protein Sci, 1995. **4**(2): p. 258-67.

132. Neumann, J. and M.E. Jones, *End-Product Inhibition of Aspartate Transcarbamylase in Various Species.* Arch Biochem Biophys, 1964. **104**: p. 438-47.

133. T Abdelal, A., L. Bussey, and L. Vickers, *Carbamoylphosphate synthetase from Pseudomonas aeruginosa. Subunit composition, kinetic analysis and regulation*. Vol. 129. 1983. 697-702.

134. Boucher, H., L.G. Miller, and R.R. Razonable, *Serious infections caused by methicillin-resistant Staphylococcus aureus.* Clin Infect Dis, 2010. **51 Suppl 2**: p. S183-97.

135. Keynan, Y. and E. Rubinstein, *Staphylococcus aureus bacteremia, risk factors, complications, and management.* Crit Care Clin, 2013. **29**(3): p. 547-62.

136. Coleman, P.F., D.P. Suttle, and G.R. Stark, *Purification from hamster cells of the multifunctional protein that initiates de novo synthesis of pyrimidine nucleotides.* Journal of Biological Chemistry, 1977. **252**(18): p. 6379-85.

137. Lee, L., et al., *Oligomeric structure of the multifunctional protein CAD that initiates pyrimidine biosynthesis in mammalian cells.* Proceedings of the National Academy of Sciences, 1985. **82**(20): p. 6802-6806.

138. Tian, W., et al., *CASTp 3.0: computed atlas of surface topography of proteins.* Nucleic Acids Research, 2018. **46**(W1): p. W363-W367.

139. Ruiz-Ramos, A., et al., *Structure and Functional Characterization of Human Aspartate Transcarbamoylase, the Target of the Anti-tumoral Drug PALA.* Structure, 2016. **24**(7): p. 1081-94.

140. Endrizzi, J.A., et al., *Binding of bisubstrate analog promotes large structural changes in the unregulated catalytic trimer of aspartate transcarbamoylase: Implications for allosteric regulation.* Proceedings of the National Academy of Sciences, 2000. **97**(10): p. 5077-5082.

141. Park, H.J., et al., *Clinical significance of Propionibacterium acnes recovered from blood cultures: analysis of 524 episodes.* Journal of clinical microbiology, 2011. **49**(4): p. 1598-1601.

142. Bush, L.M., *Bacteremia* Merck Sharp & Dohme Corp.

143. Naber, C.K., *Staphylococcus aureus Bacteremia: Epidemiology, Pathophysiology, and Management Strategies.* Clinical Infectious Diseases, 2009. **48**(Supplement_4): p. S231-S237.

144. van Hal, S.J., et al., *Predictors of Mortality in Staphylococcus aureus Bacteremia.* Clinical Microbiology Reviews, 2012. **25**(2): p. 362-386.

145. Thomer, L., O. Schneewind, and D. Missiakas, *Pathogenesis of Staphylococcus aureus Bloodstream Infections.* Annual review of pathology, 2016. **11**: p. 343-364.

146. Singer, M., et al., *The Third International Consensus Definitions for Sepsis and Septic Shock (Sepsis-3)Consensus Definitions for Sepsis and Septic*

ShockConsensus Definitions for Sepsis and Septic Shock. JAMA, 2016. **315**(8): p. 801-810.

147. Maggio, P.M., *Sepsis and Septic Shock*. Merch Sharp & Dohme Corp.

148. Polat, G., et al., *Sepsis and Septic Shock: Current Treatment Strategies and New Approaches.* The Eurasian journal of medicine, 2017. **49**(1): p. 53-58.

149. Rhodes, A., et al., *Surviving Sepsis Campaign: International Guidelines for Management of Sepsis and Septic Shock: 2016.* Crit Care Med, 2017. **45**(3): p. 486-552.

150. Lief, L., J. Arbo, and D.A. Berlin, *The Physiology of Early Goal-Directed Therapy for Sepsis.* J Intensive Care Med, 2017. **32**(10): p. 567-573.

151. Cassat, J.E. and E.P. Skaar, *Iron in infection and immunity.* Cell host & microbe, 2013. **13**(5): p. 509-519.

152. Simmonds, R.J. and R.A. Harkness, *High-performance liquid chromatographic methods for base and nucleoside analysis in extracellular fluids and in cells.* J Chromatogr, 1981. **226**(2): p. 369-81.

153. Samant, S., et al., *Nucleotide biosynthesis is critical for growth of bacteria in human blood.* PLoS pathogens, 2008. **4**(2): p. e37-e37.

154. Connolly, J., et al., *Identification of Staphylococcus aureus Factors Required for Pathogenicity and Growth in Human Blood.* Infection and immunity, 2017. **85**(11): p. e00337-17.

155. Sterling, T. and J.J. Irwin, *ZINC 15 – Ligand Discovery for Everyone.* Journal of Chemical Information and Modeling, 2015. **55**(11): p. 2324-2337.

ABSTRACT

BIOCHEMICAL, STRUCTURAL, AND DRUG DESIGN STUDIES OF ASPARTATE TRANSCARBAMOYLASE FROM *PSEUDOMONAS AERUGINOSA* AND *STAPHYLOCOCCUS AUREUS*

by

CHANDNI PATEL

August 2019

Advisor: Dr. David Evans

Major: Biochemistry and Molecular Biology

Degree: Doctor of Philosophy

Sepsis affects 1.7 million people in the United States every year and nearly 270,000 people die as a result. Sepsis is characterized by systemic inflammation from an infection leading to organ dysfunction and death. Multi-drug resistance in bacteria is increasing globally, and *Pseudomonas aeruginosa* and *Staphylococcus aureus* are notorious for their multi-drug resistance and pose a serious need for the development of new antibiotics. The levels of pyrimidines in blood are too low to sustain the growth of bacteria, so they must rely on pyrimidine biosynthesis. Previous studies have shown that a defect in several pyrimidine biosynthetic enzymes resulted in 1000-fold decrease in the titer of bacteria growing in blood. Aspartate transcarbamoylase (ATCase) catalyzes the first committed step of the *de novo* pyrimidine pathway, making it an attractive drug target in pyrimidine biosynthesis. The following dissertation utilizes biochemical and biophysical tools to understand the regulatory and structural properties of ATCase in *P. aeruginosa* and *S. aureus* as well as to identify potential sites for ATCase inhibition.

In this dissertation, I demonstrate that pDHO is a requirement for *P. aeruginosa* ATCase because ATCase does not self-associate to form a stable trimer and that pDHO facilitates ATCase trimer formation. The basis for why pDHO was a requirement for ATCase activity was not explored previously. Additionally, I explore the role of N- and C-terminal extensions of *P. aeruginosa* ATCase and demonstrate that these extensions are not involved in the ATCase-pDHO complex formation or nucleotide inhibition by ATP. This led me to conclude that the binding site of ATP is not located in the 11-residue extension of ATCase as previously suggested. Furthermore, I demonstrate that ATP inhibition of ATCase is not an allosteric mechanism, rather it is a consequence of the destabilization of the ATCase-pDHO complex. Lastly, I solved the crystal structure of *P. aeruginosa* delN ATCase-pDHO complex with a molecule of TEW bound in the active site of delN ATCase and demonstrated that TEW is a potent inhibitor of *P. aeruginosa* ATCase.

In my dissertation, I demonstrate that *S. aureus* ATCase is a stable catalytic trimer. *S. aureus* ATCase functions independently and does not associate with DHOase. I solved the crystal structure of *S. aureus* ATCase bound to an active site inhibitor, N-phosphonacetyl-L-aspartate (PALA), and validated that *S. aureus* ATCase undergoes domain closure upon PALA binding as observed in other ATCases. Using this crystal structure of *S. aureus* ATCase, I identified two sites for inhibition, including the interdomain cleft and the trimer interface. I screened top-ranking FDA-approved compounds against *S. aureus* ATCase in an in vitro assay after virtual screening. Although none of the compounds had a significant inhibitory effect on *S. aureus* ATCase, nitazoxanide showed dose-dependent destabilization of ATCase. This suggests that nitazoxanide does not show inhibitory activity probably due to its poor binding to ATCase.

AUTOBIOGRAPHICAL STATEMENT

Education

2014-Pr.	Ph.D. Biochemistry and Molecular Biology, Wayne State University, Detroit, MI
2009-2013	B.S. Biological Sciences Honors, Wayne State University, Detroit, MI

Honors and Awards

2018	Innovation Honors Award, Innovation Honors Program, Wayne State University
2018	Cayman Chemical Travel Award
2018	BEST [Broadening Experiences in Scientific Training] Program Phase III Career Exploration Award
2017-Pr.	American Heart Association Predoctoral Fellowship
2017	C.P. Lee Graduate Student Professional Travel Award, Wayne State University
2017	Graduate Student Professional Travel Award, Wayne State University
2017	Award for Graduate Students who Obtain External Support, Office of Vice President for Research, Wayne State University
2016	American Society of Biochemistry & Molecular Biology 2017 Graduate Award
2016	C.P. Lee Graduate Student Professional Travel Award, Wayne State University
2016	Graduate Student Professional Travel Award, Wayne State University
2015-2017	Interdisciplinary Biomedical Sciences Fellowship, Wayne State University School of Medicine

Positions

2018-2019	President, Biochemistry, Microbiology, and Immunology (BMI) Graduate Student Organization, Wayne State University School of Medicine
2017-2018	Student Representative, Biochemistry & Molecular Biology Ph.D. Program

Publications

Prangé T., Girard E., Fourme R., Dhaussy A., Edwards B., Vaishnav A., **Patel C**., Guy-Evans H., Hervé G. and David Evans (2019) *Pressure-induced activation of latent Dihydroorotase from Aquifex aeolicus as revealed by high pressure protein crystallography.* The FEBS Journal (FJ-18-1006)

Hervé, G., Evans, H. G., Fernado, R., **Patel, C**., Hachem, F., and Evans, D. R. (2016) Activation of latent dihydroorotase from Aquifex aeolicus by pressure. JBC 292, 629-637.